Università degli Studi di Ferrara
Dipartimento di Fisica e Scienze della Terra

Dottorato di Ricerca in Fisica

Settore disciplinare: Fis/01

Curved crystals as optical elements for focusing X- and γ rays in a Laue lens

Supervisor:
Prof. Vincenzo Guidi

Ph.D. candidate:
Riccardo Camattari

Dottorato di Ricerca
XXVI Ciclo. 2011-2013

Referees of the thesis

Prof. Peter von Ballmoos
 Institut de Recherche en Astrophysique et Planétologie, Toulouse, France

Prof. Giovanni Mattei
 Department of Physics and Astronomy "Galileo Galilei", Padova, Italy

Ph.D. candidate

Riccardo Camattari
 Department of Physics and Earth Sciences, University of Ferrara, Italy

Supervisor

Prof. Vincenzo Guidi
 Department of Physics and Earth Sciences, University of Ferrara, Italy

Curved crystals as optical elements for focusing X- and γ rays in a Laue lens: manufacturing, data analyses and Monte Carlo simulations

Short abstract:

This thesis is devoted to achieve a method to realize bent crystals in order to diffract hard X- and γ rays with high-efficiency. Several schemes were pursued to obtain high-focusing diffraction for the production of a high-resolution Laue lens. The focusing capabilities of the crystals were tested with monochromatic and polychromatic X- and γ rays at the European Synchrotron Radiation Facility (ESRF) and at the Institut Laue-Langevin (ILL) in Grenoble, France. Finally, original schemes for the realization of innovative Laue lenses, based on quasi-mosaic crystals, were simulated and proposed.

Keywords: High-focusing diffraction - bent crystals - quasi-mosaicity - Laue lens simulations

ARTICLES INCLUDED IN THE THESIS

Articles published during the Ph.D. which this thesis relies on.

I V. Bellucci, R. Camattari, V. Guidi, I. Neri, and N. Barrière.
   Self-standing bent silicon crystals for very high efficiency laue lens
   Exp. Astron. (**31**), 45-58, 2011

II V. Guidi, V. Bellucci, R. Camattari, and I. Neri
    Proposal for a laue lens with quasi-mosaic crystalline tiles
    J. Appl. Cryst. (**44**), 1255-1258, 2011

III R. Camattari, V. Guidi, L. Lanzoni, and I. Neri
     Experimental analysis and modeling of self-standing curved crystals for focusing of x-rays
     Meccanica (**48**), 1875-1822, 2013

IV R. Camattari, V. Guidi, V. Bellucci, I. Neri, and M. Jentschel
    Self-standing quasi-mosaic crystals for focusing hard X-rays
    Rev. Sci. Instrum. (**84**), 053110-053110-4, 2013

V V. Bellucci, R. Camattari, and V. Guidi
   Proposal for a Laue lens relying on hybrid quasi-mosaic curved crystals
   Astron. Astrophys. (**48**), 1-8, 2013

VI R. Camattari, A. Battelli, V. Bellucci, and V. Guidi
    Highly reproducible quasi-mosaic crystals as optical components for a laue lens
    Exp. Astron., in press , 2013

VII R. Camattari, G. Paternò, A. Battelli, V. Bellucci, P. Bastie and V. Guidi
     High-efficiency focusing of hard X-rays exploiting the quasi-mosaic effect in a bent germanium crystal
     Submitted to J. Appl. Cryst., 2013

VIII R. Camattari, G. Paternò, V. Bellucci and V. Guidi
      Quasi-mosaicity of (311) planes in silicon and its usage in a high-focusing Laue lens
      Submitted to Exp. Astron., 2013

Articles not included in the thesis

Articles published during the Ph.D. as side products of this thesis.

- V. Bellucci, R. Camattari, V. Guidi and A. Mazzolari
  Bending of silicon plate crystals through superficial grooving: Modeling and experimentation
  Thin Solid Films (**520**), 10691073, 2011

- V. Bellucci, R. Camattari, I. Neri, and V. Guidi
  Calculation of diffraction efficiency for curved crystals with arbitrary curvature radius
  J. Appl. Cryst. (**46**), 415-420, 2013

- I. Neri, R. Camattari, V. Bellucci, V. Guidi, and P. Bastie
  Ordered stacking of crystals with adjustable curvatures for hard X- and γ-ray broadband focusing
  J. Appl. Cryst. (**46**), 953-959, 2013

- V. Guidi, V. Bellucci, R. Camattari, and I. Neri.
  Curved crystals for high resolution focusing of X and γ rays through a laue lens
  Nucl. Instrum. Meth. B (**309**), 249-253, 2013

Articles published before the Ph.D.

- N. Barrière, V. Guidi, V. Bellucci, R. Camattari, T. Buslaps, J. Rousselle, G. Roudil, F. Arnaud, P. Bastie and L. Natalucci
  High diffraction efficiency at hard X-ray energy in a silicon crystal bent by indentation
  J. Appl. Cryst., (**43**), 4849-1521, 2010

PREFACE

This work aims at the realization of properly processed silicon and germanium crystals which could be used as optical elements to diffract and focus hard X- and γ rays in the 100-1000 keV energy range. These kinds of crystals have recently met the interest of the astrophysics community because they could allow high-sensitivity observations of many cosmic phenomena on a satellite-borne focusing telescope and collect information from the universe as seen through X-rays. Moreover, such crystals could be used as a γ ray imager in nuclear medicine to diagnose the presence of cancer pathologies in the human body through γ decays of metastable radioisotopes such as ^{99m}Tc.

The work of thesis was carried out within the Laue project, which is a project financed by the Italian Space Agency (ASI). The final aim of the Laue project was the realization of a prototype of Laue lens composed of germanium and gallium arsenide bent crystals. In particular, the realization and the pre-characterization of the germanium samples were performed during this Ph.D. period.

This thesis is divided into three main sections. The first section presents the empirical study performed to develop a method that would lead to the production of accurate and homogeneous bent samples. In fact, a homogeneous curvature is a necessary condition for the diffraction of the radiation with high efficiency and resolution. The resulting proposed method is economical and simple, being based on mass production tools. Furthermore, an appropriate physical model is given, to foresee the curvature of the samples as a function of the production parameters.

Several silicon and germanium samples were bent and pre-characterized at the Sensor and Semiconductor Laboratory (SSL) of Ferrara, Italy. Afterwards, the focusing capabilities of the samples were analyzed at the European Synchrotron Radiation Facility (ESRF) and at the Institut LaueLangevin (ILL) of Grenoble, France. In the second section the tests with X- and γ rays performed with the produced samples are described.

In the last section, investigations and experimental validations of diffraction with unusual crystal configurations are described. Furthermore, two proposals of Laue lens are given. Such proposals were theoretical obtained with *LaueGen*, a genetic algorithm written for this purpose. Finally, the performance of these simulated Laue lenses is shown and compared with the data available in the literature.

Contents

Introduction

Manipulation and focusing of hard X- and γ-rays in the 100-1000 keV energy range represent an increasingly significant topic for the scientific community. However, it is not trivial to focalize X-rays with good efficiency, and the modalities of implementation of an X-ray concentrator still represent an open issue.

Loosely speaking, observing hard X-ray or soft γ-ray astronomical sources in this energy range is analogous to the pre-Galilean naked-eye observation of the sky compared to the modern device-assisted astronomy with a telescope because high-energy photons cannot be concentrated. Strictly speaking, the lack of optical components working within this energy range implies the impossibility of focusing, which in turn leads to a poor signal-to-noise ratio recorded by the detectors. Indeed, multilayer optics have been proven to be capable of focusing of up to 80 keV photons with high-efficiency. More recently it has been demonstrated that multilayer reflective optics can operate efficiently and according to classical wave physics up to photon energies of at least 384 keV. However, beyond these limits the efficiency of these optics critically deteriorates [1].

In fact, there exists a wealth of experiments that could be performed, provided that a suitable sensitivity of detection devices would be accomplished. Indeed, γ-ray emission takes place in several places in the Universe, spanning from our Sun to the γ-ray bursts (GRBs) at redshifts z > 8 and to the cosmic γ-ray background radiation of the early Universe. Cosmic γ rays originate locally in solar flares, within our Galaxy in compact binary systems, pulsars, supernova remnants, and in extremely distant objects such as active galactic nuclei and GRBs. The study of the origin of the positrons annihilating in the Galactic center could be visible through the e^+ / e^- annihilation line at 511 keV. A study of the distribution of this emission line would thus bring new clues concerning the still elusive sources of antimatter. Although a 511 keV emission has been observed for more than 30 years towards the Galactic center [2], the origin of the positrons still remains a mystery. Stellar nucleosynthesis [3, 4, 5], accreting compact objects [6, 7, 8, 9], and even the annihilation of exotic dark-matter

particles [10] have all been suggested, thus a deeper investigation is necessary.

An X-ray concentrator could also be used as an imager for high-quality imaging in nuclear medicine. For instance, it would improve γ-ray detection in single photon emission computed tomography (SPECT) by providing better scan resolution. This, in turn, would lead to a lower radioactive dose being imparted to the patient, since there would be no need for tomography scanning [11, 12].

In order to make the realization of the above experiments possible, optical elements with high-diffraction efficiency are needed, along with an arrangement of the crystals to permit high-resolution focusing of the diffracted photons. In this thesis, a method to produce bent crystals suitable for high-efficiency diffraction, namely the grooving method, is proposed and experimentally tested. The method consists in grooving one of the major surfaces of a sample with a grid of regular grooves. In fact, it was shown that a series of superficial grooves may permanently and reproducibly bend the whole crystal. Moreover, a study of the theory of linear elasticity was done to exploit the quasi-mosaic effect. Through the quasi-mosaic effect, it is possible to obtain two curvatures of two different lying of crystallographic planes. The grooves generate a primary curvature on the largest surfaces of a plate. As a result of the primary curvature, quasi-mosaicity induces a secondary curvature on a perpendicular set of planes within the crystal, whose radius depends on the material and the crystallographic orientations concerned [13]. Combining these two curvatures, it is possible to achieve either high-diffraction efficiency and focalization of the diffracted beam [13, 14].

The diffraction efficiency and the focusing capability of the produced crystals were analyzed and compared with the theoretical expectations. A series of grooved samples was produced for the realization of a prototype of Laue lens, within the Laue project.

Finally, a computational method based on a genetic algorithm and named *Laue-Gen*, was developed *ab initio* to simulate and optimize new schemes of Laue lens based on quasi-mosaic crystals. The focusing capability of the simulated Laue lenses, such as the focusing factor and the sensitivity, are shown and compared with the results available in the literature.

CHAPTER 1

State of the art

1.1 Focusing X- and γ- rays: the Laue lens

Nowadays, the scientific community is seeking for methods to make the experiments based on the Laue lens come true [15]. One nonfocusing method that has already been proposed for X-rays detection consist in the usage of geometrical optics, such as collimators or coded masks [16]. However, since the total interaction cross-section for γ-rays attains its minimum within 100-1000 keV, the efficiency of geometrical optics decreases while at the same time the background noise increases with respect to the signal, because of the growing importance of shield leakage and/or $n\beta$ activation. Another nonfocusing solution consists of quantum optics based on Compton effect and tracking detectors [17].

However, focusing methods probably have greater potential because they can concentrate the signal from a large collector onto a small detector and beat the instrumental background that may hamper the observation. Bragg diffraction can be used to concentrate the signal. Indeed, the photon energy is linked to the photon energy via

$$n\lambda = 2d_{hkl}sin\theta_B \tag{1.1}$$

where λ is the radiation wavelength, d_{hkl} the d-spacing of the diffracting planes and θ_B is the Bragg angle.

If X-ray diffraction occurs traversing the crystal (the Laue scheme), the problem of focusing hard X-rays can be approached via a Laue lens. A Laue lens is conceived as an ensemble of many crystals arranged in such a way that as much radiation as possible is diffracted onto the lens focus over a selected energy band (see Fig. 1.1) [18, 19, 20, 21]. For practical applications of a Laue lens, crystals with high-diffraction efficiency are
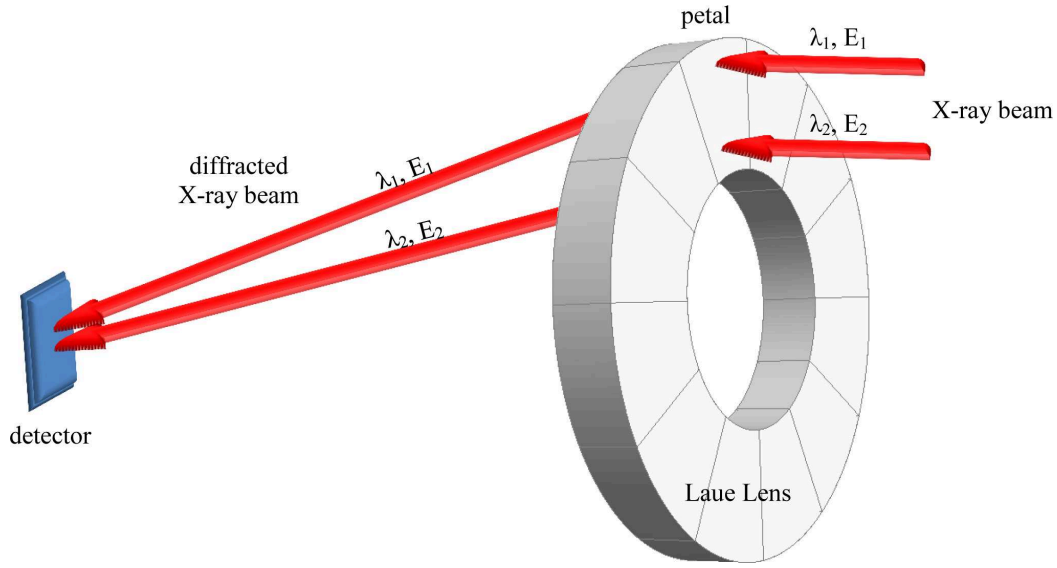
Figure 1.1: Laue lens

needed, as well as an arrangement of the crystals to permit high-resolution focusing of diffracted photons [22, 23].

The high-resolution focusing of diffracted photons is an important requirement in all the applications mentioned above. Perfect and flat mono-crystals diffract within a very narrow energy range, so they are not adequate for a Laue lens (Fig. 1.2a). With the aim of wide-passband focusing, one of the components currently under investigation by the scientific community is the mosaic crystal. This kind of crystal is an aggregation of crystallites whose angular distribution is a Gaussian spread about a nominal direction [24] (Fig. 1.2b). For a mosaic crystal, reflectivity is given by [24]

$$\eta_M = \frac{1}{2}[1 - e^{-2W(\Delta\theta)QT_0}]e^{\frac{-\mu T_0}{cos\theta_B}} \tag{1.2}$$

where T_0 is the crystal thickness traversed by radiation, $\Delta\theta$ is the difference between the angle of incidence and Bragg angle θ_B, μ the linear absorption coefficient within the crystal and $W(\Delta\theta)$ the distribution function of crystallite orientations. In turn, $W(\Delta\theta)$ is defined as

$$W(\Delta\theta) = 2\left(\frac{ln2}{\pi}\right)^{\frac{1}{2}}\frac{1}{\Omega_M}e^{-ln2(\frac{\Delta\theta}{\Omega_M/2})^2} \tag{1.3}$$

where Ω_M is called mosaicity, or mosaic spread, and represents the full width at half maximum (FWHM) of the angular distribution of crystallites. Finally, considering the kinematical theory approximation [25], Q is given by
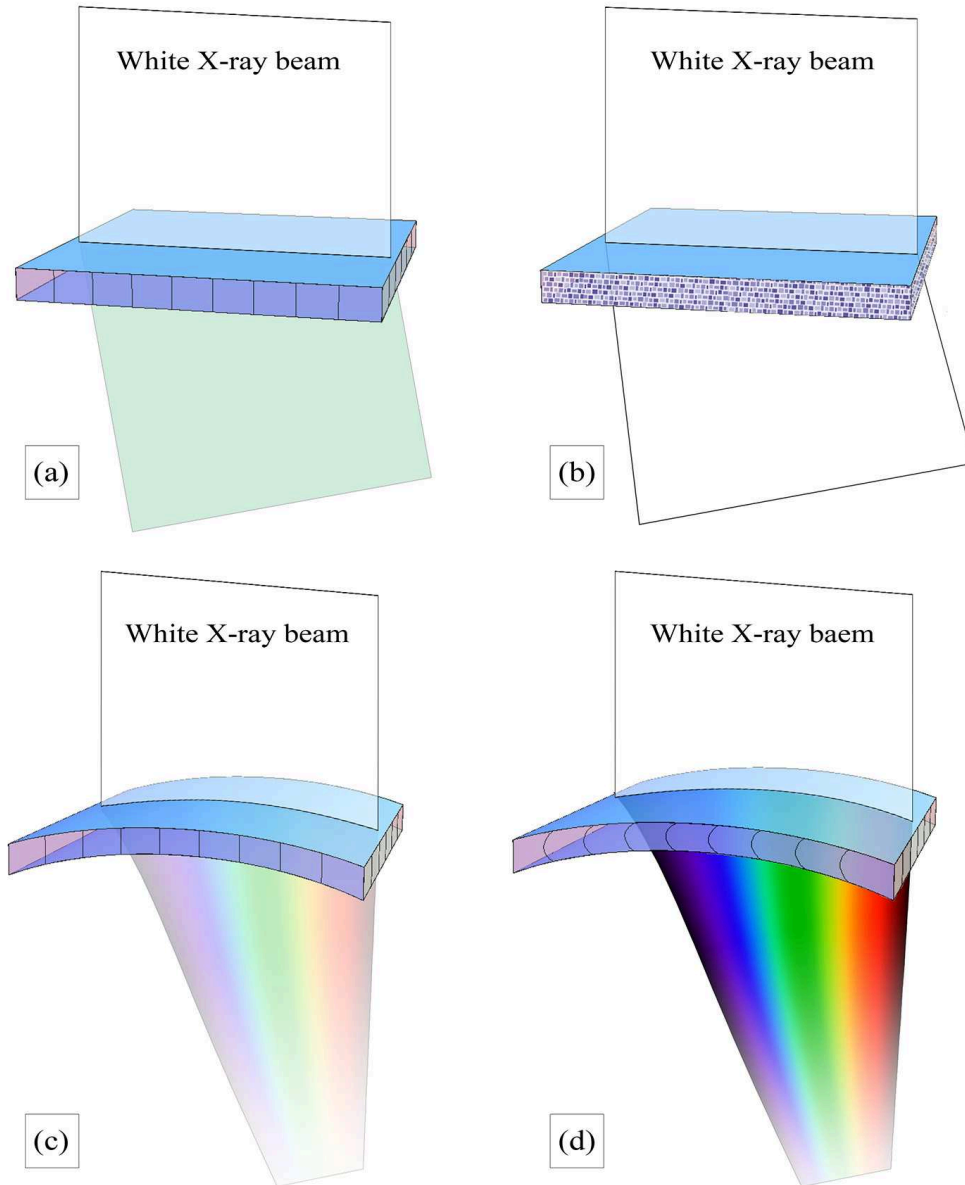
Figure 1.2: Diffraction capability with different kind of crystals, considering a white X-ray beam impinging on the plate. (a) *Perfect crystal.* If the Bragg condition is satisfied, a precise wave length will be diffracted with the efficiency being dependent on the thickness traversed. The integrated reflectivity is very low. (b) *Mosaic crysatal.* The diffraction efficiency is higher with respect the case a), but it is limited at 50% and the spatial resolution of the diffracted photons is limited by the mosaic defocusing effect. c) *Bent crystal but without QM curvature.* The primary curvature can focalize the diffracted photons. However, the flat diffracting planes reduce the integrated intensity. d) *Bent crystal with QM curvature.* QM sample combines the focusing action due to the primary curvature with the high reflectivity of CDP built up by quasi-mosaicity.

$$Q = \frac{\pi^2 d_{hkl}}{\Lambda_0^2 cos\theta_B} \tag{1.4}$$

where Λ_0 is the extinction length as defined in [26] for the Laue symmetric case.

The mosaic crystal has two main disadvantages. Firstly, it has a limited diffraction efficiency, corresponding to a maximum of 50% in reflectivity at zero absorption. Secondly, the spatial resolution of the diffracted photons is limited because of the so-called mosaic defocusing effect [27]. Crystals with curved diffracting planes (CDP crystals) represent an alternative to mosaic crystals with the potential to overcome these two drawbacks. In fact, their energy bandpass can be very well controlled, because it is proportional to the curvature. Moreover, their diffraction efficiency is not limited to 50% [25, 28] because the continuous change of the incidence angle on bent crystalline planes prevents re-diffraction of a diffracted beam. Furthermore, the energy bandpass of the photons diffracted by CDP crystals is orders of magnitude broader than that obtained from flat crystals.

Given the numerous advantages of CDP crystals, in this thesis a study of Laue diffraction with these crystals has been proposed and experimentally validated through hard X-ray diffraction. For CDP crystals, reflectivity is given by [25]

$$\eta_C = \left[1 - e^{\frac{-\pi^2 T_0 d_{hkl}}{\Omega\Lambda_0^2}}\right]e^{\frac{-\mu T_0}{cos\theta_B}} \tag{1.5}$$

where, in this case, Ω represents the bending angle of the curved diffracting planes.

A particular kind of CDP crystal, that employs the so-called quasi-mosaic (QM) effect [13], has also been recently proposed as optical component for focusing hard X-rays (Fig. 1.2d).

1.2 Crystals with curved diffracting planes and quasi-mosaic crystals

CDP crystals disposed with respect to impinging photons (as in Fig. 1.3a, hereinafter named geometry 1) were recently proposed and their high reflectivity demonstrated [29]. A scheme based on such geometry is certainly a viable route for building a Laue lens. However, it requires the fabrication and the setting up of a large number of such crystals to cover the whole Laue lens, because the crystals must be oriented with their major faces parallel to the photon direction. To overcome this problem and expose the largest crystal surface to the photon flux, the geometry 2 has subsequently
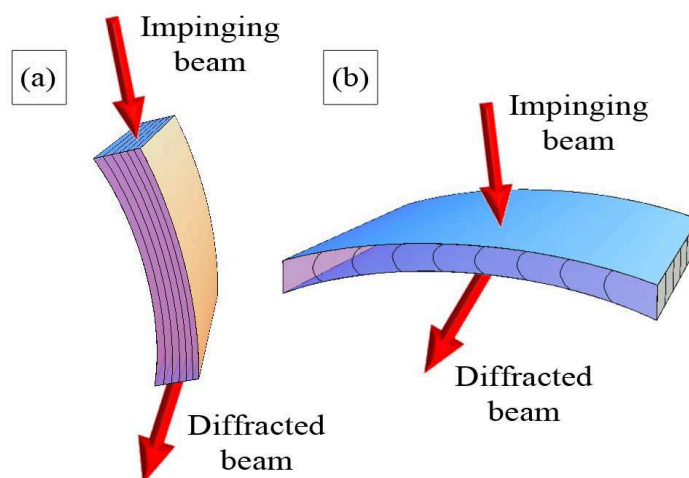
Figure 1.3: (a) geometry 1. (b) geometry 2. Red arrows represent an X-ray beam.

been proposed and is depicted in Fig. 1.3b. Indeed, geometry two would require the fabrication and the setting up of about 10^2 samples, in contrast with 10^3-10^4 samples needed for geometry 1.

A necessary condition for obtaining crystals with CDPs in geometry 2 involves the employment of the quasi-mosaic (QM) effect. QM crystals belong to a class of CDP crystals featuring two curvatures of two different lying of crystallographic planes. As a crystal is bent to a primary curvature by external forces under very specific orientations, another curvature (secondary curvature) is generated within the crystal, i.e., the QM curvature [30]. A Laue lens with QM crystals is an arrangement of curved plates whose primary curvature lies on a spherical calotte of radius R_P, while the QM curvature allows diffraction with CDPs. Due to Bragg diffraction, focusing of each QM sample converges on a focal spot at a distance $f = R_P/2$ on the symmetry axes of the calotte (see Fig. 1.4).

Quasi-mosaicity is a mechanical property driven by anisotropy and is fully explained by the theory of linear elasticity in an anisotropic medium [31]. Most importantly, quasi-mosaicity allows focusing of the photon flux in a spot smaller than the size of the diffracting crystal, in contrast to diffraction by a mosaic crystal, the spot of which is no smaller than the crystal size exposed to the photons. For a quasi-mosaic crystal, the primary curvature is responsible for focusing, while the secondary (QM) curvature increases the diffraction efficiency [13]. Thus, since the secondary curvature can control the size of the focal spot, QM crystals allow focusing with high resolution. As a result, the sensitivity of a Laue lens could be increase. Indeed, if there were no QM effect, the integrated reflectivity of the whole lens would be the same as that
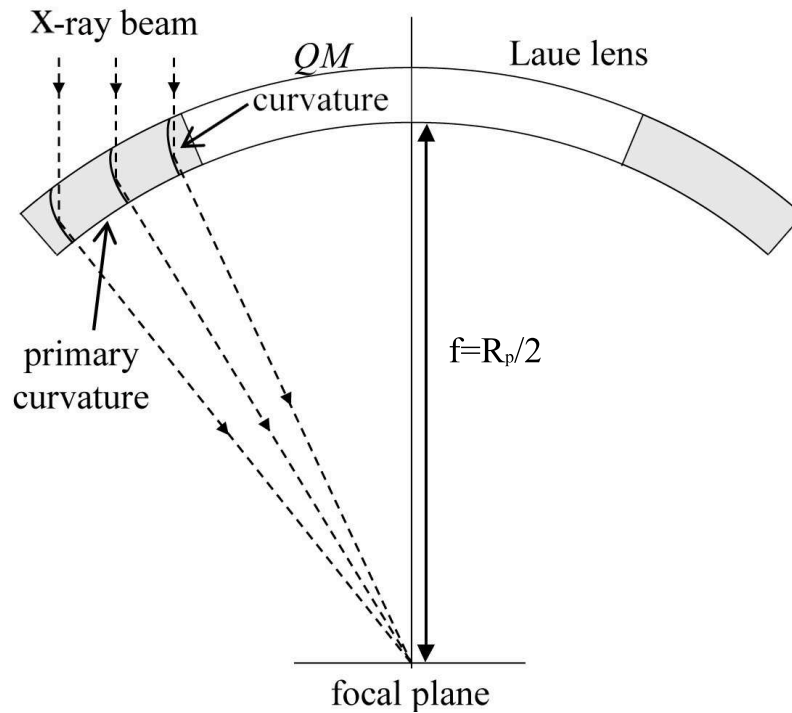
Figure 1.4: Schematic representation of a cross section of a Laue lens based on QM crystals. Gray rectangles represent the crystals. The primary curvature leads to a secondary curvature of the planes affected by quasi-mosaicity. In this configuration the QM diffracting planes are perpendicular to the main surface of the plates. The primary curvature allows focalizing diffracted radiation onto the focal plane, while the QM curvature increases the integrated diffraction efficiency.

obtained from flat diffracting planes, which is relatively poor.

In this work of thesis CDP crystal properties are deeply discussed and analyzed. Moreover, this work demonstrates how such crystals can be manufactured as optical elements for a Laue lens. Finally, it is studied how a Laue lens based on QM crystals can be realized.

CHAPTER 2

Self-standing bent crystals as optical elements: the method of grooving

2.1 Crystals deformation

Novel applications can be attained through the usage of bent crystals as optical components for the focalization of hard X- and γ- rays through Bragg diffraction. Nuclear astrophysics, nuclear medicine and homeland security would highly benefit from such optics, because they all share the same need for efficient X- and γ-ray focusing systems.

For the fabrication of a bent crystal, several techniques were developed. Bending can be accomplished by mechanical means, i.e., by deforming a perfect single crystal through an external device [32]. Mechanically bent crystals have been used in synchrotrons since decades as high-efficiency monochromators at high-energy X-ray beamlines [33, 34]. Curved crystals are also very efficiently used to control neutron diffraction over a wide angular acceptance [33, 35, 36, 37, 38]. However, the usage of an external device leads to excessive weight, condition not permitted for satellite-borne experiments. Thus, self-standing bent crystals are mandatory for the practical implementation of a focusing telescope. Such curved crystal can be produced by applying a thermal gradient to a perfect single crystal [11]. However, this method is energy consuming and not suitable to a space-borne observatory as well. Crystals having curved diffracting planes can also be obtained by a concentration-gradient technique, i.e., by growing a two-component crystal with graded composition along

the growth axis [11, 28, 39, 40]. However, crystals bent by such a method are not easy to manufacture. As a result, the technique hardly applicable for a Laue lens application, for which serial production of crystals should be envisaged.

The process of plastic deformation in a material occurs when the material shape and structure irreversibly change in response to the application of forces. Curved crystals can be obtained by controlled surface damage by means of a mechanical lapping process on one side of planar samples. The surface damage introduces defects in a superficial layer of a few tens of micrometres in thickness. The superficial layer results subjected to a highly compressive strain [41]. However, with this technique, it is impossible to obtain bent samples thicker than 1 - 2 millimeters.

A rather non conventional method to deform crystalline plates is grooving of one of its major surfaces with a grid of regular grooves. In fact, it was shown that series of superficial grooves may permanently and reproducibly bend the whole crystal. In 70-GeV proton channeling experiments [42], it was found that accidental microscratches on a crystal surface cause a deformation of the crystallographic planes to substantial depths, down to a few hundred microns. The analysis showed that protons near a scratch are channeled by deformed crystal planes. For example, it was proved that bent Si and Ge mono-crystals can deflect high-energy charged particles, exploiting axial or planar potential within the crystal [43, 44]. It was also shown that a silicon plate alternatively grooved on its major faces could be used as a crystalline undulator with the purpose of fabricating a miniature free-electron laser [45].

Though the surface grooving method allows to obtain highly reproducible bent crystals, the physical mechanisms behind the process of deformation of crystals by superficial grooves have not been fully understood yet. An extensive study was carried out to understand the process of substrate deformation. By adjusting experimental parameters, very good control of the curvature was achieved. The process of deformation was modeled in terms of the irreversible compression that occurs in the material close to the grooves. The underlying material was treated as an anisotropic medium elastically reacting to the state of stress provided by the grooves. A good correlation between experimental results and theoretical expectations was satisfactorily achieved.

2.2   Material and methods

The fabrication of bent Si crystals was developed with the method of superficial grooving through the usage of a high precision dicing saw (DISCO^{TM} DAD3220), equipped with a rotating blade of various size, geometry and diamond grit size.

To verify the possibility of deforming a sample through the grooving method, a

preliminary test was done on a $10 \times 10 \times 2$ mm^3 silicon sample. A single groove, 160 μm wide and 1680 μm deep, was done parallel to the sample sides and passing through the center of the sample surface (see left side of Fig. 2.1). Analysis of the deformation of the crystal, i.e., of its crystallographic planes, was performed at several positions along x axis, by using a high-resolution X-ray diffractometer (X'Pert Pro MRD XL PANalytical^{TM}) in Bragg geometry (Cu Kα radiation, $\lambda = 1.54$ $\mathring{A}$). For every step, the crystal was rotated in the neighborhood of the angle where the Bragg diffraction occurs. The diffracted radiation was recorded as a function of the incident angle. The achieved profile of intensity is the so called rocking curve (RC) (see right side of Fig. 2.1). As can be noticed, the Si plate takes the shape of a dihedron bent by 30 arcsec just beneath the groove.

If instead of an individual groove, a regular grid of grooves is done on the same surface, a net curvature can be achieved. This is the key idea about deformation of a plate by the method of surface grooving.

To deepen the study, periodic grooves$-$160 μm wide$-$at variable depths were manufactured on one of the major sides of Si plates, each sample being a square with lateral dimension of 10 mm and a thickness ranging from 0.5 to 2 mm. Crystals were (111) oriented so that Young's modulus and Poisson's ratio remained constant along any direction of their surface. Furthermore, to avoid unwanted asymmetries, the grooves were made along two perpendicular directions. A photo of a grooved sample is shown in Fig. 2.2, while fabrication parameters of all samples are reported in Tab. 2.1.

For every crystal, the morphological curvature, as generated by the grooves, was measured by using an optical profilometer (VEECO^{TM} NT1100) with vertical resolution of the order of 1 nm. The instrument is equipped with a stitching system that allows scanning over an area of 10×10 cm^2. In order to account for the initial morphological non-planarity of the samples (wafers generally exhibit non zero bowing) and thereby to consider only the effect of the grooves, subtraction of the profiles before and after grooving was done. Since the profile of a surface with grooves is superficially altered by their presence, the measurements were carried out on the back face of the samples. A typical interferometric measurement of a grooved plate is shown in Fig. 2.3. As can be noticed, the curvature of the sample is homogeneous and spherical.

Production and characterization of all samples was carried out at the Sensor and Semiconductor Laboratory (SSL) of Ferrara, Italy.
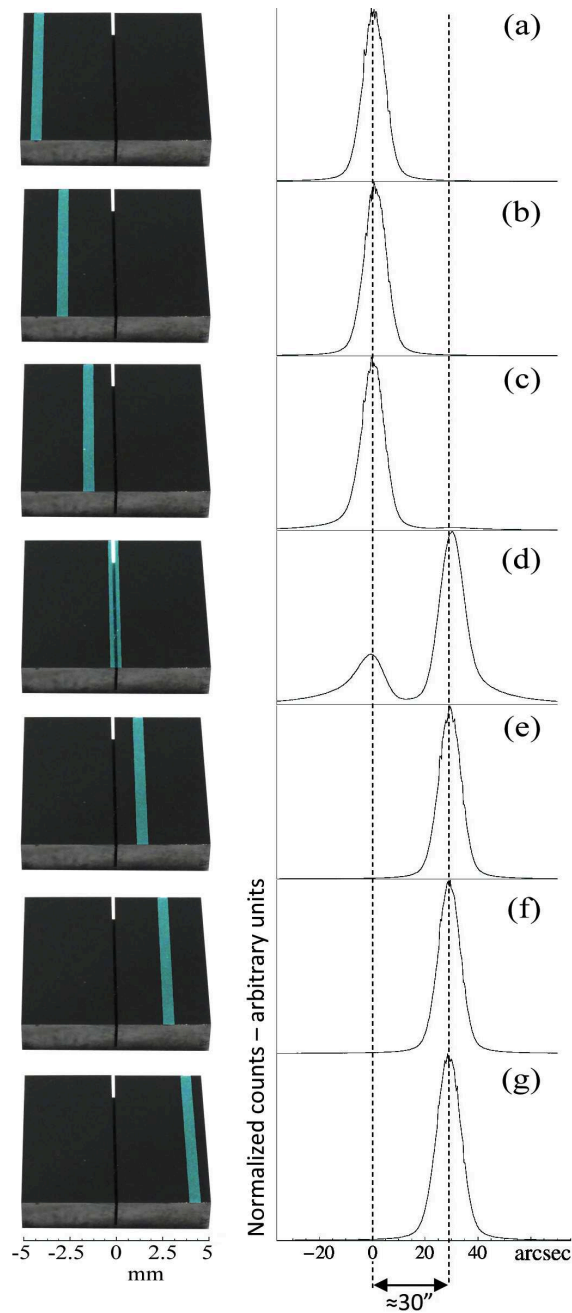
Figure 2.1: Left side: photos of the $10 \times 10 \times 2$ mm³ Si plate. The clearer rectangles represent the areas where X-ray beam impinges for diffraction. The groove is centered at x = 0 mm. Seven measures was done, at (a) = -4 mm, (b) = -2.5 mm, (c) = -1 mm, (d) = 0 mm, (e) = 1 mm, (f) = 2.5 mm, (g) = 4 mm. Right side: Rocking curves relative to each position as specified by the photo on the left. X-axis is the angle between X-rays and crystallographic planes.

Figure 2.2: Photo of a grooved sample, with crystallographic orientation.

Figure 2.3: Interferometric measurement of the backside of a grooved sample. Left side: 3d view analysis (a). Right side: cross sections of the deformation pattern along x (b) and y directions (c), as taken on the center of the sample.

Table 2.1: Fabrication parameters of all samples

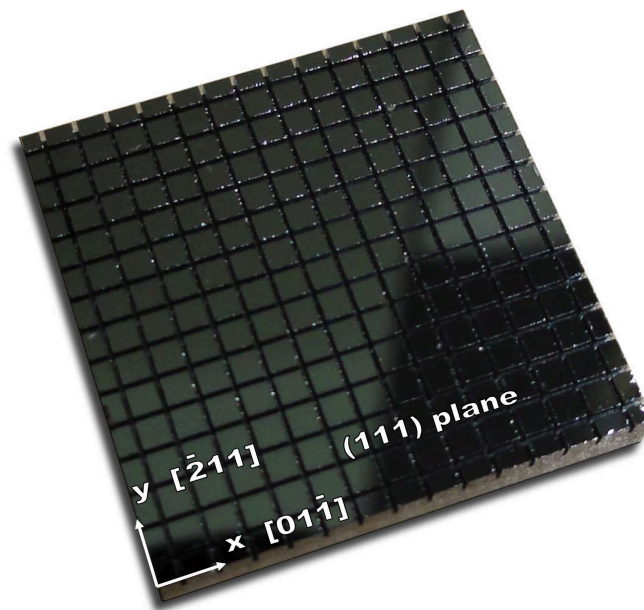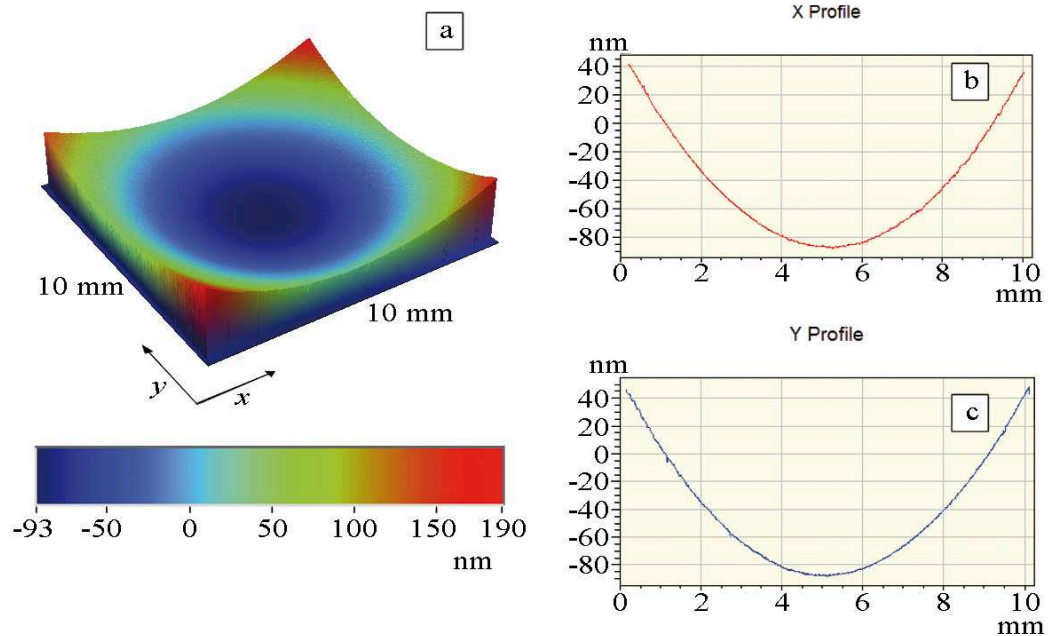| Material	Silicon
Thickness of plates	530 μm
	1030 μm
	1940 μm
Plates side length	10 mm
Blade specification	G1A 2000
Size diamond grains	2-4 μm
Blade width	160 μm
Groove speed	1 mm/s
Blade angular speed	40000 r.p.m.
Number of grooves	from 5×5 to 17×17
Grooves depth	variable

2.3   Linear elasticity and revisitation of the Stoney formula in anisotropic media

Surface grooving produces permanent plastic deformation in the neighborhood of the grooves [46]. Indeed, plasticization occurs in a thin layer of the crystal beneath and beside the grooves due to the dicing process. The extension of the plasticized layer results to be dependent on the grooving process. Such plasticized layer transfers coactive forces to the crystal bulk, thus producing an elastic strain field within the crystal.

A precise prediction and optimization of the crystal deformation needs a proper simulation of the internal state of stress in the structure. This can be obtained by observing that the plasticized layer-to-substrate interaction problem resembles that of a thin coating, which transfers interfacial tractions to the underlying substrate. It can be assumed that the plasticized layer behaves like a thin film deposited onto the surface of a crystal at the position of the superficial grooves.

A preliminary model, shown in [47], interpreted the effect of grooving as a compressive action exerted on the material between the grooves. A grooved plate was artificially divided into a compressive film with thickness equal to the depth of the grooves and an elastic unaltered substrate with the remaining material. Under this assumption, the Stoney formula was applied to describe the curvature of the plate. However, this simplification works only for relatively shallow grooves, which result in a moderately low curvature. For deeper grooves, a more realistic representation of the physical features of grooved plates is needed. Here it is provided a more effective

approach that holds true for any radius of curvature.

Indeed, the plasticized layer undergoes a compressive state of stress, whose intensity depends upon dicing parameters, i.e., advance speed of the blade, blade width and grit (dimension of diamond grains on the blade), number and depth of the grooves. Thus, mechanical deformation of the crystal can be assessed by solving a film-to-substrate interaction problem, in which a given level of compressive stress σ_f in the coating is imposed.

The curvatures of internal planes of a deformed crystal can be calculated through the displacement field as a function of $u(\mathbf{r})$, $v(\mathbf{r})$ and $w(\mathbf{r})$, which are the deformations along the x, y, and z axes, respectively. The normal (σ) and tangential (τ) components of stress tensor are bound up to mechanical momenta M_x and M_y applied to the crystal via

$$\sigma_x = \frac{M_x}{I}z, \quad \sigma_y = \frac{M_y}{I}z, \quad \sigma_z = 0 \tag{2.1}$$

$$\tau_{yz} = 0, \quad \tau_{xz} = 0, \quad \tau_{xy} = 0 \tag{2.2}$$

where I is the momentum of inertia. As known from the theory of homogeneous anisotropic thin plates subjected to bending, from the following boundary conditions,

$$\frac{dw}{dx}\Big|_0 = \frac{dw}{dy}\Big|_0 = 0, \quad \frac{dv}{dx} - \frac{du}{dy} = 0, \tag{2.3}$$

$$u(0) = v(0) = w(0) = 0 \tag{2.4}$$

the displacement field arising from the deformation of the crystal plate is

$$u = \frac{1}{2I}[M_x(S_{51}z^2 + S_{61}yz + 2S_{11}xz) \tag{2.5}$$
$$+ M_y(S_{52}z^2 + S_{62}yz + 2S_{12}xz)]$$

$$v = \frac{1}{2I}[M_x(S_{41}z^2 + 2S_{21}yz + S_{61}xz) \tag{2.6}$$
$$+ M_y(S_{42}z^2 + 2S_{22}yz + S_{62}xz)]$$

$$w = \frac{1}{2I}[M_x(S_{31}z^2 - S_{11}x^2 - S_{12}y^2 - S_{16}xy \tag{2.7}$$
$$+ M_y(S_{32}z^2 - S_{12}x^2 - S_{22}y^2 - S_{26}xy)]$$

where S_{ij} are the components of compliance tensor for anisotropic material referred to the (x, y, z) Cartesian system [31, 48]. u, v and w completely define the displacement field of the crystal plate. The relationship between the curvature of the middle plane of the plate and bending moments M_x, M_y (per unit length), uniformly distributed

along its sides, is

$$
\begin{aligned}
\frac{\partial^2 w}{\partial x^2} &= -\frac{6}{h_s{}^3}(2M_x S_{11} + 2M_y S_{12}), \\
\frac{\partial^2 w}{\partial y^2} &= -\frac{6}{h_s{}^3}(2M_x S_{12} + 2M_y S_{22})
\end{aligned}
\tag{2.8}
$$

h_s being the plate thickness.

The plasticized layer, which lies at $h_s/2$ from the middle plane of the plate (being $h_f << h_s$, see section 2.4), induces an interfacial stress distribution to the underlying crystal. As known from the film-to-substrate interaction problem, these interfacial tractions tend to concentrate in the neighborhoods of the film edges [49]. Particularly, for coatings compliant with respect to the substrate, an almost constant stress occurs in the film. Moreover, since the grooves were manufactured on the plate along x and y directions, taking into account the 90° rotational symmetry around z axis, it results

$$
-\frac{1}{R} = \frac{\partial^2 w}{\partial x^2} = \frac{\partial^2 w}{\partial y^2}, \qquad M_x = M_y = M \cong \sigma_f h_f h_s/2
\tag{2.9}
$$

h_f being the thickness of the plasticized layer and R the radius of curvature. From Eqs. (2.8) and (2.9), the relationship between film stress and curvature can be obtained as

$$
\sigma_f = \frac{h_s{}^2}{6(S_{11} + S_{12})h_f}\frac{1}{R}.
\tag{2.10}
$$

It is worth noticing that Eq. (2.10) corresponds to the classical Stoney formula (2.11) for an isotropic film-to-substrate system under equi-biaxial plane stress, which relates the stress level in the film to the local curvature of the substrate via [50]

$$
\sigma_f = \frac{E_s h_s{}^2}{6(1 - \nu_s)h_f}\frac{1}{R}
\tag{2.11}
$$

where E_s and ν_s are the Young modulus and Poisson ratio of the substrate, respectively. Indeed, Eq. (2.10) is retrieved from Eq. (2.11) provided that the anisotropy of the substrate is taken into account, i.e., $E_s = 1/S_{11}$, $\nu_s = -S_{12}/S_{11}$.

However, due to the presence of the grid of grooves, the plasticized regions on the crystal surface are not continuous (see Fig. 2.4), thus Eq. (2.10) should not be applied. Nonetheless, as showed in [51], Stoney formula can simply be extended to a system with nonuniform curvature if the effective level of plasticization is considered. In particular, for a symmetric distribution of grooves on a crystal, the mean radius of
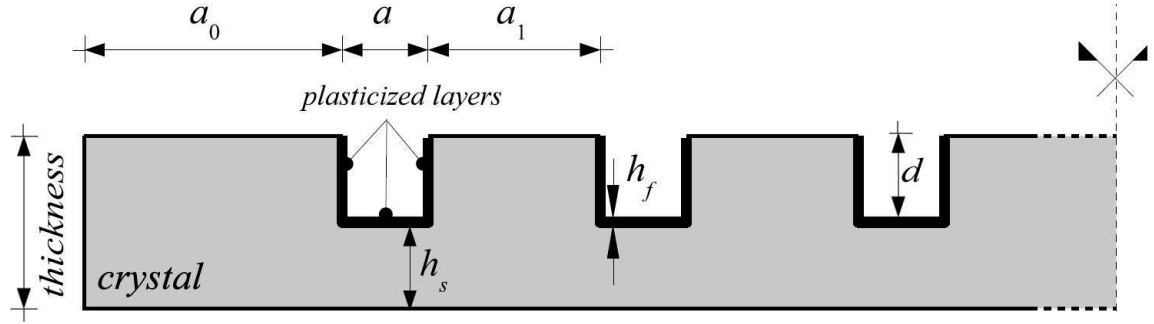
Figure 2.4: Schematic representation of a grooved crystal, section view. Film thickness, h_f, substrate thickness, h_s, groove depth, d and sample thickness are highlighted. a_0 is the distance between the crystal edge and the first groove, a the groove width and a_1 the distance between the grooves.

curvature $\overline{R}$ can be expressed as a function of the geometric parameters of the system

$$\overline{R} = \frac{l^2 R}{4a\chi}, \tag{2.12}$$

$$\chi = aN^2 + 2a_0 N + N(N-1)a_1 + \kappa\left(\frac{a}{4} + aN + a_0 + a_1 N\right) \tag{2.13}$$

where l is the crystal lateral dimension, N the integer number of grooves lying on half of the plate and κ is a coefficient, which takes into account the presence of a groove placed on the axis of symmetry, i.e., if the number of grooves is odd, $\kappa = 1$, else $\kappa = 0$. Eqs. (2.12) and (2.13) were obtained by superposing the bending effect due to each groove through the principle of virtual work applied to the grooved plate [31]; thus, a proper relationship among the local curvatures $1/R$ and the mean curvature $1/\overline{R}$ producing the same transversal deflection of the system was found.

Hence, from Eqs. (2.10), (2.12) and (2.13), it results

$$\overline{R} = \frac{l^2 h_s^2}{6(S_{11} + S_{12})\sigma_f h_f 4a\chi}. \tag{2.14}$$

2.4   Results and Discussion

Plasticization of the surface with grooves operated by a blade with diamonds grains (grit) has already been investigated through Raman spectroscopy [46]. Results proved that the plasticized layer is very localized, its thickness being comparable to the grit
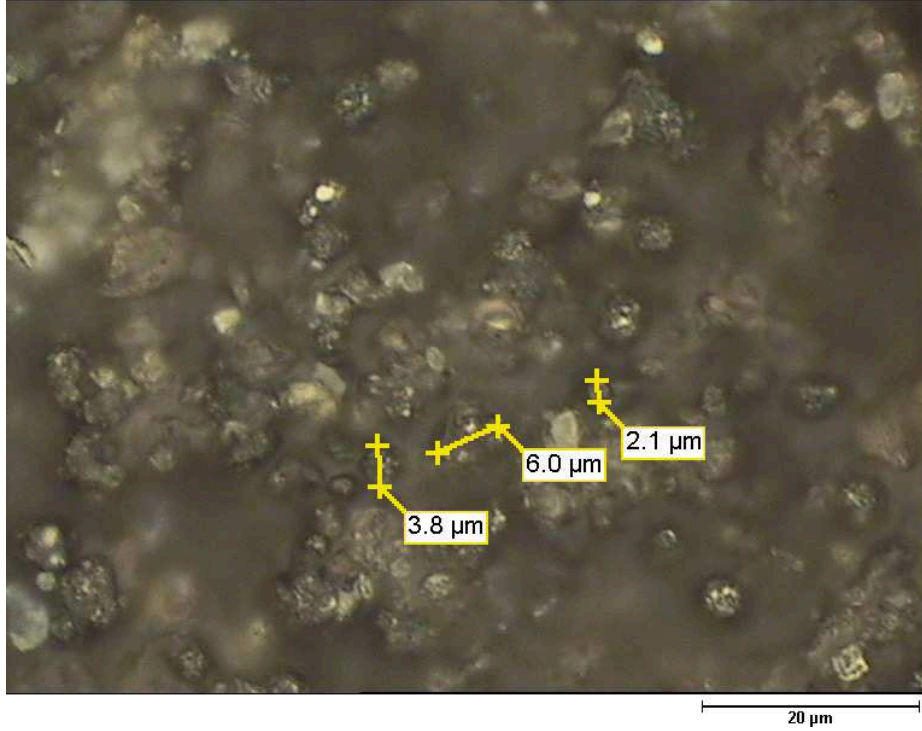
Figure 2.5: Photo of a typical blade obtained through optical microscopy. Dimensions of some diamond grains are highlighted.

size. Therefore, the thickness of the plasticized layer (h_f) can be directly controlled by simply varying the blade grit. As can be noticed in Fig. 2.5, where the size of some diamond grains is highlighted, it is reasonable to set h_f to be 5 μm, thus to make it possible the determination of σ_f. In any case, the only quantity that can not be measured directly in Eq. (2.14) is $\sigma_f h_f$. However, the following elaborations will be made in terms of $\sigma_f h_f$, therefore precise knowledge on σ_f and h_f individually is not crucial.

Under the assumption of the plasticized layer as a compressive film deposited on the surface of an unaltered crystal substrate, the curvature radius of grooved samples can be obtained through Eq. (2.14). In order to prove this hypothesis, a systematic production and characterization of grooved samples was worked out. Analysis was carried out on square Si plates with 10 mm lateral dimension patterned with a grid of 9×9 grooves on one of their surfaces. To deepen our study, different plate thicknesses (0.53, 1.03 and 1.94 mm) were investigated. In Fig. 2.6, the curvature radius is shown as a function of the groove depth.

For every grooved sample, the value of σ_f was calculated by simply reversing Eq. (2.14). Three averaged values, $\sigma_{f1} = 38.4\ MPa$, $\sigma_{f2} = 38.6\ MPa$ and $\sigma_{f3} = 38.8\ MPa$ were obtained for three set of samples with thickness 0.53, 1.03 and 1.94 mm,

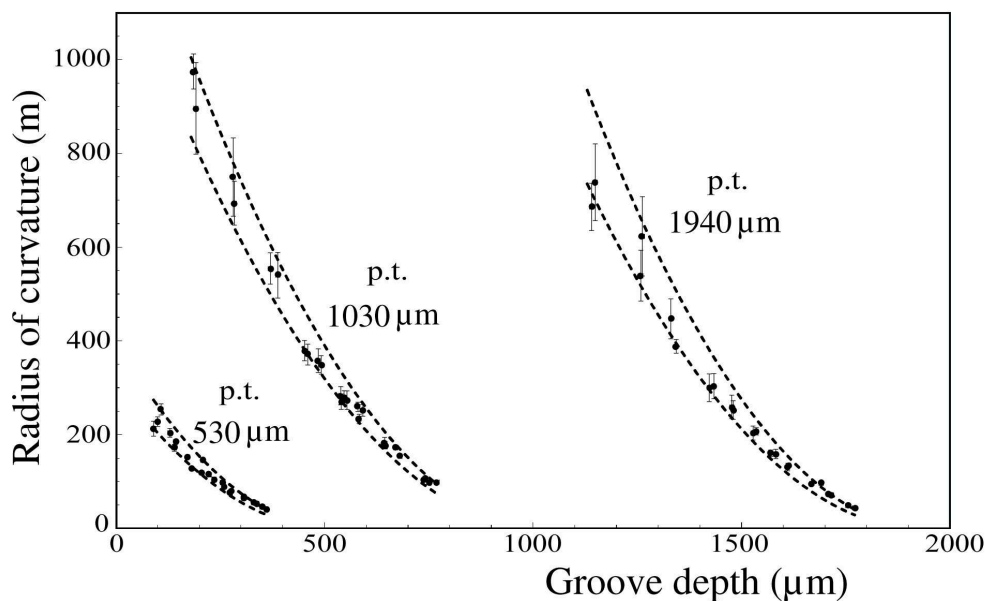Figure 2.6: Mean radius of curvature ($\overline{R}$) of grooved plates with variable depth for a grid of 9×9 grooves. The black points represent the measured samples with uncertainty bars. Theoretical expectation (dashed lines) was calculated taking into account the uncertainty on σ_f. Plates thickness (p.t.) was 530, 1030 and 1940 μm.

respectively. Since σ_{f1}, σ_{f2} and σ_{f3} are very close to each other, the existence of a single value for $\sigma_f = 38.6\ MPa$, valid for all samples, can be inferred. This fact confirms that σ_f does not depend upon the plate thickness but only on the grooving process, in agreement with theoretical expectations.

According to the model, the mean radius of curvature in Eq. (2.14) is expected to depend on h_s, rather than on the plate thickness. In order to prove the h_s dependence, the same data were plotted vs. h_s (Fig. 2.7). As can be seen, experimental data are again in close agreement with the expectation of the model.

The model was also verified by measuring the radius of curvature as a function of the number of grooves on 10×10×0.5 mm^3 Si plates. Groove depth was kept fixed at 258 μm with 10 μm of uncertainty. The other physical quantities of interest are reported in Tab. 2.2 and experimental results are shown in Fig. 2.8. The Fig. 2.8 highlights that good agreement between experimental data and theoretical expectation exists, as given by Eq. (2.14).

In summary, the state of stress and curvature in the samples are completely determined by the effect of plasticization due to the sawing process. Moreover, it was found out that the sequence by which the grooves are made does not influence the stress distribution, meaning that the resulting curvature solely depends upon the final
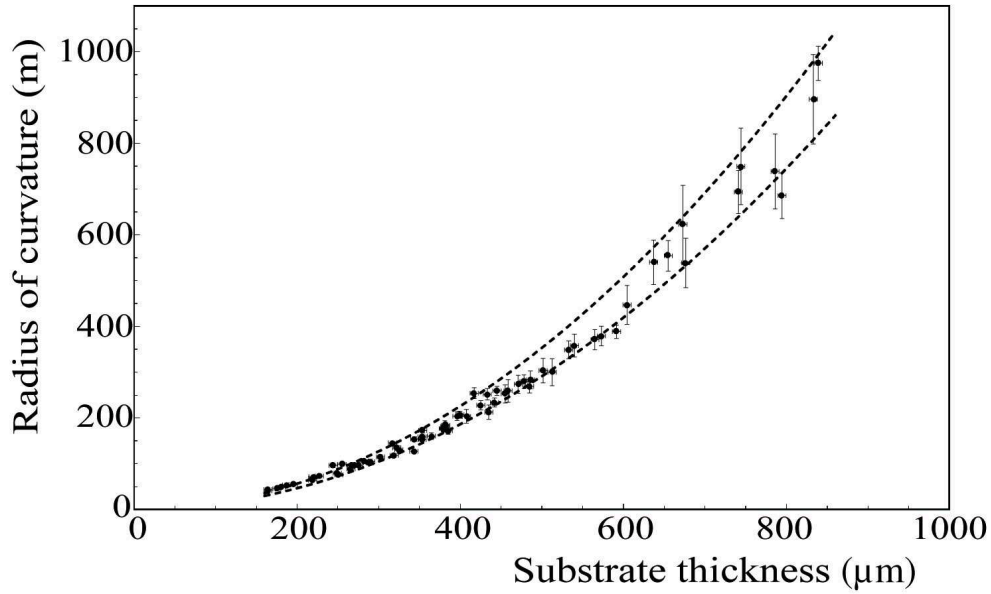
Figure 2.7: Mean radius of curvature ($\overline{R}$) of grooved plates with variable substrate thickness (h_s) for a grid of 9×9 grooves. The black points represent the measured samples with uncertainty bars. Theoretical expectation (dashed lines) was calculated taking into account the uncertainty on σ_f. Plates thickness was 530, 1030 and 1940 μm.

Figure 2.8: Mean radius of curvature ($\overline{R}$) of grooved plates with variable number of grooves. The black points represent the measured samples with uncertainty bars. Theoretical expectation (dashed lines) was calculated taking into account the uncertainty on σ_f. Plates thickness was 530 μm and the groove depth was 258 μm.

Table 2.2: Features of the samples shown in Fig. 2.8

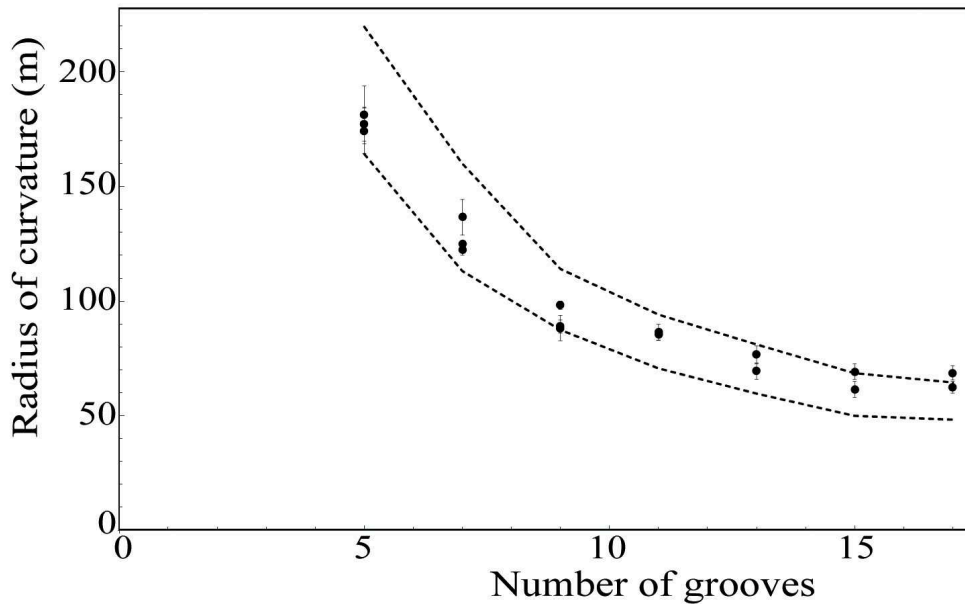| Number of grooves	a (mm)	a_0 (mm)	a_1 (mm)
5×5	0.16	0.72	1.94
7×7	0.16	0.72	1.24
9×9	0.16	0.72	0.89
11×11	0.16	0.72	0.68
13×13	0.16	0.42	0.59
15×15	0.16	0.37	0.49
17×17	0.16	0.36	0.41
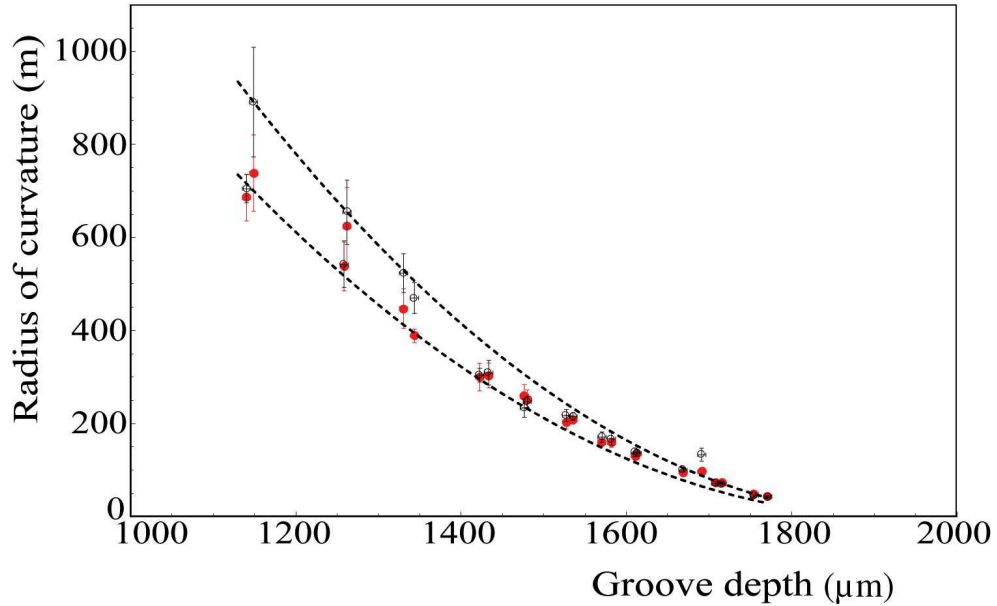
Figure 2.9: Mean radius of curvature $(\overline{R})$ of grooved plates with variable depth for a grid of 9×9 grooves. Empty black circles represent the measured grooved side of samples with uncertainty bars, while filled red circles represent the measured back side of samples with uncertainty bar. Theoretical expectation (dashed lines) was calculated taking into account the uncertainty on σ_f. Plates thickness was 1940 μm.

configuration of the grooves.

A crucial question for applications is whether or not the strain propagates deep into the substrate. Thereby, deformation was investigated on the grooved faces of the samples and compared to their respective backfaces. A systematic study was carried out on a $10\times10\times2$ mm^3 Si plates with a grid of 9×9 grooves on one of their surfaces. Fig. 2.9 contains the curvature radii measured on both faces of each sample. Both values agree to each other and to the general trend of the curve within the margin of

uncertainty, thereby a uniform curvature of the crystalline planes within the samples can be inferred.

2.5   Conclusions

A precisely determined bending of Si plates was obtained thanks to the method of grooves. An extensive study through the systematic production and characterization of grooved silicon samples was performed. It was demonstrated that the deformation affects the whole crystal, the curvature of opposite sides of the crystal being the same as far as experimental uncertainty is concerned. Not self-equilibrated residual stresses in the layer affected by the sawing process result in self-standing bent crystal. Grooved crystals can be used in manifold applications, especially those where weight constraint is mandatory, because no external mechanical device can be tolerated. Example of these applications are the realization of a Laue lens for nuclear medicine, homeland security or satellite-borne experiments in astrophysics.

The curvature of grooved samples can be foreseen with a model, that is based on the assumption that the plasticized layer behaves as a compressive film. Then, the Stoney approach was used to determine the curvature of grooved samples.

The method of grooves appears to be of widespread application and could be used to bend other materials than silicon. In fact, in the next sections, it will be demonstrated that germanium also behaves accordingly. An advantage of the developed model is that it purely relies on macroscopic physical quantities.

CHAPTER 3

Diffracting hard X-rays with high efficiency: the geometry 1

3.1 Grooved crystals for high-efficiency diffraction

Silicon mono-crystals were bent thanks to a series of parallel superficial grooves on one of the largest faces of the crystals. Grooved Si crystals were characterized at the European Synchrotron Radiation Facility (ESRF) in Grenoble, using a monochromatic beam ranging from 150 to 700 keV. Crystals exhibited very high diffraction efficiency over a broad range of energy, reaching 95% at 150 keV. The measured angular spread of the diffracted beam was always very close to the morphological curvature of the sample under investigation, proving that the energy passband of bent crystals can be controlled by simply imparting a selected curvature to the sample. The grooving method was found to offer high reproducibility and easy control of diffraction properties of the crystals. In the next sections, an on-beam systematic study to probe their performance vs. diffraction of high-energy photons is shown.

3.2 Experimental

Commercially available pure Si wafers were diced to form plates using the DISCO^{TM} DAD3220. The samples were bent through the grooving method, as explained in chapter 2. Grooves were manufactured on the surface of the plates along one direction, i.e., either x or y (Fig. 3.1a). All plates were 1 mm thick with the orientation of the largest surfaces being (111). Fabrication parameters of all the samples are reported in Tab. 3.1 and an image of one of the samples is shown in Fig. 3.2. For every crystal,
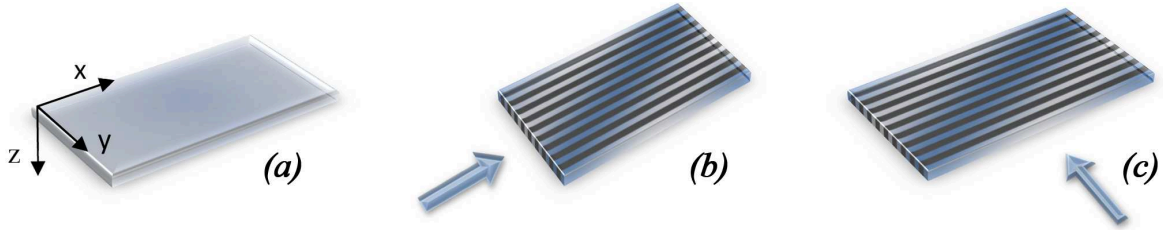
Figure 3.1: Grooves were manufactured on the surface of a Si plate along one direction, either x or y (a). The probe X-ray beam enters the sample parallel (b) or perpendicular (c) to the grooves

Table 3.1: Fabrication parameters of all the samples

Code	**S24**	**S31**	**S71**	**S72**	**S81**
Size (mm^3)	9.8×9.8×1	12.2×12.2×1	25.5×25.5×1	25.5×36.6×1	54.2×30.6×1
Number of grooves	15	15	31	25	30
Direction of grooves	[110]	[110]	[110]	[211]	[110]
Pitch of grooves (μm)	650	780	790	1000	1000
Depth of grooves (μm)	500	500	500	400	400
Blade	very hard	hard	hard	hard	hard

the curvature induced by grooves was measured through optical profilometry. Once the initial non-planarity of the samples has been taken into account, profilometry was done on the back face of the grooved plates. An ellipsoidal surface was recorded, with the shortest radius of curvature perpendicular to the grooves. A typical profilometric pattern of one of the samples is shown in Fig. 3.3. Production and optical characterization of all samples were carried out at the Sensor and Semiconductor Laboratory.

All samples were tested through X-ray diffraction during a 6-day run at beamline ID15A of ESRF. A highly monochromatic and quasi-parallel beam was tuned to the desired energy, ranging from 150 to 700 keV, thanks to a two-reflection Laue Si (111) unbent monochromator. Monochromaticity was of the order of $\Delta E/E = 2 \times 10^{-3}$. The sample holder was set far enough from the detector in order to allow for sufficient separation of diffracted and transmitted beams even at the highest energy. The characterization of the samples was carried out by performing rocking curves (RCs), i.e.,
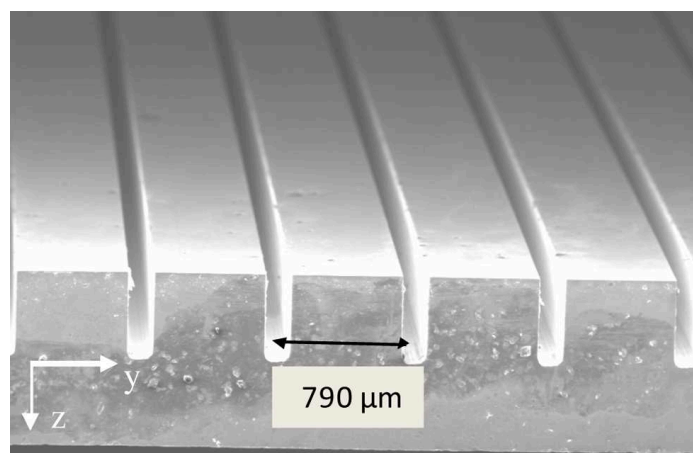
Figure 3.2: Side view of sample S71 with a series of grooves as taken by scanning electron microscope. The black arrow indicates the pitch of the grooves

by recording either the transmitted or diffracted beam intensity while the crystal was being rotated in the beam around the position where the Bragg condition was satisfied. Diffraction and transmission RCs were recorded one after the other, resulting in two complementary curves as a function of the beam incidence angle. The full width at half maximum (FWHM) of the RC was a direct measurement of the angular distribution of diffracting planes (hereinafter referred to as angular spread), namely the bending angle of the crystal. In all the cases above mentioned, the Bragg angles were small. Therefore, a possible broadening of the RCs due to a variation of the lattice parameter can be negligible. Furthermore, the shape of the RCs was not modified by extinction phenomena, which are negligible in such bent crystals. The RCs also exhibits the diffraction efficiency of the sample under analysis. For comparison with previously published measurements, efficiency was defined as in Ref. [52], namely the ratio of diffracted beam intensity over the transmitted one. Transmitted beam intensity was recorded by keeping the sample under diffraction condition and shifting the detector in such a way to measure the beam intensity passing through the crystal without undergoing diffraction.

All samples were analyzed by diffraction with their (111) planes, the pencil beam entering the sample at different depths from the grooved surface (coordinate z). Two different configurations were used, i.e., the beam was set quasi-parallel (hereinafter referred to as parallel) or perpendicular to the grooves, its size being 50×50 μm^2 and 100×50 μm^2, respectively. A sketch of the two configurations is shown in Figs. 3.1b and 2c.
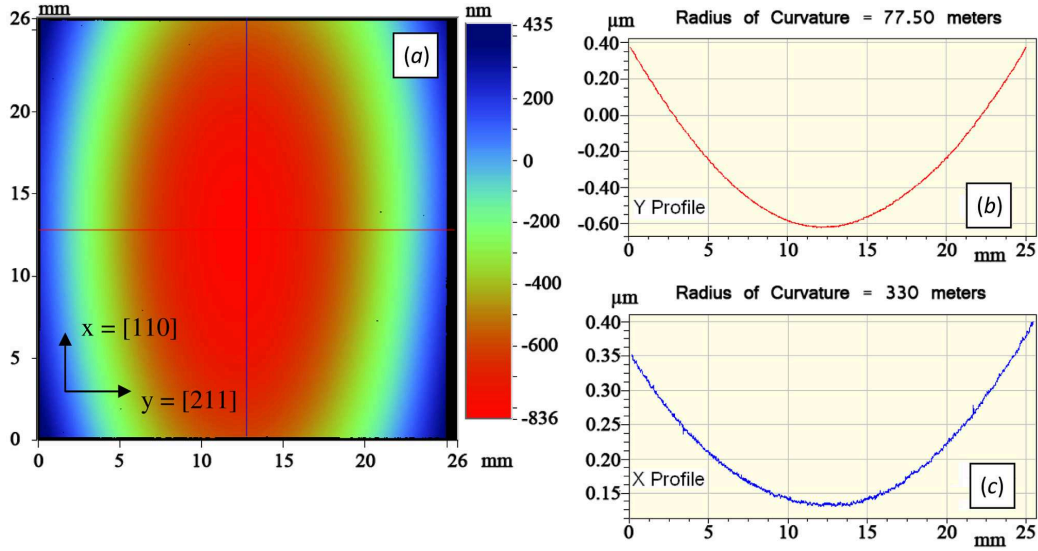
Figure 3.3: Optical profilometry scanning of the surface without grooves of crystal S71 (a). False-color representation of deformation is highlighted. Cross sections of the deformation pattern along $y = [211]$ (b) and $x = [110]$ (c) directions as taken on the center of the sample with indications of the two main curvature radii

Table 3.2: Main performance of all the samples under investigation

Code	S24	S31	S71	S71	S72	S81
Photon energy (keV)	150	150 - 500	150 - 700	150 - 500	150- 600	300
Beam configuration	Perp. to the grooves	Perp. to the grooves	Par. to the grooves	Perp. to the grooves	Perp. to the grooves	Par. to the grooves
Bending angle (arcsec)	32.2	35.1	15.7	66.6	55.0	29.5
Angular spread (arcsec)	26.2	23.6	14.1	57.1	49.9	25.7
Max. diffraction efficiency at lowest energy	81.7%	69.1%	94.9%	71.1%	79.4%	86.4%
Averaged diffraction efficiency at lowest energy	54.9%	51.1%	93.4%	56.1%	60.3%	81.8%

Finally, experimental data were analyzed and compared to theoretical expectations through a custom-made software specifically designed for bent crystals and inspired from the code in Ref. [23].

3.3   Results and discussion

The main characteristics of each measured sample are summarized in Tab. 3.2. Here the features of sample S71 are extensively described, since more significant. The crystal was initially measured at 150 keV with the beam penetrating the sample through its $25.5{\times}1$ mm^2 surface at different depths from the grooved side, parallel and perpendicular to the grooves. Bending angles of the sample, as measured by optical profilometry, averaged 15.7 and 66.6 arcsec along the [110] and [211] directions, respectively. Fig. 3.4 shows both diffracted and transmitted RCs as normalized to transmitted beam intensity (so that diffraction efficiency is readily displayed).

All RCs exhibited flat-topped and uniform shapes with FWHM of the order of crystal bending, i.e., it averaged 14.1 and 57.1 arcsec for the parallel and perpendicular cases, respectively. This sample featured significantly high efficiency when the beam was parallel to the grooves, highlighting very homogeneous diffraction pattern with efficiency about 93.4% over the whole depth. This performance highlights that a bent crystal can amply break the 50%-efficiency limit, which holds indeed for a mosaic crystal. With the beam perpendicular to the grooves, diffraction efficiency was still a good performance though it varied over the crystal depth, i.e., it was nearly 50% close to the grooved region, and raised up to 71% deeper into the crystal. Such features are better pointed out in Figs. 3.5a and 3.5b, where diffraction efficiency is shown as a function of coordinates z and y (z and x), for the parallel (or perpendicular) case. Efficiency resulted constantly close to the unity in the parallel case while it smoothly varied over the whole depth for the other configuration. However, no dependence on coordinate y (or x) was recorded in any case. The same dependence was recorded for angular spread for the parallel and perpendicular cases (Fig. 3.5c and Fig. 3.5d, respectively). It follows that the curvature was uniform along coordinate y (or x), though its dependence on coordinate z showed different profile. Indeed, as the distance from the grooved face increased, the angular distribution slightly increased for the parallel case. Perpendicularly to the grooves, the variation of the angular spread within the crystal was stronger, i.e., it increased across the groove depth and decreases outside. This evidence can be ascribed to the fabrication process of grooving. In fact, generation of mosaicity perpendicularly to the advance speed of the blade is easier to form than longitudinally because of the stronger action exerted by the blade on

the side walls of the groove. This effect leads to an increase in angular spread, and consequently in energy bandwidth, resulting in efficiency decrease throughout the whole depth of the grooves. Indeed high efficiency was restored beneath the grooves, meaning that the curvature of diffracting planes was homogeneous and its structure was not significantly affected by mosaicity.

Finally the sample was measured at several energies, the beam entering the crystal far from the grooved region, parallel and perpendicular to the grooves. RCs are shown here for parallel case (Fig. 3.6). The sample featured significant diffraction efficiency up to 700 keV, ranging from 92% down to 29%. With the beam perpendicular to the grooves, efficiency keeps lower than 60% above 200 keV. Next section compares experimental performance to theoretical expectations, showing that the decrease in efficiency with energy is completely in agreement with the dynamical theory of diffraction [25].

3.4   Simulations

In order to deepen our understanding of diffraction properties of the samples, a simulation code was developed. The software describes diffraction in both curved and mosaic crystals and generates the physical quantities of interest. Such quantities, typically used to qualify the diffraction properties of a crystal, are diffraction efficiency and reflectivity. Reflectivity is defined as the ratio of diffracted beam intensity over incident beam intensity. For any set of parameters such as crystalline material, set of reflection planes and thickness of curved or mosaic crystal, the code computes reflectivity and diffraction efficiency as a function of photon energy and angular spread (or mosaicity). Expected performance is then compared to experimental data. The diffraction efficiency for mosaic and CDP crystals was calculated with Eqs. 1.2 and 1.5.

As in previous section, the results of the simulations will be shown here for sample S71. In Fig. 3.7, experimental diffraction efficiency vs. z is compared to the theoretical efficiency in case of a perfectly curved crystal and a mosaic crystal. These latter were calculated taking into account the FWHM of the RCs, thus an experimental uncertainty is included. Due to generation of mosaicity perpendicularly to the grooves, measured efficiency varies over the crystal depth, being always lower than the theoretical limit for a perfectly bent crystal, especially under the grooves. However, this performance keeps always higher or at worst equal to the theoretical efficiency for a mosaic crystal, meaning that the grooves allow obtaining a homogeneous curvature with no significant damage of the crystal. In order to better understand the behavior
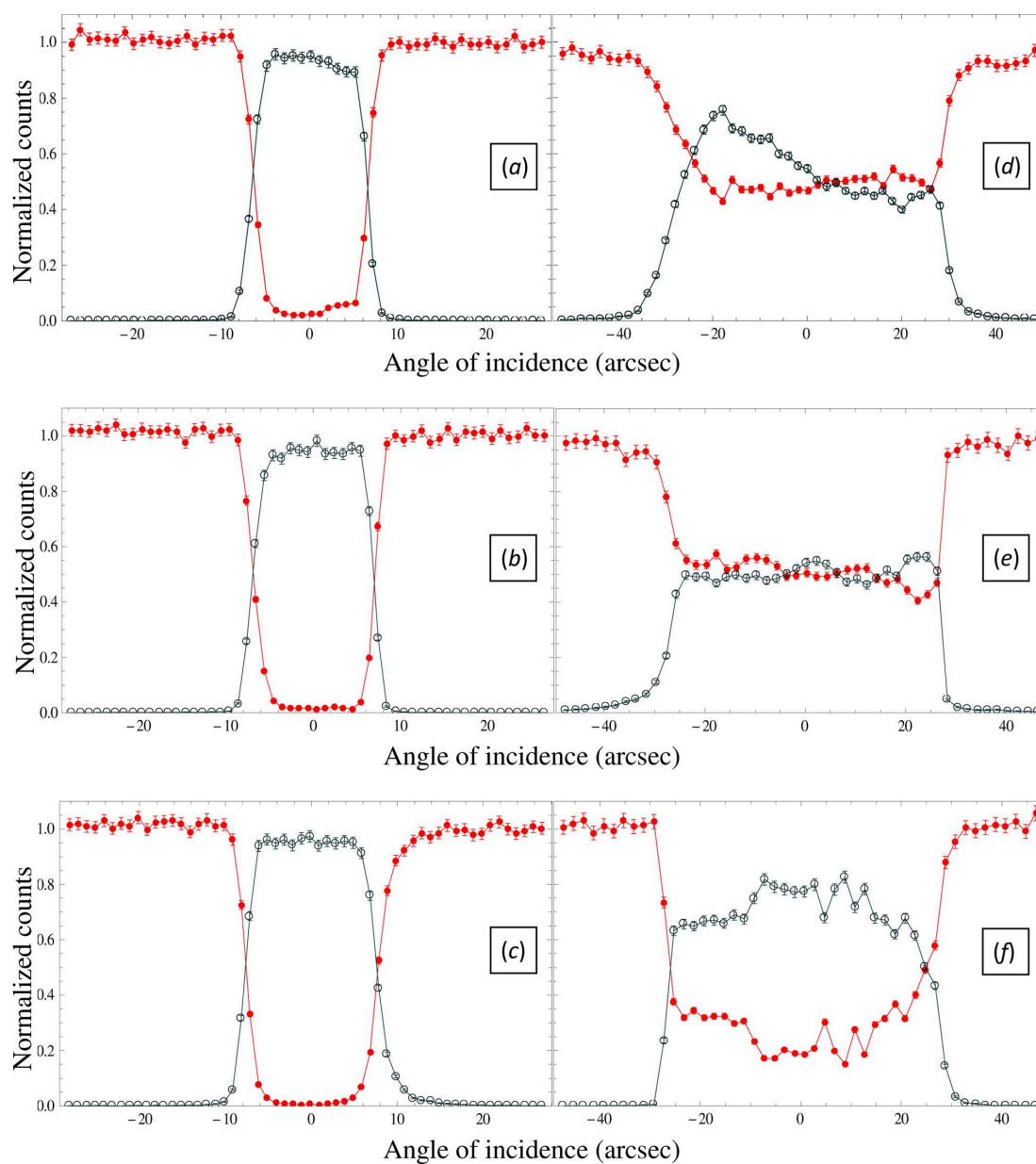
Figure 3.4: RCs of crystal S71 with the beam parallel to the grooves at several distances from the grooved face, at (a) $z = 0.4$ mm, (b) $z = 0.6$ mm, (c) $z = 0.8$ mm; the RCs were recorded at $y = 13.9$ mm. RCs with the beam perpendicular to the grooves at (d) $z = 0.15$ mm, (e) $z = 0.55$ mm, (f) $z = 0.85$ mm; the RCs were recorded at $x = 15$ mm. The filled red circles plot the intensity of the transmitted beam, whereas the empty blue circles plot the intensity of the diffracted beam. RCs with rectangular and homogenous shapes were achieved, with an energy passband of the order of crystal bending (about 16 arcsec for the parallel case and 57 arcsec for the perpendicular case). Efficiency is close to the unity in the parallel case. Notice that in (d) the sum of the transmitted and diffracted beams is bigger than 1 in the left part of the RCs. This artefact is due to the proximity of the surface where the diffracted beam leaves the crystal, thus the path of the diffracted beam does not cross the whole thickness of the crystal, resulting in smaller absorption.
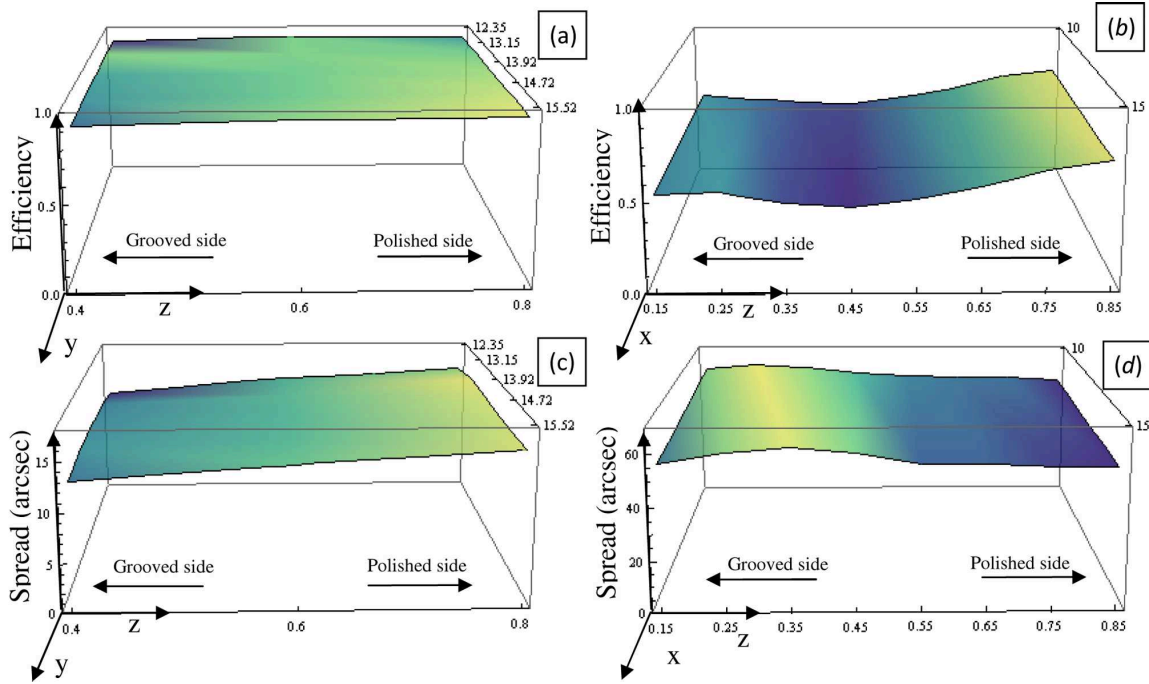
Figure 3.5: Diffraction efficiency of crystal S71 vs. coordinate z (mm) at several positions within the crystal (coordinate y or x) for parallel (a) and perpendicular (b) cases. Same dependence of angular spread is shown for parallel (c) and perpendicular (d) cases. No dependence on coordinate y (or x) was recorded in any case. Efficiency near the polished side of the sample is close to the unity while it gently decreases close to the grooved side in the parallel case and more strongly in the perpendicular case.

of diffraction response, the crystal was modeled as it were made by two coexisting structures at any coordinate z, i.e., a mosaic crystal and a perfectly curved crystal. Based on this model, diffraction efficiency was considered as the superposition of the contributions of the two kinds of crystal. Here, $C(z)$ is the fraction of perfectly curved crystal-like behavior and $[1-C(z)]$ the contribution of mosaicity, such that

$$\eta(z) = C(z)\eta_C + [1 - C(z)]\eta_M \qquad (3.1)$$

where $\eta(z)$ is the experimental diffraction efficiency obtained at a given distance from the top of the crystal, η_C the expected diffraction efficiency for a perfectly curved crystal and η_M the expected diffraction efficiency in case of a mosaic crystal. As a result, for the perpendicular case the fraction of mosaicity $[1-C(z)]$ is close to the unity in the region of the grooves, and vanishes outside. For the parallel configuration the mosaicity fraction keeps about 8% throughout the entire thickness of the sample. Indeed, in the parallel case, experimental efficiency is constantly close
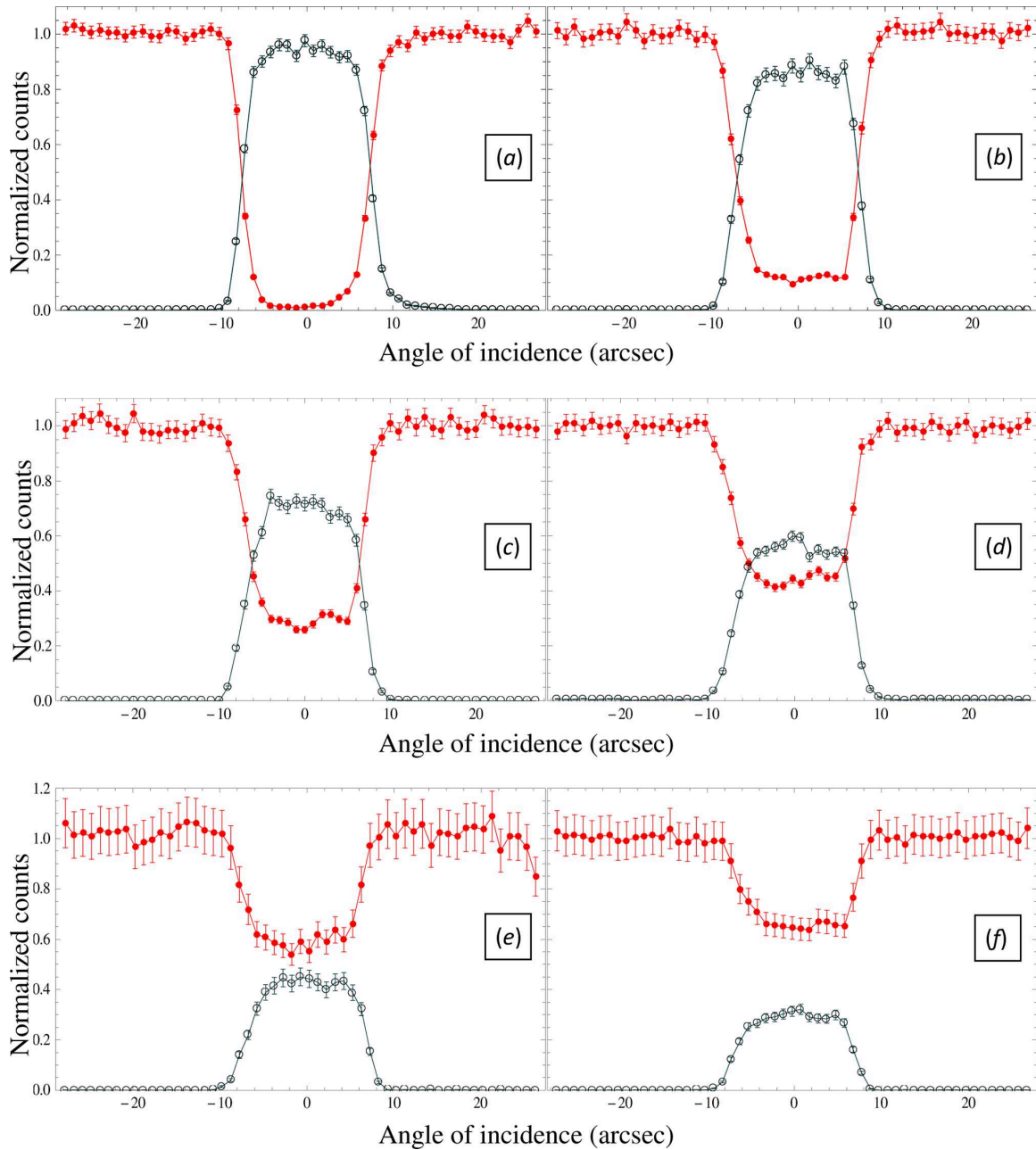
Figure 3.6: RCs of crystal S71 with the beam parallel to the grooves, measured at $z = 0.8$ mm and $y = 13.9$ mm. Beam energy was set at 200 keV (a), 300 keV (b), 400 keV (c), 500 keV (d), 600 keV (e) and 700 keV (f). The filled red circles plot the intensity of the transmitted beam, whereas the empty blue circles plot the intensity of the diffracted beam. Efficiency falls off with photon energy according to the dynamical theory of diffraction though a rectangular shape of the distribution is preserved.
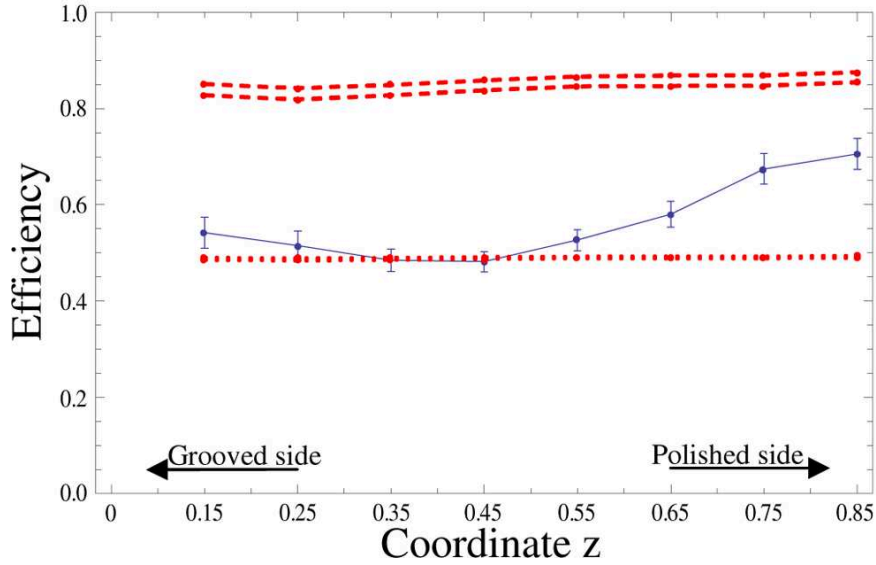
Figure 3.7: Experimental efficiency (blue circles) vs. coordinate z (mm) for crystal S71 with the 150 keV probe beam perpendicular to the grooves. Red dashed and dotted lines represent theoretical efficiencies in case of a curved and of a mosaic crystal, respectively. An experimental uncertainty is included in both cases. Due to generation of mosaicity, experimental efficiency varies within the crystal, being lower over the whole groove depth and increasing outside. However, diffraction efficiency is always higher or at worst equal to the theoretical contribution given by a mosaic crystal.

to the theoretical limit of a perfectly curved crystal.

Diffraction efficiency was studied vs. photon energy. Fig. 3.8 shows the response of sample S71, measured with the beam parallel and perpendicular to the grooves. In the parallel case (Fig. 3.8a), experimental efficiency is very close to its theoretical limit over about 15 arcsec angular spread, namely the morphological curvature of the sample. With the beam perpendicular (Fig. 3.8b) to the grooves, efficiency is slightly lower than its theoretical limit though still higher than the theoretical efficiency for a mosaic crystal.

A behavior similar to that of sample S71 was observed by all the samples in Tab. 3.2, this being a representation of the high reproducibility of the grooving method.

3.5   Discussion

The grooving method proved to yield a self-standing homogeneous and controlled curvature in Si (111) crystals. The crystals showed significantly high efficiency and

Figure 3.8: Experimental and theoretical diffraction efficiencies vs. energy, for parallel (a) and perpendicular (b) cases for crystal S71. RCs were carried out at 0.8 mm and 0.85 mm from the gr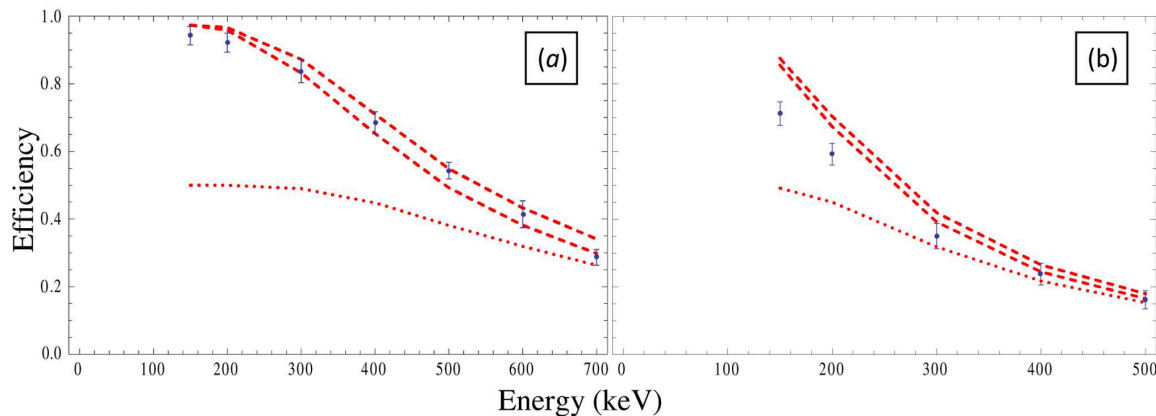ooved face for parallel and perpendicular cases, respectively. Theoretical efficiency (red dashed line) was calculated taking into account the FWHM of the RCs, thus an experimental uncertainty is included. Measured diffraction efficiency is represented by blue circles with their error bars. Red dotted line represents theoretical efficiency for a mosaic crystal with mosaicity equal to the FWHM of the RCs.

broad-band response when subjected to X-ray diffraction. The morphological curvature measured by optical profilometry is in good agreement with the curvature of the crystalline planes as determined by X-ray diffraction. As a result, it can be inferred that the energy bandwidth of bent crystals can be very well controlled. Diffraction efficiency turns out to be different when the beam is parallel or perpendicular to the grooves and that is ascribed to a generation of stronger mosaicity perpendicularly to the grooves. Grooved Si crystals were shown to efficiently diffract up to 700 keV, proving that optics made of bent crystals can work on a wide energy range in the hard X / soft γ ray domain. However, at energies above 300 keV, crystals with higher atomic number may be more suitable to yield a even higher reflectivity.

The use of diffracting crystals disposed in geometry 1 requires the fabrication and the positioning of a large number of samples to cover the whole Laue lens, because the crystals must be oriented with their major faces parallel to the photon direction. A solution to this problem is given in [53]. In fact, a stack of bent crystals can be assembled as an optical element for X-ray focusing, as shown in Fig. 3.9. The bent samples were glued one over the other to form a stack, simply using hot-melt adhesive. The relative alignment of the curved diffracting planes in the stack was tested by hard X-ray diffractometry using a polychromatic and divergent beam. The experimental results are shown in [53, 54]. The stack exhibited a single and well defined spot under
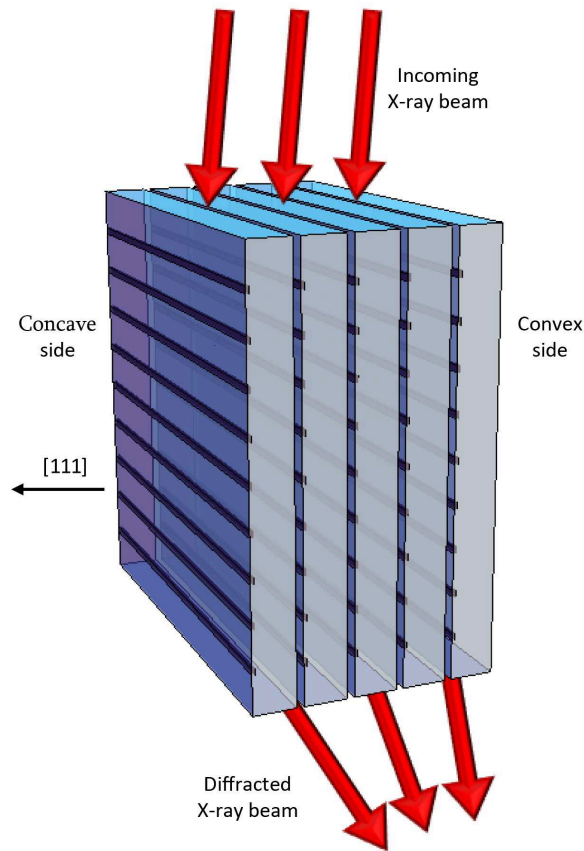
Figure 3.9: A stack of plate-like curved crystals is proposed as an optical component for focusing of X- and γ-rays. The crystal curvature arises from grooving of a surface of each plate. In the Laue lens scheme, high-energy photons enter nearly parallel to the CDP, suffer diffraction and undergo focusing onto the detector.

X-ray diffraction, highlighting that the plates were sufficiently aligned to behave as a single crystal. The curvature of the plates in the stack can be precisely set by tightly controlling the experimental parameters of grooving.

Thanks to the stacking, it would be possible to realize optical elements with arbitrarily large size, aiding the problem of positioning. However, the number of crystals needed to cover a whole Laue lens still remains the same, namely very large. Moreover, in order to employ stacked crystals for space-borne system, vibrations tests must be performed.

To overcome this problem, geometry 2 with curved crystals has been introduced, to expose the larger crystal surface to the photon flux. It is shown in the next chapters that, exploiting the quasi-mosaic effect in grooved crystals, it is possible to obtain bent Si and Ge samples capable of focusing the X-ray beam with high efficiency and high resolution.

CHAPTER 4

Diffracting hard X-rays with high resolution: the geometry 2

4.1 Quasi-mosaic crystals

Quasi-mosaicity is an effect of secondary bending within a crystal driven by crystalline anisotropy. This effect can be used to fabricate a series of curved crystals in geometry 2 for the realization of a Laue lens (see Figs. 4.1). It will be shown that crystals bent that present the quasi-mosaic effect allow very high-resolution focusing with respect to mosaic crystals. In particular, quasi-mosaic crystals would increase the signal-to-noise ratio up to one order of magnitude as compared to a Laue lens based on mosaic crystals with the same energy passband. Moreover, no mosaic defocusing would occur for quasi-mosaic crystals.

High-resolution focusing of diffracted photons within an energy range is an important requirement for all the applications involving a Laue lens. It is possible to use quasi-mosaicity for crystal bending, i.e., an effect of anisotropy in crystal deformation. In this configuration, bending results in a primary curvature generating a secondary curvature within the crystal due to quasi-mosaic effect. Usage of quasi-mosaic (QM) crystals allows positioning of the crystals in a Laue lens in the same way as for mosaic mosaic crystals, i.e., with the diffracting planes perpendicular to the major faces of the crystal (Fig. 4.1). For a Laue lens made by crystals with diffracting planes perpendicular to the major face of the crystal, focusing can be fully provided by bending the crystals to a primary curvature equal to that of the whole lens. But, even for such a curved crystal, if the diffracting planes were perfectly flat, the integrated reflectivity of the whole lens would be the same as for an unbent mono-crystal, i.e., a relatively

low figure. Indeed, by using QM crystals, it is possible to encompass the focusing action due to primary curvature with the high reflectivity of bent diffracting planes built up by quasi-mosaicity. Here it is also shown that since the size of the focal spot of the photons diffracted by a QM crystal can be controlled by the secondary curvature, QM crystals allow focusing with higher resolution with respect to mosaic crystals.
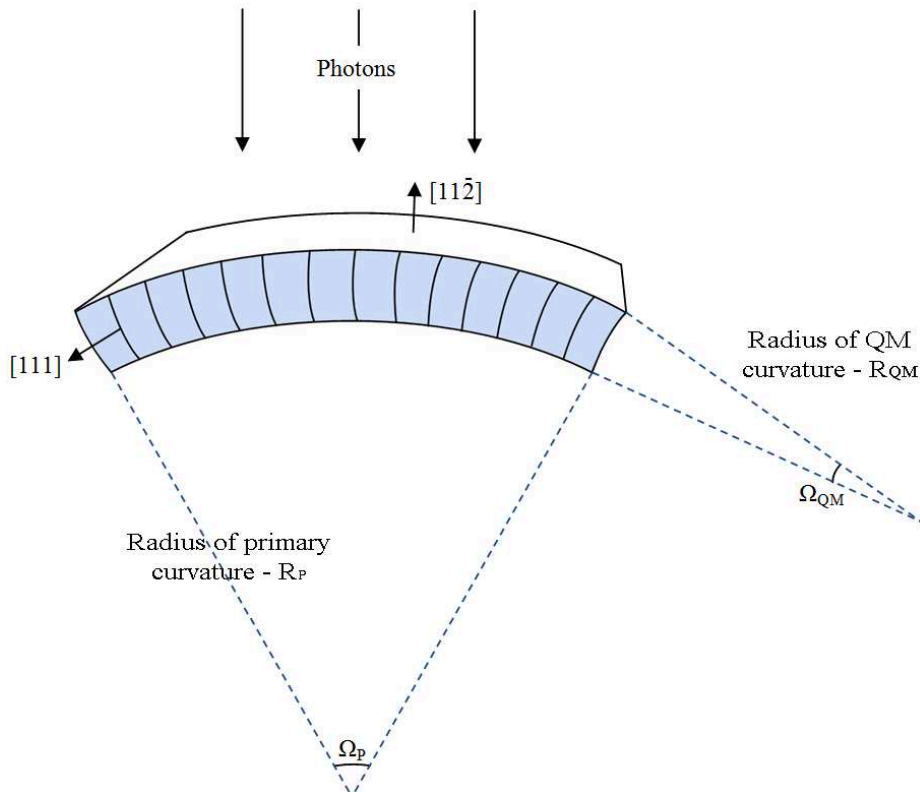
Figure 4.1: A primary curvature of a properly oriented crystal leads to a secondary curvature owing to quasi-mosaicity. For a Laue lens, quasi-mosaic curvature of (111) lattice planes resulting from primary bending of (11$\bar{2}$) crystal plates is proposed for diffraction of the radiation. In this configuration the (111) diffracting planes are perpendicular to the main surface of the plate, thus positioning of the crystals in the lens would be the same as for mosaic crystals. Ω_P and Ω_{QM} are primary and secondary bending angles, respectively.

4.2   Quasi-mosaicity in the theory of elasticity

Historically, quasi-mosaicity was discovered by Sumbaev and discussed in a seminal work [30]. More recently, this phenomenon was introduced by Ivanov [55] to bend Si
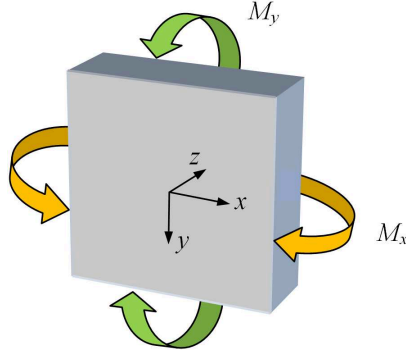
Figure 4.2: Schematic representation of a square crystal plate with the coordinate system used for the modelling. The bent arrows symbolize the applied momenta M_x and M_y.

crystals for steering high-energy particles via coherent effects in crystals, viz. planar channeling [43] and volume reflection [44]. However, such QM crystals do need an external device to maintain their curvatures. For satellite-borne experiments the usage of an external device would lead to excessive weight, thus self-standing bent crystals are mandatory for practical implementation of QM crystals in a Laue lens.

Quasi-mosaicity is fully understood in the framework of the theory of linear elasticity. A square crystal plate subject to a couple of mechanical momenta applied along x and y directions undergoes primary deformation (see Fig. 4.2). In this configuration, the curvatures of internal planes can be calculated through the displacement field as a function of space $u(\mathbf{r})$, $v(\mathbf{r})$, $w(\mathbf{r})$, which are the deformations along x, y and z directions, respectively.

Starting from EQs. 2.3 and by assuming $M_x = M_y = M$ (see Fig. 4.2), the primary curvature on the center of the plate surface, i.e., at $(0, 0, 0)$, holds

$$\frac{1}{R_P} = \frac{d^2 w}{dx^2} = -\frac{M}{I}(S_{11} + S_{12}) \text{ for } xz \text{ planes} \tag{4.1}$$

and

$$\frac{1}{R_P} = \frac{d^2 w}{dy^2} = -\frac{M}{I}(S_{12} + S_{22}) \text{ for } yz \text{ planes} \tag{4.2}$$

while the curvatures induced by quasi-mosaicity is

$$\frac{1}{R_{QM}} = \frac{d^2 v}{dz^2} = \frac{M}{I}(S_{41} + S_{42}) \text{ for } yz \text{ planes} \tag{4.3}$$

and

$$\frac{1}{R_{QM}} = \frac{d^2 u}{dz^2} = \frac{M}{I}(S_{51} + S_{52}) \text{ for } xz \text{ planes} \tag{4.4}$$

It follows that QM curvature occurs only if $(S_{41} + S_{42})$ or $(S_{51} + S_{52})$ is not zero, thus it manifests itself only along selected crystallographic directions. In particular for a diamond-like lattice, primary deformation of $(11\bar{2})$ planes results in QM deformation of (111) planes (Fig. 4.1). The ratio between QM and primary curvature along the radial direction of the lens holds

$$\frac{R_{QM}}{R_P} = \frac{S_{12} + S_{22}}{S_{41} + S_{42}} \tag{4.5}$$

For a high-efficiency diffraction by Si or Ge plates, (111) planes are normally selected because of their high reflectivity. Thus, it is proposed to bend $(11\bar{2})$ Si or Ge plates as a primary curvature, which results in secondary curvature of (111) diffracting planes aligned with the radial direction of the lens.

4.3 Discussion and simulations

In this section it is provided a performance comparison between mosaic vs. QM crystals, each of which used under optimal condition for practical implementation in a Laue lens with realistic data.

A mosaic crystal was consider with the shape of a square tile of size L_M and with a certain mosaicity Ω_M. If is assumed a parallel incoming beam impinging onto the crystal, the spatial distribution of the photons that are diffracted on the focal plane is given by the convolution of the tile size of the crystal with the normal distribution of the crystallites [27]. Thus, the square image of each mosaic crystal suffers from blurring due to mosaicity, the contribution of all the crystals of a whole ring being the overlap of the blurred images of all the crystal tiles.

The final pattern is dominated by one of the two effects in the convolution, depending on the proportion between mosaicity and the ratio between the tile size with the focusing length. If mosaicity is negligible the focal spot only depends on the tile size, if instead mosaicity dominates, the intensity of the focal spot is Gaussian-distributed. In practical cases, as in [27], mosaicity is not negligible though it is not the major effect.

With an individual QM crystal with tile size L_{QM}, it is possible to focalize the photons along the radial direction by simply bending the crystal to a primary curvature equal to that of the whole lens. In this case the focal spot is a rectangle with base

L_{QM} in the direction where focusing does not occur and height being determined by the quasi-mosaic curvature within the crystal. Under same conditions for the incoming beam and by assuming that the passband for photon energy for a mosaic crystal equals that for a QM crystal, it comes clear that the size of the spot on the focal plane is certainly smaller for a QM crystal than for a mosaic one.

To deepen this argument, simulations of focusing capability of QM *vs.* mosaic crystals was done. These were accomplished through both a Monte Carlo method and an analytical modelling. Firstly, for both kinds of crystals it is calculated the ratio between diffracted beam intensity and incident beam intensity, i.e., the reflectivity. For mosaic case, reflectivity is given by formula 1.2 [24]. Since QM crystals belong to a class of CDP crystals, then the ratio between diffracted and incident beams, i.e., the reflectivity η_{QM}, is given by the following formula as a result of the dynamical theory of diffraction [25]

$$\eta_{QM} = [1 - e^{\frac{-\pi^2 T_0 d_{hkl}}{\Omega_{QM} \Lambda_0^2}}] e^{\frac{-\mu T_0}{cos\theta_B}} \qquad (4.6)$$

where T_0 is the crystal thickness traversed by radiation, d_{hkl} the d-spacing of planes (hkl), θ_B the Bragg angle, μ the linear absorption coefficient within the crystal, Λ_0 the extinction length as defined in [26] for the Laue symmetric case and $\Omega_{QM} = \frac{T_0}{R_{QM}}$ represents the bending angle of the curved diffracting planes. With QM crystals, these latter are (111) planes, thus Ω_{QM} can be calculated as a function of the primary curvature through Eq. (4.5).

For the simulation, crystal tiles was considered to be disposed as concentric rings onto the spherical cap of a Laue lens with a certain focal distance f. The energy passband of a full ring is given by formula [56], which holds for both configurations

$$\Delta E \approx \frac{2\Omega E f}{r} \qquad (4.7)$$

where r is the radius of the ring and E the mean energy diffracted by a ring, depending on crystal reflection planes as given by formula [56]

$$E = \frac{hc}{2d_{hkl} \sin(\frac{1}{2} \tan^{-1}(\frac{r}{f}))} \approx 12.4 \frac{f}{d_{hkl} r} \qquad (4.8)$$

where the approximation of small angles was considered in last two formulae.

In order to provide a numerical comparison, an incoming photon beam with uniform energy distribution centered at E and with energy spread ΔE was considered to impinge parallel to the axis of the lens, this latter taken with a focal distance of 20 m and made of a single ring. E was investigated within the range 100-250 keV, which is

Table 4.1: Main features and results of the simulation at E=250 keV

	mosaic	quasi-mosaic
Material	Cu	Ge
Atomic number	29	32
ΔE (keV)	8.27	8.27
Number of rings	1	1
Ring radius (m)	0.475	0.304
Tile size (mm)	10.0	10.0
Tile thickness (mm)	6.5	2.4
Mass of crystals (kg)	1.71	0.24
Number of photons hitting the lens	10^6	633898
Mosaicity (arcsec)	81	-
r_{focus} at FWHM (mm)	5.8	0.47

an interval including both astrophysics and nuclear medicine. Hereinafter are explicitly given the parameters for optimization at $E = 250$ keV. Cu and Ge were chosen as materials for mosaic and QM cases, respectively. This choice of comparison can be justified since the former material is normally proposed as a mosaic crystal to diffract photons at those energies, the latter, having an atomic number comparable to that of Cu and being commercially available as high perfection mono-crystals. The choice of a single ring was taken for a more direct comparison between the two configurations.

To fairly compare QM and mosaic crystals with the shape of square tiles, the energy passband and flux of incident photons were chosen to be the same for the two cases. For direct comparison with no need for normalization, the crystals were chosen to have the same tile size $L_{QM} = L_M = L = 1.00$ cm. Thus, the optimal mosaicity for the mosaic case, Ω_M, at 250 keV and $L = 1.00$ cm turned out to be 81 arcsec. Therefore, these parameters determine an energy passband $\Delta E = 8.3$ keV. Finally, a crystal thickness of $T_0 = 6.5$ mm was chosen in order to optimize the reflectivity r_M (Eq.1.2) throughout the whole ring of the lens.

For the QM case, the primary radius of curvature of the crystal must be twice the focal length of the lens, namely 40 m [57]. T_0 was a free parameter that determines both focusing capability and reflectivity of the lens. Indeed, large values of T_0 lead to higher reflectivity and lower spatial resolution on the focal plane, while smaller values of T_0 smoothly decrease reflectivity but significantly increase the focusing capability. An optimum value of T_0 is determined by perfect matching of the focal spot with the detector size. In this simulation, it was chosen $T_0 = 2.4$ mm.

Main features used for the simulation and its outcomes are reported in Tab. 4.1 and results are shown Fig. 4.3 for $E = 250$ keV. Here a cross-section of the photon
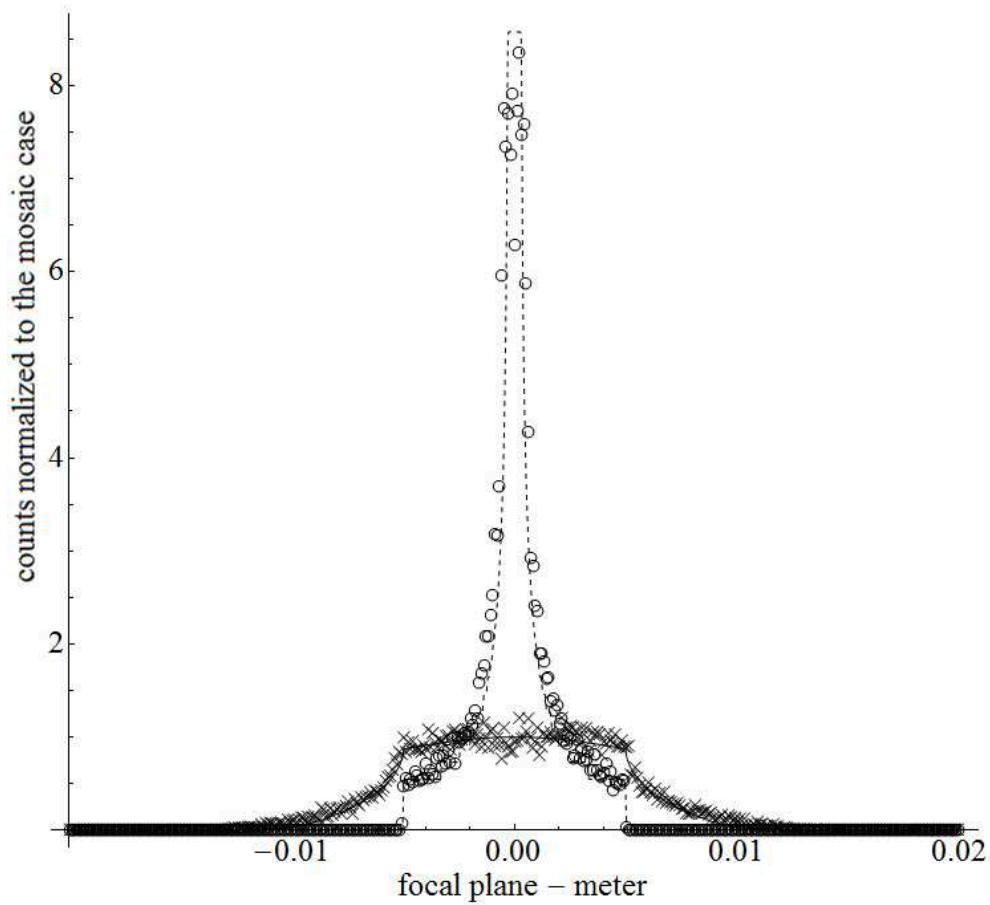
Figure 4.3: Cross-section of photon distribution in the focal plane for the cases of mosaic and quasi-mosaic crystals at $E = 250$ keV. For the mosaic case the crosses and the continuum line represent Monte Carlo simulation and analytical modelling, respectively. For quasi-mosaic crystal the circles and the dashed line represent Monte Carlo simulation and analytical modelling, respectively. Total counts are normalized to mosaic case. FWHM turns out to be 5.8 mm for mosaic case while 0.47 mm for quasi-mosaic one.

distribution in the focal plane, in the cases of mosaic and QM crystals is displayed. As visible, under same conditions of lens geometry, ΔE and flux of photons hitting the crystals, the focal spot for the QM case is significantly smaller and a higher signal intensity can be attained. This latter fact means that focusing with higher resolution can be accomplished if the lens is formed by QM crystals.

To compare the two focal spots, it was resorted to the signal-to-noise ratio as follows

$$StN = \frac{S}{N} \propto \frac{S}{V_{det}} \propto \frac{S}{r_{focus}^2} \qquad (4.9)$$

where S is the signal count within a specified encircled area with radius r_{focus}, N is the background, V_{det} is the useful volume of the detector and r_{focus} is half of the FWHM of photon distribution in the focal plane. The background was taken proportional to the volume of detector, this latter facing the incoming X-rays with a surface as large as the encircled area. Due to different focalization properties, the obtained FWHMs of photon distribution in the focal plane for QM and mosaic cases were significantly different.

As a result of simulation, the quotient between the signal-to-noise ratios for the cases of QM and mosaic crystals turned out to be

$$\frac{StN_{QM}}{StN_M} \approx 10 \tag{4.10}$$

all over the energy range 100-250 keV.

4.4   Conclusions

The effect of quasi-mosaicity in Ge crystals shows efficient focusing of high-energy photons in a Laue lens. The size of the focal spot yielded by a Laue lens made of QM crystals is significantly smaller than that obtained with mosaic crystals under same experimental conditions. Thereby, the focusing capability of a Laue lens can be largely improved through QM crystals.

Since with QM crystals it is not simple to obtain large values of curvature of the diffracting planes, a model was proposed in [58] to calculate the diffraction efficiency of X-rays in Laue geometry for curved crystals with an arbitrary value of the curvature radius. The model generalizes the results based on the dynamical theory of diffraction, which are valid only for crystals with a radius of curvature lower than the critical curvature. The model was proposed for any kind of crystal, and its efficiency tends to one-half in the limit of a thick flat crystal.

Starting from the obtained results, an extensive study about the quasi-mosaic effect was performed. Several Si and Ge samples were produced at SSL and their diffraction capability were analyzed at ILL and ESRF. The experimental results are shown and discussed in the next chapters. The performed study aims to realize a Laue lens based on QM crystals, capable of concentrating the diffracted photons in a focal spot in such a way to maximize the sensitivity of the lens.

CHAPTER 5

Experimental verification of quasi-mosaicity in self-standing Si and Ge grooved crystals

5.1 Quasi-mosaicity in grooved crystals

A silicon and a germanium quasi-mosaic bent crystal for high-resolution diffraction of X- and γ rays were realized. Production and optical characterization of a Si and a Ge sample was carried out at SSL. Commercially available pure wafers were diced to form two plates using the DISCO^{TM} DAD3220, equipped with rotating diamond blades of 150 μm width and 5 μm diamond grain size (G1A 320). A net bending was imprinted to the crystals thanks to a series of superficial grooves to keep the curvature without external devices. Then, the curvatures were measured using the optical profilometer VEECO^{TM} NT1100.

5.2 Quasi-mosaicity in the Si sample

Crystallographic orientations of the Si sample are indicated in Fig. 5.1, and the profilometry characterization is reported in Fig. 5.2. Main features are reported in Tab. 5.1.

The Si sample was tested through γ-ray diffraction at the Institut Laue-Langevin (ILL) (Grenoble, France) at the facility named DIffractometer for Gamma Ray Astrophysics (DIGRA), a facility purposely built for characterization of instrumentation in Astrophysics. The γ-ray beam energy was 181.931 keV and monochromaticity

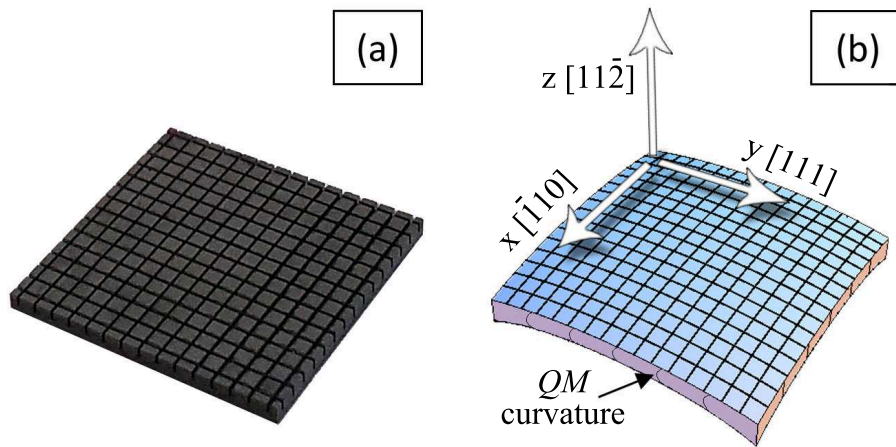Figure 5.1: a) Photo of the sample. It is possible to see the grid of grooves. b) Schematic representation of the sample. The crystallographic orientation and the QM curvature are highlighted.
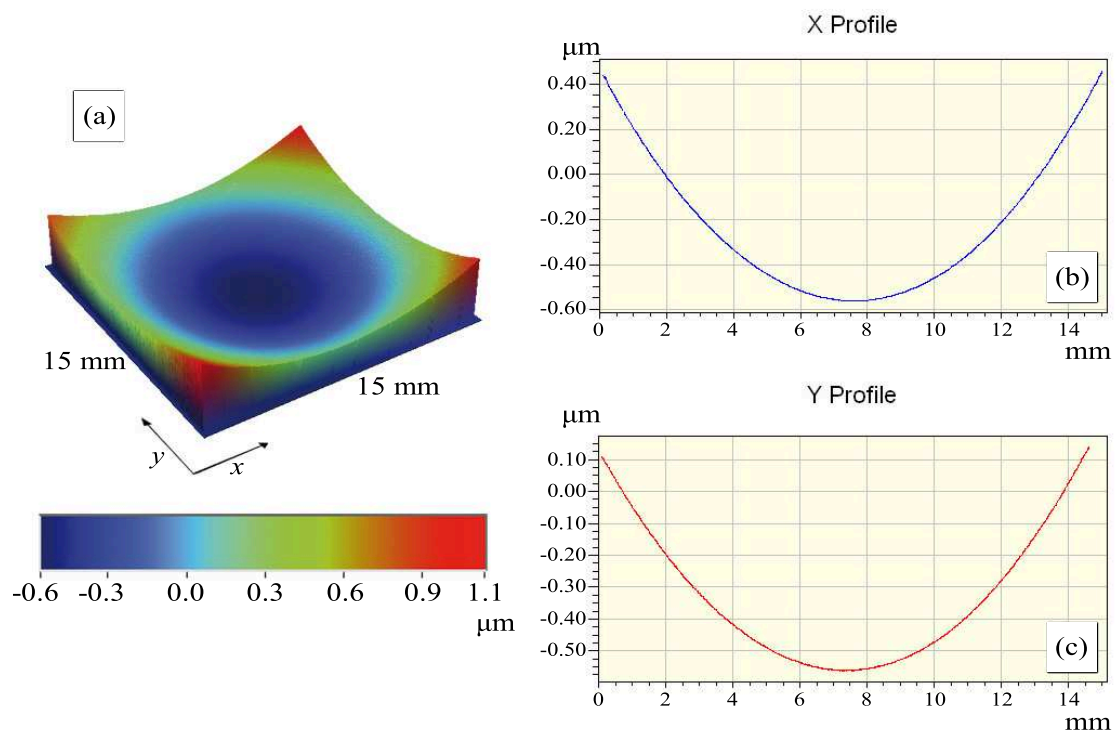

Figure 5.2: a) Interferometric measurement of backside of the Si sample. Left side: 3d view analysis (a). Right side: Cross sections of the deformation pattern along x (b) and y directions (c), as taken on the center of the sample

Table 5.1: Crystal features

Material	Silicon
Tile size (mm^2)	15×15
Tile thickness (mm)	1
Blade type	G1A 320
Blade rotation (rpm)	40000
Blade speed (mm/s)	0.2
Groove depth (μm)	500
Number of grooves	15×15
Groove step (mm)	1
Primary radius of curvature along y (m)	38
QM radius of curvature (m)	99

$\Delta E/E \approx 10^{-6}$. The γ-ray flux was produced by neutron capture in a gadolinium target ($^{157}_{64}$Gd) inserted close to the nuclear reactor of ILL at a temperature of about 400°C. Beam divergence after the Si (220) monochromator was 1 arcsec, as measured by recording a rocking curve (RC) of the monochromator itself. Collimated-beam size dimension was 1 mm on the diffraction plane (yz) and 3 mm on the plane (xz), z being the direction of the beam. A standard electrode coaxial Ge detector with 25% relative efficiency was used.

Characterization of the sample was carried out by performing RCs. The photon beam hit the $(11\bar{2})$ surface of the sample and was diffracted by bent (111) planes. Diffraction efficiency was recorded on the center of the sample and the experimental RC is reported in Fig. 5.3.

The gray zone represents the theoretical expectation as calculated through a custom-made code specifically designed to predict the behavior of bent and mosaic crystals. Both primary and secondary curvatures were accounted for in the simulation. From Eq. 4.5, the secondary-to-primary ratio holds $\frac{R_{QM}}{R_P} \simeq 2.614$ for the orientation used. In fact, the beam was diffracted by (111) bent planes, whose angular distribution consisted of the convolution between the portion of primary curvature, as seen by the beam, and the secondary curvature. The primary curvature seen by the beam was calculated taking into account the width of the collimated beam (1 mm) and the primary radius of curvature measured with the profilometer. The divergence of the beam was also included, by convolving the obtained distribution with a gaussian of $\sigma = 1$ arcsec. Finally, a morphological factor was included to consider the part of the sample that cannot diffract, i.e., the portion of material removed during the grooving process.
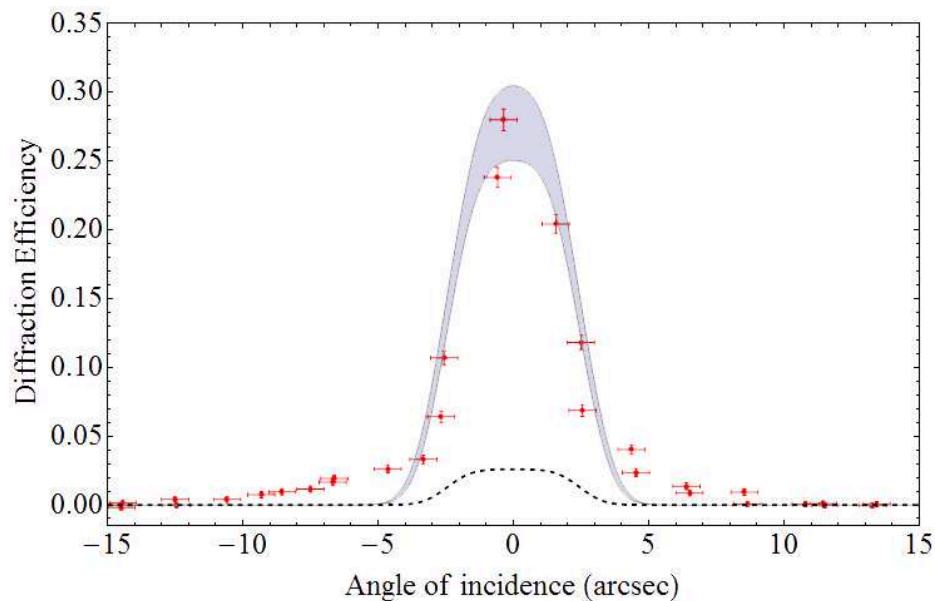
Figure 5.3: Experimental and theoretical RCs. Red circles plot the intensity of measured diffracted beam with their uncertainty bar. The gray area represents the expected result as calculated by taking into account the experimental uncertainties. The dashed black line represents diffraction efficiency if QM curvature were absent.

Fig. 5.3 shows a good agreement between theoretical expectation relying on quasi-mosaicity and experimental results, and was indeed the first experimental demonstration that self-standing QM crystals can be manufactured via superficial grooving.

The key effect of quasi-mosaicity, owing to the curvature of diffracting planes, is a raise in diffraction efficiency. For comparison, it was simulated the same crystal with the same primary curvature and orientation if there were no quasi-mosaicity, i.e., if the diffracting crystalline planes were flat. In this case, the contribution in the convolution from the secondary curvature would be a Darwin-broadened distribution instead of a wider uniform distribution due to quasi-mosaiciy. Moreover, in the case of flat diffracting planes, the diffraction efficiency was set at 0.5 because of intrinsic limitation of diffraction by flat planes in thick crystals [24]. Diffraction efficiency resulted in the dashed line in Fig. 5.3, which is by far lower than for the case of curved diffracting QM planes.

5.3   Quasi-mosaicity in the Ge sample

Crystallographic orientations of the Ge sample are indicated in Fig. 5.4, and the profilometry characterization is reported in Fig. 5.5. Main features are reported in
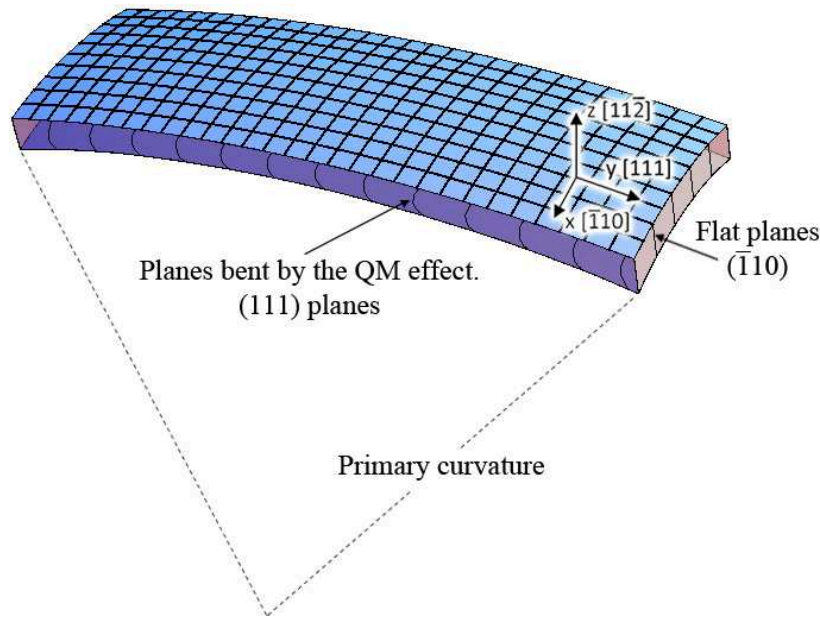
Figure 5.4: Sketch of the Ge sample. Crystallographic orientations and grooves are highlighted, with the coordinate system used.

Tab. 5.2.

The Ge sample was analysed by diffraction of the (111) planes, bent as a result of the quasi-mosaic effect. Thus, curvature obtained through the grooving method (primary) induced a secondary curvature of (111) planes through the quasi-mosaic effect, as shown in Fig. 5.4. In this case, the QM radius of curvature is 2.39 times the primary one, viz. $R_{QM} = 2.39 R_p = 92.9$ m.

5.3.1   High-efficiency diffraction

Diffraction efficiency of the sample was tested through X-ray diffraction at beamline ID15A of ESRF. A highly monochromatic beam was set at 150 or 300 keV. The characterization of the samples was carried out by performing rocking curves (RCs). The beam size was 50×50 μm^2 wide, impinging on a region of the sample free of the grooves. Rocking curves are shown in Fig. 5.6 a and b.

The FWHM of the RCs turns out to be a direct measurement of the angular distribution of the (111) diffracting planes. Since the sample was 2 mm thick, the FWHM of the angular spread was expected to be 4.4 arcsec. This value was well verified through analysis of broadening of the RCs at both beam energies.

The reflectivity was about 50% for both cases, though the expected values were 100% at 150 keV and 95% at 300 keV. It was an effect similar to that in Fig. 3.7,
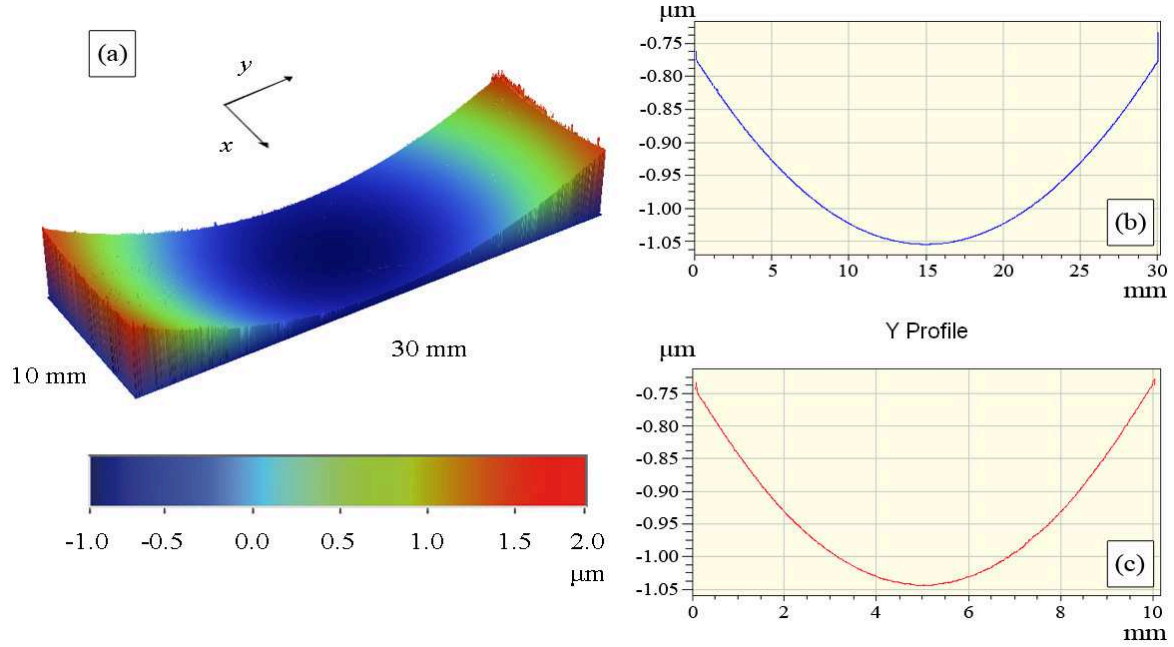
Figure 5.5: a) Interferometric measurement of backside of the Ge sample. Left side: 3d view analysis (a). Right side: Cross sections of the deformation pattern along x (b) and y directions (c), as taken on the center of the sample

Table 5.2: Crystal features

Material	Germanium
Tile size (mm^3)	10×30×2
Blade type	G1A 320
Blade width (μm)	250
Blade rotation (rpm)	3000
Blade speed (mm/s)	0.1
Diamond grain size μm	5
Groove depth (μm)	1550 ± 5
Number of grooves	9×28
Groove step (mm)	1
Primary radius of curvature R_p along y axis (m)	38.86 ± 1.94
QM radius of curvature R_{QM} (m)	92.9 ± 4.6
QM angular spread Ω_{QM} (arcsec)	4.4 ± 0.2
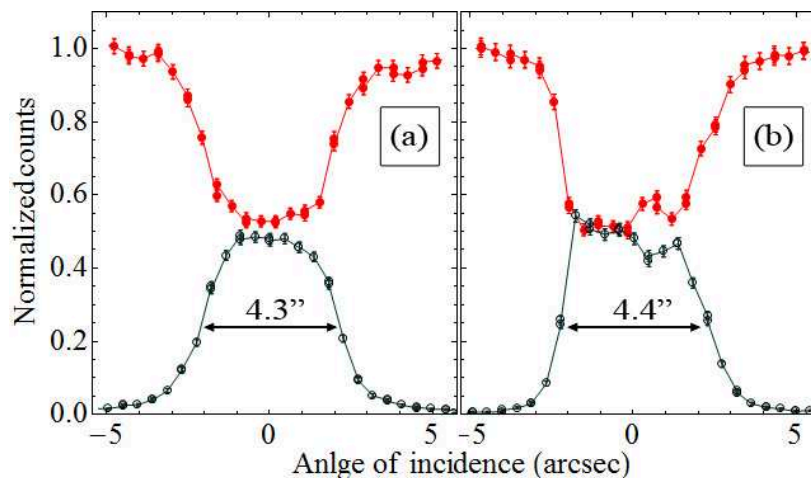
Figure 5.6: RCs of crystal. The filled red circles plot the intensity of the transmitted beam, whereas the empty blue circles plot the intensity of the diffracted beam. (a) Beam energy at 150 keV. (b) Beam energy at 300 keV.

namely diffraction efficiency was pinned at 50% if the diffraction occurred in a layer of material rich in defects and cracks. This effect was interpreted as a sort of partial mosaicization of the sample due to the grooving process. From a microstructural point of view, the material close to the grooves is subjected to contact with numerous particles of the blade at the same moment, which cause different contact pressures and produce different depth of cut due to their different shape and size. Thus, metallization, plastic deformation and brittle fracture may occur simultaneously [46]. The scarce knowledge of the distribution of dislocations, defects and cracks in the structure due to the grooving process makes it unfeasible any attempt to predict analytically the diffraction efficiency. However, recorded values of diffraction efficiency are quite satisfactory, being higher than any other performance relying on mosaic crystals.

5.3.2   Focusing of an X-ray beam

In order to highlight the focusing effect driven by the sample curvature, the crystal was analyzed through a diverging and polychromatic X-ray source at ILL [59, 60]. The diffractometer used a high-voltage and fine-focus X-rays tube designed for industrial radiography, the X-ray energy range being between 80 and 420 keV. The beam impinged onto the sample with an angle depending on the position at the entry face of the crystal. Thus, X-rays with different energies were diffracted towards the image point, which depended on the curvature of the crystal. A sketch of experimental configuration is shown in Figs. 5.7a and 5.7b.
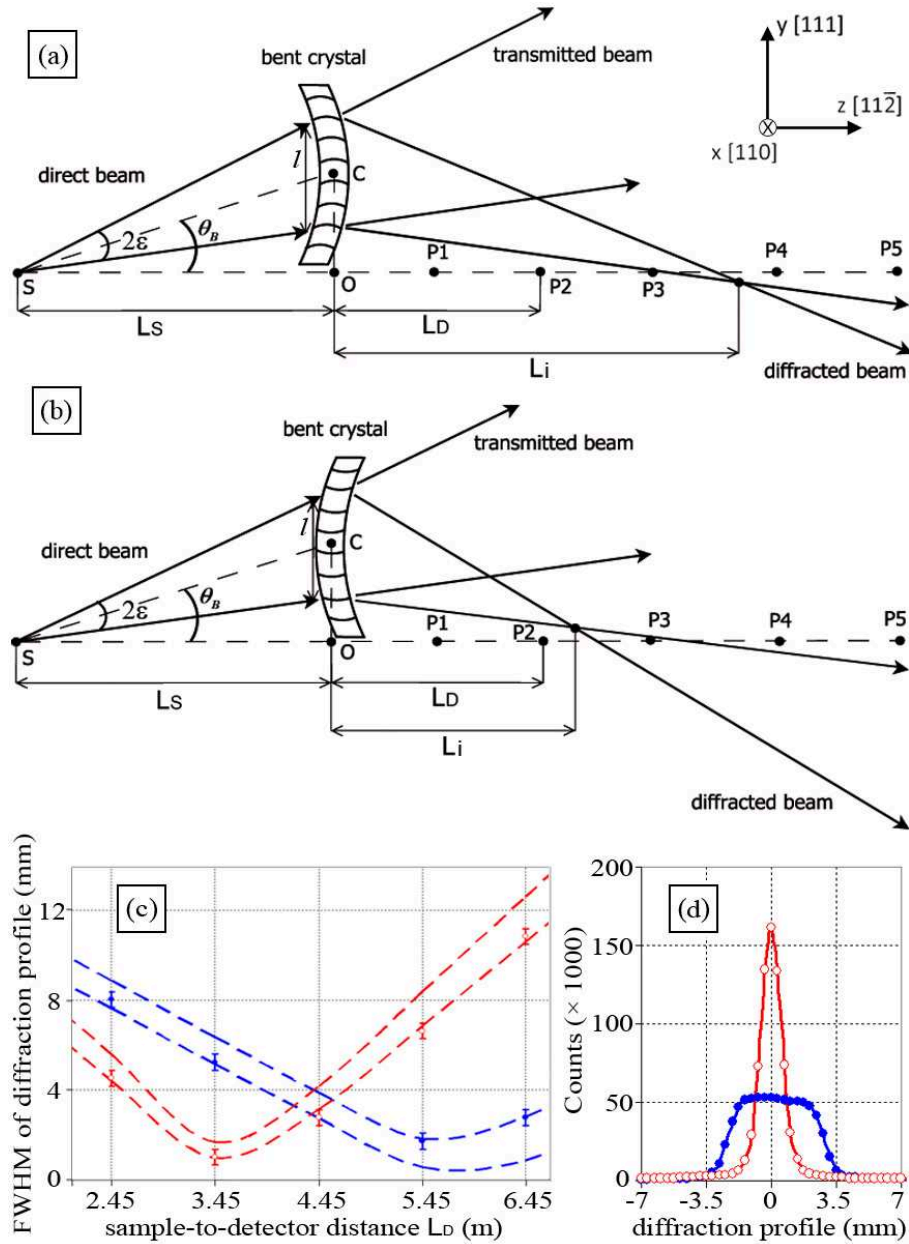
Figure 5.7: Schematic representation of the experiment with a divergent polychromatic X-ray beam and the bent crystal with the QM curvature in Laue symmetric geometry. Depending on the sign of R_P, the image distance increase (a) or decrease (b). (c) FWHM of diffraction profile plotted as a function of sample-to-detector distance L_D. Blue filled circles plot the measured width related to (a) and red empty circles plot the measured width related to (b). Dashed lines enclose the range of the theoretical width calculated using Eq. 5.2 and considering the uncertainty over parameters. (d) Diffraction profile with detector in position P2 ($L_D = 3.45$ m). Blue filled circles refer to (a), red empty circles refer to (b).

Table 5.3: System parameters an their uncertainty

Parameter	Mean value	Uncertainty
source-to-sample distance L_S (m)	4.45	0.04
sample-to-detector distance L_D (m)	variable	0.02
source-to-collimator distance (m)	3.03	0.03
collimator-to-sample distance (m)	1.42	0.01
collimator width (mm^2)	9.5×9.5	0.1
$\overline{CO}$ (mm)	45	1
Portion of crystal hit by the beam l (mm)	14.5	0.6
Source diameter a (mm)	1.0	0.1
Mean Bragg angle θ_B (degree)	0.58	negligible
Beam divergence ε (degree)	0.100	0.004

Table 5.4: The detector: high-resolution and sensitive X-ray image intensifier coupled with a CCD camera

Detector features	
number of pixels	512×512
size of each pixel (mm^2)	0.35×0.35
acquisition time	few seconds

The geometrical parameters are reported in Tab. 5.3, whereas the detector is described in Tab. 5.4. Diffraction of (111) planes was firstly analysed with the beam impinging on the crystal surface as in Fig. 5.7a. Then, the crystal was rotated by 180° around the x axis (see Fig. 5.7b). Considering the geometrical configuration, the energy range of diffracted beam turned out to be 160-227 keV.

Is worthwhile to notice that in spite that the sample is spherically bent, the crystal behaves as a cylindrical lens because the focusing effect only occurs in the scattering plane. Thus, diffraction of a polychromatic and divergent beam produces a line on the detector [61]. The FWHM of the intensity profile, taken on a cross section perpendicular to the line, depends on several parameters. In the case of a perfect crystal and the sample-to-detector distance L_D equal to source-to-sample distance L_S, the width size depended only on the X-ray source size and on the crystal thickness traversed by the beam. Conversely, a curved crystal can concentrate the diffracted X-rays either at a smaller or a larger distance. Indeed, under the small-angle approximation, it is possible to prove

$$\frac{1}{L_i} = \frac{1}{L_S} + \frac{2}{R_P} \tag{5.1}$$

where L_i is the image distance of a bent crystal with primary radius of curvature

equal to R_p with the following convention: $R_P > 0$ when the centre of the osculating circle is in the half-plane where the image lies, while $R_P < 0$ in the contrary case.

To evaluate the focusing capability of the sample, the FWHM of the diffracting profile was recorded on the detector, that is

$$FWHM = \sqrt{a^2 + \left(2T_0\theta_B - 2L_D\frac{T_0}{R_{QM}} + l\left|1 - \frac{L_D}{L_i}\right)\right|\right)^2} \qquad (5.2)$$

where a is the source diameter, T_0 the sample thickness traversed by the beam, l the size of the beam on the crystal surface and R_{QM} the radius of curvature of the QM diffracting planes. Also in this case is $R_{QM} > 0$ when the centre of the osculating circle is in the half-plane where the image lies, else is $R_{QM} < 0$. The term $2L_D\frac{T_0}{R_{QM}}$ represents the contribution of the QM planes, that can change the FWHM of the spot but not L_i. If $L_D = L_S$ it is possible to obtain the formula described in [53, 54]

The image distance was $L_i = 5.77$ m for Fig. 5.7a and $L_i = 3.62$ m for Fig. 5.7b. In order to verify the effect of the crystal curvature, the detector was positioned at 5 different points indicated with $P1$, $P2$, $P3$, $P4$, $P5$ in Figs. 5.7a and 5.7b, while L_S was kept fixed. L_D was increased by steps of 1.00 m, starting from 2.45 m for $P1$ to 6.45 m for $P5$. In Fig. 5.7c the width of the measured diffraction profiles were plotted as a function of L_D, in agreement with their theoretical expectations. Finally, Fig. 5.7d shows the measured diffraction profiles with $L_D = 3.45$ m ($P2$).

5.4   Conclusion

It was demonstrated that it is possible to exploit quasi-mosaic self-standing curved crystals to diffract hard X- and γ rays. Sample fabrication relied on the grooving method, which is an easy and cheap technique. It has been experimentally demonstrated that quasi-mosaicity significantly raises the crystals diffraction efficiency, which results at least one order of magnitude higher with respect to the one expected from crystals with flat diffracting planes. The aid of simulation leads to highlight the reasons for the enhancement, which is to be ascribed to the convolution of the response due to the primary curvature with a broad distribution owing to the secondary QM curvature. However, it seems that the grooving process lower the capability of a bent QM crystal.

As well as in a Laue lens, a crystal that exploits the QM effect could also be used in a white-light diffractometer to control the focal length of the diffracted X-ray beam by simply adjusting the primary curvature, while the QM curvature guaranties a high

integrated diffraction efficiency. Such an operation could easily be automated through a piezo-driven holder.

On the basis of the obtained results, quasi-mosaicity was exploited as effect to produce a series of high-resolution optical elements for the realization of a prototype of Laue lens within the Laue project, as shown in chapter 6. Moreover, quasi-mosaicity was investigated along unusual crystallographic directions, as shown in chapter 7. Following from that, two new schemes of Laue lens are proposed in chapter 8.

CHAPTER 6

Manufacture of self-standing Ge QM crystals for the Laue project

6.1 Quasi-mosaic crystals for a prototype of Laue-lens

The realization of a Laue lens for astronomical purposes does demand mass production of crystalline tiles as optical components. It has been demonstrated in previous chapters that self-standing curved crystals are a reliable tool to diffract X-rays with high-efficiency. Moreover, by exploiting the quasi-mosaic effect, it is possible to diffract X and γ radiation with high resolution. Here the fabrication of 150 quasi-mosaic Ge samples, bent by grooving one of their largest surfaces, is presented. It is also shown that the grooving method is a viable technique to manufacture such crystals in a simple and very reproducible way, thus compatible with mass production. Fabricated samples highlight very homogenous curvature. Furthermore, with a specific chemical etch, it is possible to finely adjust one by one the radius of curvature of each grooved sample.

Grooved QM Ge samples were fabricated for the Laue project (2010-2013) under support of the Italian Space Agency (ASI). The Laue project is devoted to the development of advanced technologies for building a petal of a Laue lens with a broad energy passband (100-300 keV) and long focal length (20 m) for space-borne Astrophysics experiments [62, 63]. The main aim is to significantly overcome the sensitivity limits of the current generation of X-ray telescopes and improve the imaging capability.
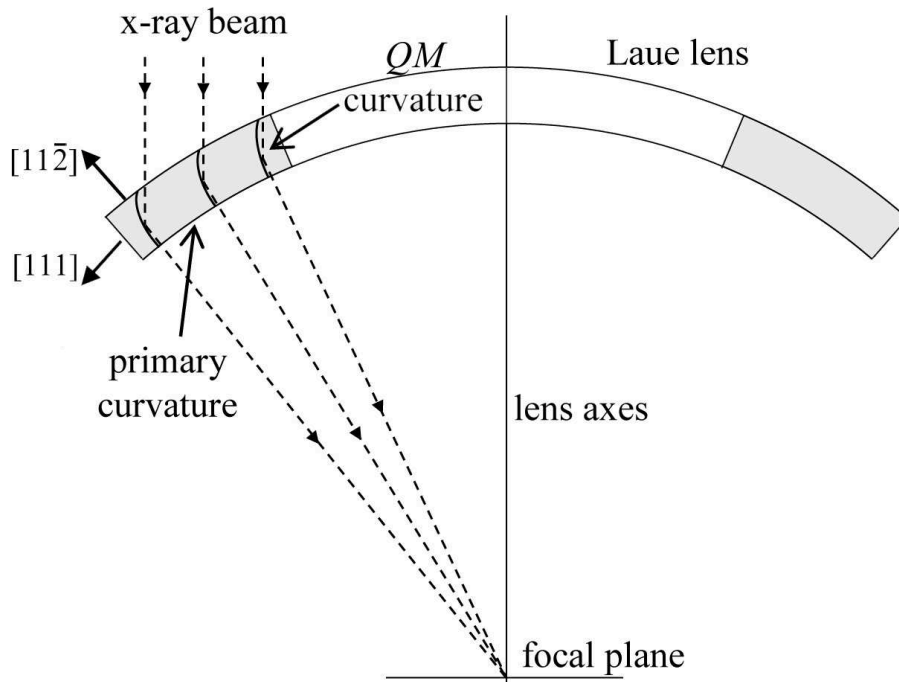
Figure 6.1: Schematic representation of a cross section of a Laue lens based on QM crystals. Primary curvature of $(11\bar{2})$ planes leads to a secondary curvature of (111) planes owing to quasi-mosaicity. In this configuration the (111) diffracting planes are perpendicular to the main surface of the plate. It can also be seen the capability of primary curvature to focalize diffracted radiation while QM curvature establishes an increase in diffraction efficiency.

6.2 Experimental realization of the Ge QM samples

To combine the focusing action of the primary curvature with the raise in the diffraction efficiency due to the QM curvature, the crystals have to be positioned in the Laue lens as depicted in Fig. 6.1. In fact, to focalize the impinging photons, a cylindrical curvature would work. However, it derives from the theory of elasticity that a spherical curvature is required to obtain the QM effect [13].

The production and optical characterization of 150 QM Ge crystals for the Laue project was carried out at SSL. Crystallographic orientations are indicated in Fig. 6.2. Commercially available pure Ge wafers were diced to form $30 \times 10 \times 2$ mm^3 plates, using the DISCO^{TM} DAD3220, equipped with rotating diamond blades of 250 μm width and 5 μm diamond grain size (G1A 320). A permanent curvature was induced through the grooving method. A radius of curvature of 40 m was chosen for the

Table 6.1: Crystal features

Material	Germanium
Tile size (mm^3)	30×10×2
Blade type	G1A 320
Blade width (μm)	250
Blade rotation (rpm)	3000
Blade speed (mm/s)	0.1
Groove depth (μm)	1550
Number of grooves	9×28
Groove step (mm)	1
Primary radius of curvature along y (m)	40
QM radius of curvature (m)	95.6
Angular bandpass (arcsec)	4.3

project. It is possible to calculate the ratio between QM (R_{QM}) and primary (R_P) radius of curvature thanks to the linear theory of elasticity. It turns out to be $\frac{R_{QM}}{R_P} =$ 2.39, which corresponds to a QM curvature of about 95.6 m. The angular bandpass corresponding to this radius of curvature is 4.3 arcseconds. Main features are reported in Tab. 6.1. The curvature of all the samples was measured using the profilometer VEECO^{TM} NT1100 on the back surface of each sample.
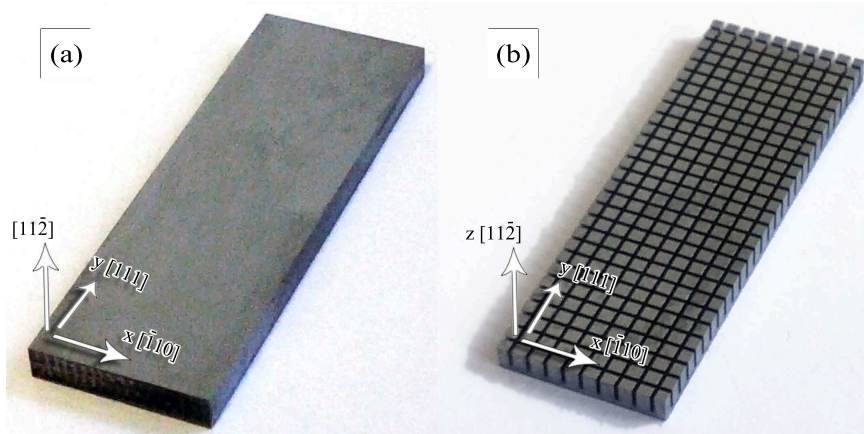

Figure 6.2: Photo of a Ge sample before (a) and after (b) the manufacture. Crystallographic orientation are highlighted.

The profilometric measurement of the primary radius of curvature of a typical sample is reported in Fig. 6.3. The curvatures resulting from the grooving process are very close to a spherical surface, because the grooves are regularly spaced and have all the same depth.
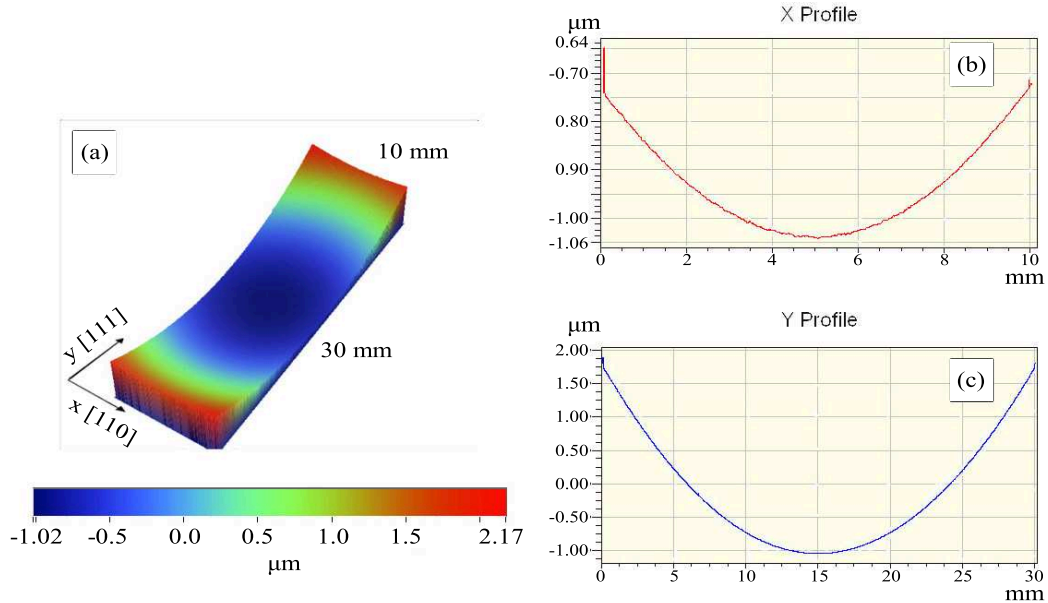
Figure 6.3: Interferometric measurement of backside of a sample with average radius of curvature $r = 39.9$ meters. Left side: 3d view analysis (a). Right side: Cross sections of the deformation pattern along x (b) and y directions (c), as taken on the center of the sample.

To verify the uniformity of the curvature, subtraction of measured surface with a perfectly spherical surface having the radius of curvature equal with the average radius of curvature of the measured sample was performed. Result of subtraction with the sample of Fig. 6.3 is shown in Fig. 6.4. Moreover, the root mean square roughness R_q was calculated by using Eq. 6.1. It represents the standard deviation of the distance between the measured sample surface and the spherical surface with radius of curvature $= 39.9$m.

$$R_q = \sqrt{\frac{1}{MN} \sum_{i=l}^{M} \sum_{i=l}^{N} Z^2(x_i, y_i)} = 13.86nm \qquad (6.1)$$

where M and N are the numbers of data points in the X and Y direction of the array, respectively, and Z is the surface height.

Although the distribution of primary radius of curvature of the manufactured samples was not symmetric, a fit with a Gaussian distribution was worked out. The distribution for the [111] direction is displayed in reported in Fig. 6.5. The series of 150 samples was purposely produced with an average radius of curvature slightly lower with respect to the desired value of 40 meters. Such distribution averaged 36.6
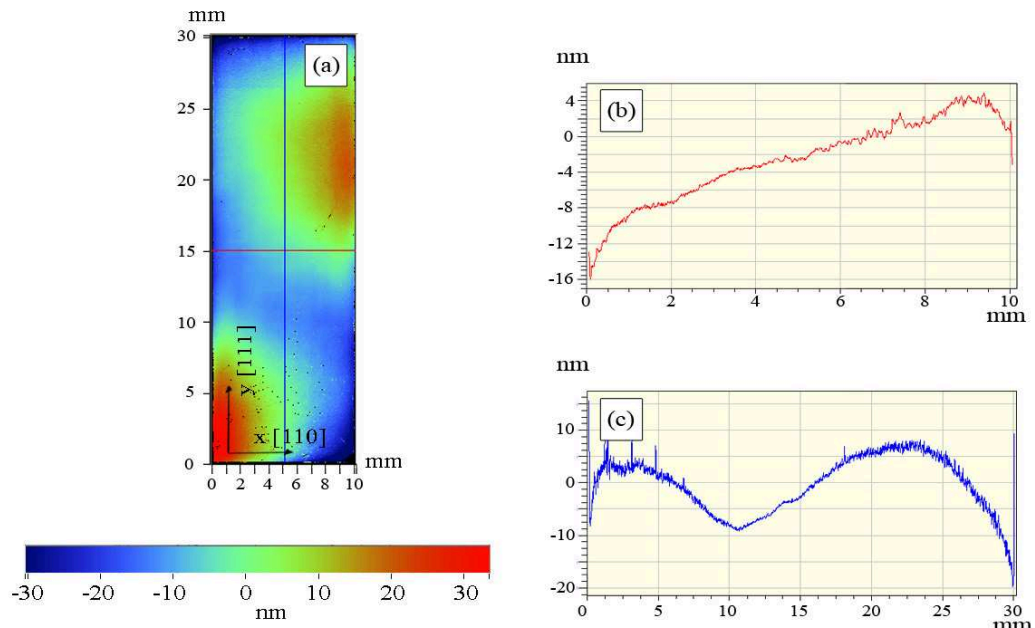
Figure 6.4: Subtraction between the measured sample with a spherical surface with radius $r = 39.9$ meters. Left side: 2d view of subtracted data (a). Right side: Cross sections of the subtraction pattern along x (b) and y directions (c), as taken on the center.

m with standard deviation of 6.6 m. Indeed, the over-bent samples can be adjusted one by one at attain the value of 40 m thanks to a chemical etch. In fact, during the production, some features were difficult to control. For example, there was an uncertainty on the crystals thickness, which can vary from sample to sample. The consequence was partial reproducibility in the final curvature. Indeed, for each sample the curvature is homogeneous, but the resulting radius of curvature may vary from sample to sample.

The method to adjust the curvature consisted in a fast chemical etch, based on a solution of H_2O_2. Such solution is capable of oxidizing Ge with different speeds, depending on the crystalline phase [64]. In fact, it is possible to selectively remove the most amorphous part of a sample, namely the material plasticized by the blade, by lowering the superficial tension and then the curvature of the sample. With quick chemical etch at low H_2O_2 concentration, the possibility of increasing the radius of curvature of samples of a few meters was experimentally verified. In Tab. 6.2 an example is reported. 60 seconds of etching was performed, obtaining a relaxation of the curvature of about 4 meters, starting from 36.8 to 40.3. With shorter etch it would be possible to obtain lower value of relaxation.
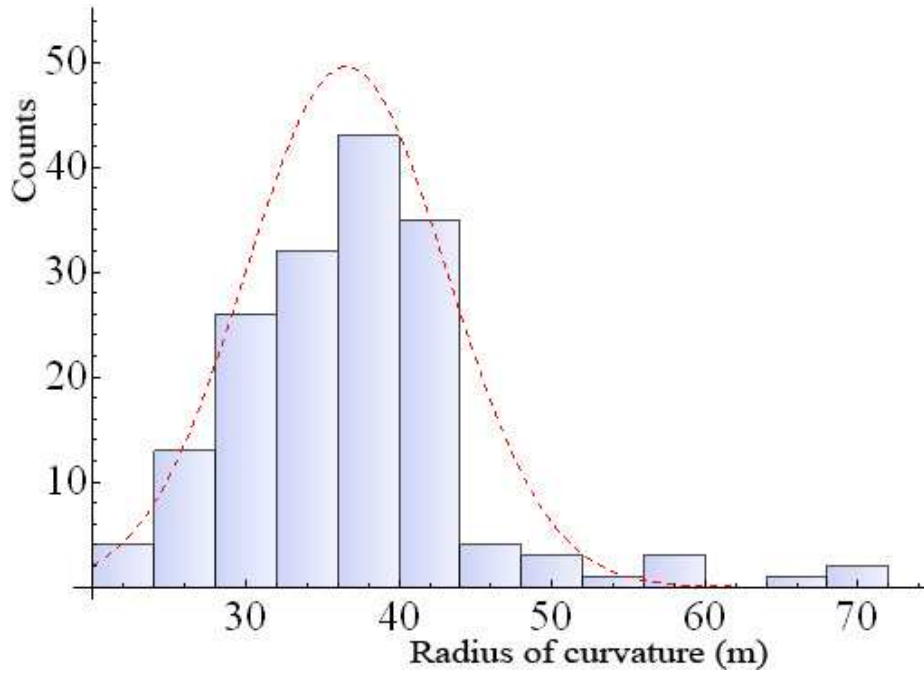
Figure 6.5: Distribution of primary radius of curvature, measured along [111] direction on the 150 crystal tiles produced, before the chemical etch. The red dashed line shows the best fit Gaussian distribution.

6.3 Discussion

Ideally, each tile is expected to produce a diffracted spot shaped as a thin rectangle, with 10 mm width and of thickness given by the quasi-mosaic defocusing. The defocusing can be estimated to be $2F_{det}m$, F_{det} being the distance of the tile from the focal spot and m the angular distribution due to QM effect [27]. In this case $2F_{det}m \simeq 0.84mm$.

The expected reflectivity for these crystals can be predicted by the diffraction theory for curved diffracting planes. However, a portion of the sample is removed during the manufacture process, thus it must be taken into account that the grooves occupy about 32.5% of the samples volume. Expected reflectivity as a function of the photon energy is reported in Fig. 6.6.

The production of 150 QM samples of germanium was carried out rapidly and in a very reproducible way. The interferometric measurement takes few minutes, less than 5 minutes for each sample. The chemical etch is very fast, it takes about one minute. The cut process is the longest part of the production, it is about 4-5 h long. Currently, it is necessary to measure the samples for each step, because the experimental condition may vary in a not well controlled way. More time can be

Table 6.2: Adjustment of the curvature in a Ge grooved sample

Chemical etch	solution of H_2O_2
Initial radius of curvature along [111]	36.8 m
Concentration	2.5 ml in 100 ml of water
Etch duration	60 s
Final radius of curvature	40.3 m
Temperature	room

saved, once all the processes will be optimized.
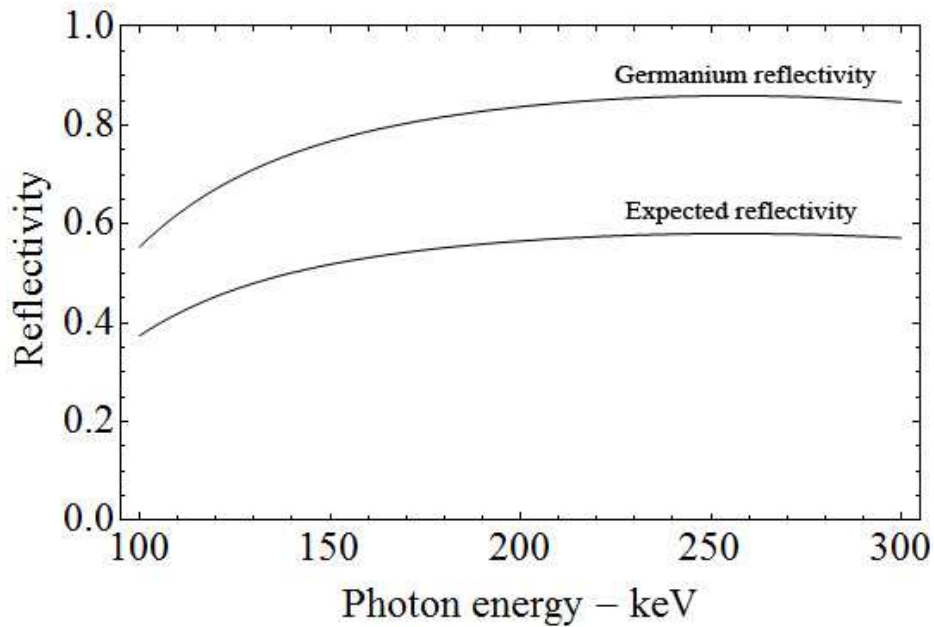
Figure 6.6: Expected reflectivity for the fabricated Ge samples. The top curve is the theoretical reflectivity of a non-grooved CDP block of germanium having dimensions identical to those of our tiles. The bottom curve shows the theoretical reflectivity of the grooved tiles, which takes into account the fact that a fraction of crystal is removed during the manufacture process.

It is shown that the samples obtained with the grooving method turn out to have a high-homogeneous curvature, with a small uncertainty on the final curvature. Moreover, with the chemical etch, it turns be possible to finely adjust one by one the radius of curvature of each sample, preserving the homogeneity of bending. Grooving turns out to be an elective method for a quick production of a large number of self-standing bent samples, that is a mandatory issue for a concrete realization of a Laue lens.

The Ge samples are currently being tested at LARIX facility, with X-ray diffraction on the QM (111) planes. When all these experimental data will be acquired, the prototype of the Laue lens will be assembled and tested at the LARIX laboratories to form the petal lens. Finally, it will be very important to verify if the curvature of the grooved crystals change once mounted on the lens support.

CHAPTER 7

Quasi-mosaic effect of (422) and (311) bent planes: experimental validation

7.1 Motivations

Crystals are the core of a Laue lens. For a concrete application of a Laue lens, crystals characterized by high-diffraction efficiency are needed, as well as high-resolution focusing of the diffracted photons. Moreover, it is very important that the lens is characterized by a large collecting area, resulting in a large effective area, in order to enhance the signal-to-noise ratio on the detector. The effective area of a Laue lens at a certain energy is defined as its geometric area, as seen by the X-ray beam, times the diffraction efficiency at that energy.

In order to increase the geometric area of a Laue lens and thus the number of collected photons, it is possible to use several materials with different lattice spacings and crystallographic orientations for diffraction. Unlike the case of mosaic crystals, for which the nominal direction of mosaic planes can be chosen relatively easily, the quasi-mosaic effect is bound up to very specific crystallographic orientations. It is the purpose of this chapter to show that quasi-mosaicity does exist in Si and Ge crystals along unusual and never explored orientations, such as the (422) and the (311). As it is explained in section 8.3, the combined use of Si and Ge exploiting (111), (422) and (311) QM CDPs leads to an unprecedented performance for a Laue lens. Indeed, exploiting (111), (422) and (311) diffracting planes would permit the fabrication of a Laue lens with the geometric area one order of magnitude larger than for a lens
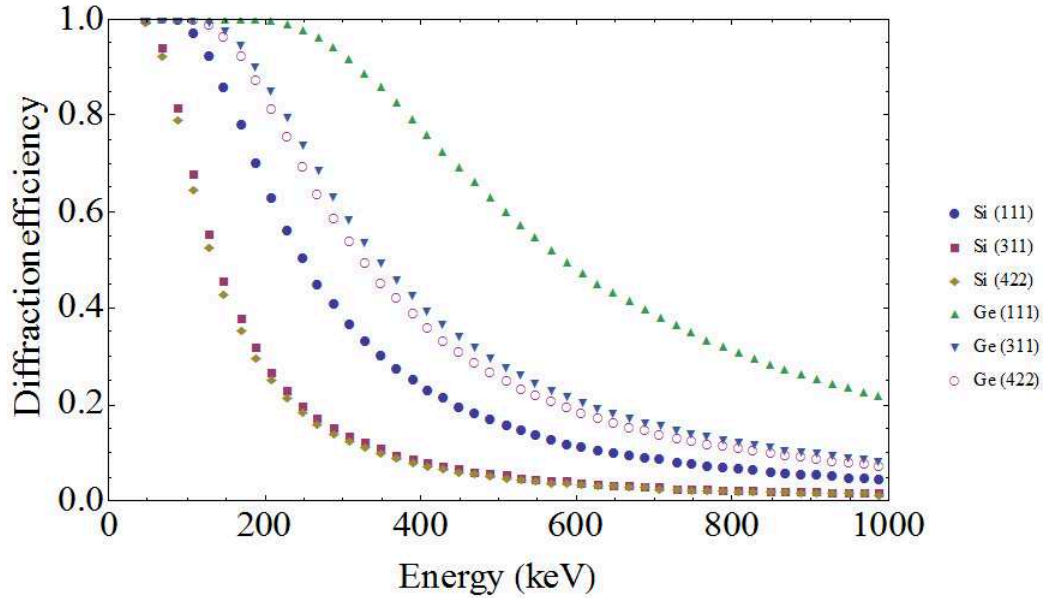
Figure 7.1: Theoretical diffraction efficiency for curved diffracting planes. The thickness traversed by the beam was set to be 2 mm, the angular spread of diffracting planes was 5 arc-seconds.

solely composed of (111) QM crystals. In fact, (111), (422) and (311) have different d-spacing, thus they occupy different positions in the Laue lens.

In Fig. 7.1 is shown the theoretical diffraction efficiency of Si and Ge crystals, by taking into account a QM angular spread of 5 arcsec, that is a typical value for QM crystals. It is possible to notice that the diffraction efficiency of high crystallographic indices is lower with respect to that for low indices. However, (422) and (311) crystals can be arranged in the outermost part of a lens because of the larger Bragg angle. Indeed, the distance R from the axis of the lens at which a crystal can diffract the radiation onto the detector is proportional to the Bragg angle, i.e., R depends on the crystallographic planes used for diffraction. Using the approximation for small angle, it results

$$R = f \tan(2\theta_B) \propto \sqrt{h^2 + k^2 + l^2} \tag{7.1}$$

where f is the focal length, θ_B the Bragg angle and (h, k, l) are the Miller indices of the planes used for diffraction.

Even if the diffraction efficiency for such crystallographic orientations is lower than that for the (111) planes, the external position guarantees a large geometric area, resulting in a large effective area. Moreover, since Ge and Si crystals have different d-spacing, even more locations for crystalline tiles are possible. In summary, building
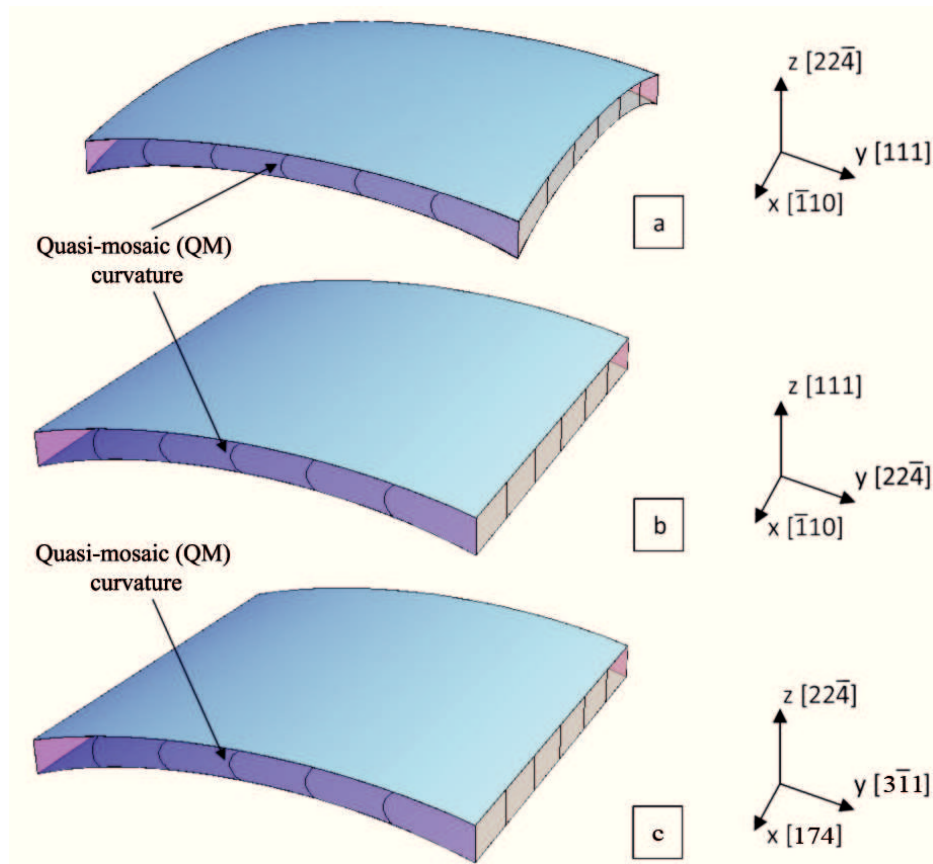
Figure 7.2: Schematic representation of a crystal plate with the coordinate system used for the modeling. In (a) two moments are applied, while in (b) and (c) a single moment is applied. Crystallographic orientation and QM curvature for the three cases are highlighted.

up a lens with very large geometric area that concentrates a range of energies with high efficiency can be envisaged.

7.2 QM curvature calculation for (422) and (311) planes

Since the QM curvature is a consequence of crystal anisotropy, its radius of curvature is strictly linked to the crystal orientation. It is possible to calculate the ratio between QM and primary curvatures thanks to the linear theory of elasticity.

Two new cases are considered. The case shown in Fig. 7.2a refers to quasi-mosaicity with (111) planes. It has been demonstrated in previous chapters that a primary spherical bending of (422) planes in Si or Ge plates results in a QM curvature

of the (111) planes. A spherical curvature can be obtained by applying two momenta M_x and M_y to a crystal. As shown in chapter 4, the ratio between QM and primary curvature radii is

$$\frac{R_{QM}}{R_{P_y}} = -\frac{S_{12} + S_{22}}{S_{41} + S_{42}}, \tag{7.2}$$

Since the stress is uniform over the largest surface, the ratio is independent of the crystal plate dimensions.

The case in Fig. 7.2b corresponds to the quasi-mosaicity in (422) planes[1]. For this case, it is demonstrated that cylindrical bending of (111) Si or Ge plates as a primary curvature results in a QM curvature of the (422) planes, so that only one momentum M has to be applied to the sample. For the case of Fig. 7.2c, it is demonstrated that cylindrical bending of (422) Si or Ge plates as a primary curvature results in a QM curvature of the (311) planes, so that also in this case only one momentum M has to be applied to the sample. In these two cases, the primary curvature along the y axis is

$$\frac{1}{R_{P_y}} = \frac{d^2w}{dy^2} = -\frac{M}{2I}S_{22}, \tag{7.3}$$

while the QM curvature in the focusing direction is

$$\frac{1}{R_{QM}} = \frac{d^2v}{dz^2} = \frac{M}{2I}S_{42}. \tag{7.4}$$

Finally, the ratio between QM and primary curvatures can be obtained as

$$\frac{R_{QM}}{R_{P_y}} = -\frac{S_{22}}{S_{42}}. \tag{7.5}$$

The ratios for the cases of interest are reported in Tab. 7.1.

7.3   Experiment with a (422) QM sample

Here the possibility to exploit the quasi-mosaic effect for bent (422) diffracting planes is experimentally demonstrated.

A cylindrical curvature was produced on a Si crystal by inducing a superficial strained layer. The tile size was $20 \times 100 \times 3$ mm^3 and the crystallographic orientation was the same as in Fig. 7.2b. The sample curvature was measured by using the optical

---

[1]Since diffraction by (211) planes is forbidden in diamond-like crystalline structure as Si and Ge, (422) planes were considered. However, they represent the same crystallographic direction.

Table 7.1: Ratios between QM curvatures and principal curvatures, the latter calculated along the y axis

QM CDP	R_{QM}/R_{P_y}
Ge (111)	-2.390
Si (111)	-2.614
Ge (422)	3.185
Si (422)	3.542
Ge (311)	3.141
Si (311)	3.455

Table 7.2: Experimental features

QM sample	
material	silicon
tile size	20×100 mm^2
tile thickness	3 mm
primary radius of curvature, along y [$22\overline{4}$]	21.2 m
QM radius of curvature, (422) planes	74.6 m
Beam Features	
γ-ray beam	
beam energy	181.931 keV
monochromaticity	$\Delta E/E \approx 10^{-6}$
beam divergency	1 arcsec

profilometer VEECO^{TM} NT1100 at SSL. The primary radius of curvature, measured along y, was 21.2 m. Using the results listed in Tab. 7.1, the radius of curvature of the (422) QM planes (secondary curvature) was 74.6 m.

Diffraction efficiency of the (422) CDP was tested by γ-ray diffraction in transmission geometry at the Digra facility at ILL. The γ-ray beam energy was $E = 181.931$ keV with monochromaticity $\Delta E/E \approx 10^{-6}$. Gamma quanta were produced by neutron capture in a gadolinium target ($^{157}_{64}$Gd), which was inserted close to the nuclear reactor of ILL at a temperature of 400°C. The beam divergence after the Si (220) monochromator was 1 arcsec, measured by recording a rocking curve (RC) of the monochromator itself. The collimated-beam size was 1 mm on the diffraction plane and 3 mm on the perpendicular plane. A standard electrode coaxial Ge detector with 25% relative efficiency supplied by Canberra was used. The main features of the experiment are reported in Tab. 7.2.

The sample was characterized by performing RCs. The photon beam hit the (111)
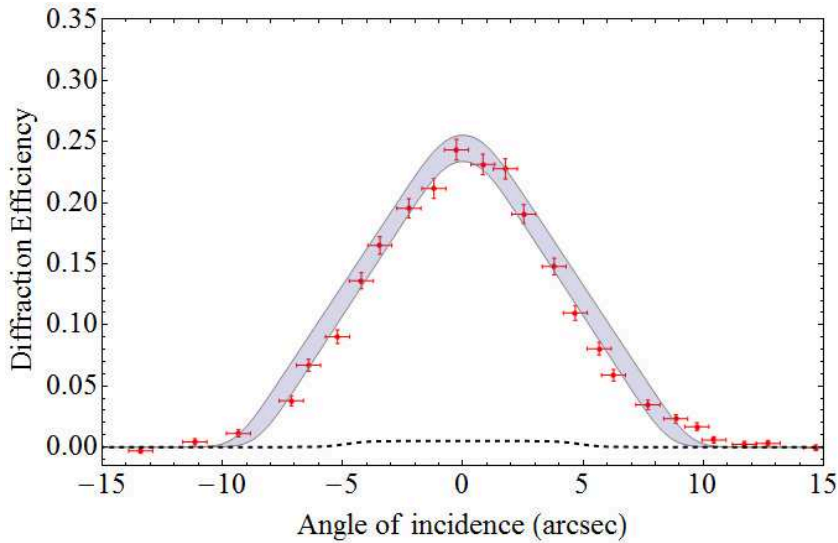
Figure 7.3: Experimental and theoretical RCs of a [22$\overline{4}$] QM crystal cylindrically bent. Red crosses plot the intensity of the measured diffracted beam with their uncertainty bar. The gray area represents the expected result as calculated by taking into account the experimental uncertainties. The dashed black line represents the diffraction efficiency without the *QM* curvature.

surface of the sample. Diffraction efficiency was measured at the center of the sample and its RC is reported in Fig. 7.3. The gray area in the figure represents the theoretical expectation as calculated through a custom-made code, specifically designed for simulating the performance of diffraction through broad-band crystals such as mosaic or CDP crystals. In the simulation, both primary and secondary curvatures were accounted for. The angular distribution after diffraction consists of the convolution between the distribution of the portion of primary curvature seen by the beam, and the distribution of secondary curvature. The primary curvature seen by the beam was calculated by taking into account the width of the collimated beam (1 mm) and the radius of curvature measured with the profilometer (21.2 m). To calculate the diffraction efficiency, the dynamical theory was considered [65]. Moreover, the divergence of the beam was included by convolving the obtained distribution with a Gaussian of $\sigma=1$ arcsec. Fig. 7.3 highlights the very good agreement between the theoretical expectation relying on quasi-mosaicity and the experimental results.

As a result of the above experiment, it can be inferred that the quasi-mosaicity of (422) planes can be implemented in the construction of a Laue lens composed of QM crystalline tiles.

Table 7.3: Crystal features

Material	Silicon
Sample size (mm^2)	15×15
Sample thickness (mm)	2
Blade width (μm)	250
Blade rotation (rpm)	3000
Blade speed (mm/s)	0.1
Groove depth (μm)	1550
Number of grooves along x axis	14
Groove step (mm)	1
Primary radius of curvature (R_p) along y axis (m)	25.0 $\pm$ 1.2
QM diffracting planes	(311)
R_{QM}/R_p	3.455
QM radius of curvature (m)	86.4 $\pm$ 4.3
QM angular spread Ω_{QM} (arcsec)	4.8 $\pm$ 0.2

7.4 Experiment with a (311) QM sample

Here it is experimentally demonstrated, as an innovative effect, the possibility to exploit the quasi-mosaic effect for bending (311) diffracting planes.

The production and the morphological characterization of a QM silicon sample was carried out at SSL. A commercially available pure Si wafer 2 mm thick was diced to form a plate of 15×15 mm^2 using the DISCO^{TM} DAD3220, equipped with a rotating diamond blade of 250 μm width and 5 μm diamond grain size (G1A 320). A permanent curvature was induced through the grooving method. The grooves were manufactured in such a way to obtain a cylindrical curvature of the sample, i.e., only along the x axis, as schematized in Fig. 7.2c.

The primary curvature was measured using the optical profilometer VEECO^{TM} NT1100 on the back face of the samples. The profilometric pattern of the sample surface is shown in Fig. 7.4 and the sample features are listed in Tab. 7.4.

The sample was tested through γ-ray diffraction at the DIGRA facility at ILL. The γ-ray beam energy was 181.931 keV. The beam features are summarized in Tab. 7.4.

Characterization of the sample was carried out by performing RCs. The diffraction efficiency was measured at the center of the samples and the pertaining RC are reported in Figs. 7.5a and b. Accordingly with the theory of diffraction, the RC is expected to be a uniform distribution about 35% high [65]. For a better understanding of the experimental results shown in Fig. 7.5, simulation of the RC was
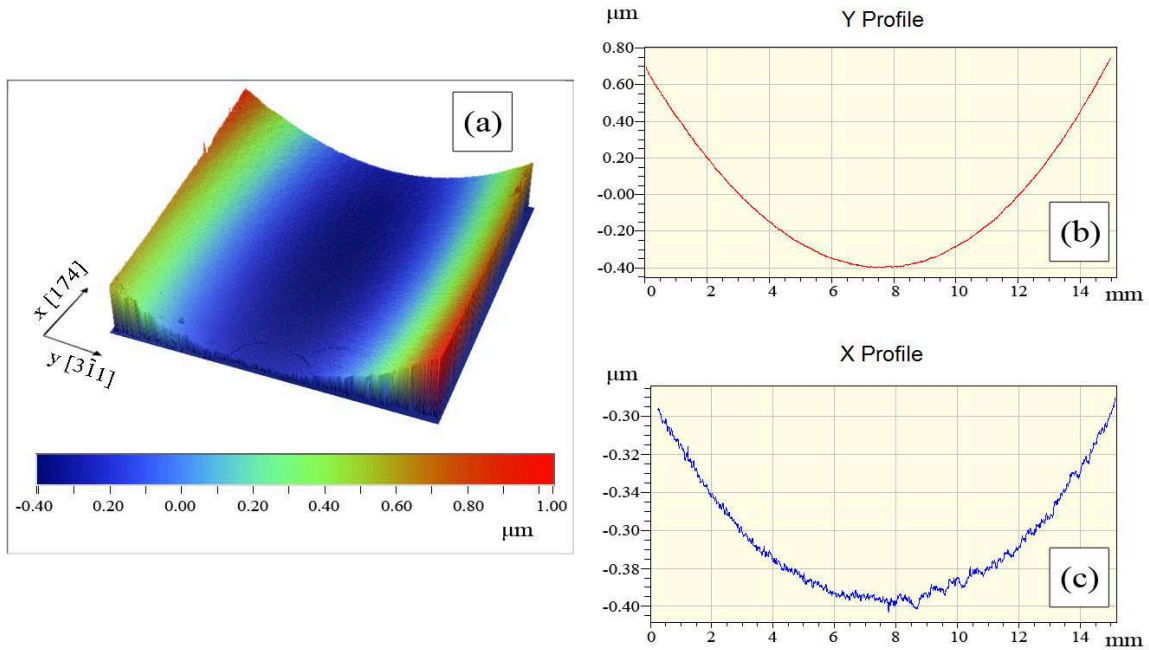
Figure 7.4: Interferometric measurement of the backside of the sample. Left side: 3d view analysis (a). Right side: Cross sections of the deformation pattern along y (b) and x directions (c), as taken at the center of the sample.

Table 7.4: Beam features

Beam energy (keV)	181.931
monochromaticity ($\Delta E/E$)	$\approx 10^{-6}$
Collimated beam size (mm^2)	1×1

carried out. The gray area in Fig. 7.5b represents the theoretical expectation, taking into account the uncertainty on the curvature of the sample. As in the case of (422) planes reported in section 7.3, beam divergence, primary and secondary curvatures were taken into accounted for the simulation. From the theory of elasticity, the ratio between QM and primary curvature is set at $\frac{R_{QM}}{R_P} = 3.455$ for the (311) planes, thus $R_{QM} = 3.455 R_p = 86.4$ m. For the calculation of diffraction efficiency, the dynamical theory was considered [65]. Finally, a morphological factor was included to consider the part of the sample that cannot diffract, i.e., the portion of material removed during the grooving process, that is about 18%.

In summary, Fig. 7.5 highlights very good agreement between the theoretical expectation and the experimental results. It can be noticed that the diffraction efficiency turns out to be not very high. However, bent crystals exploiting the (311) diffracting
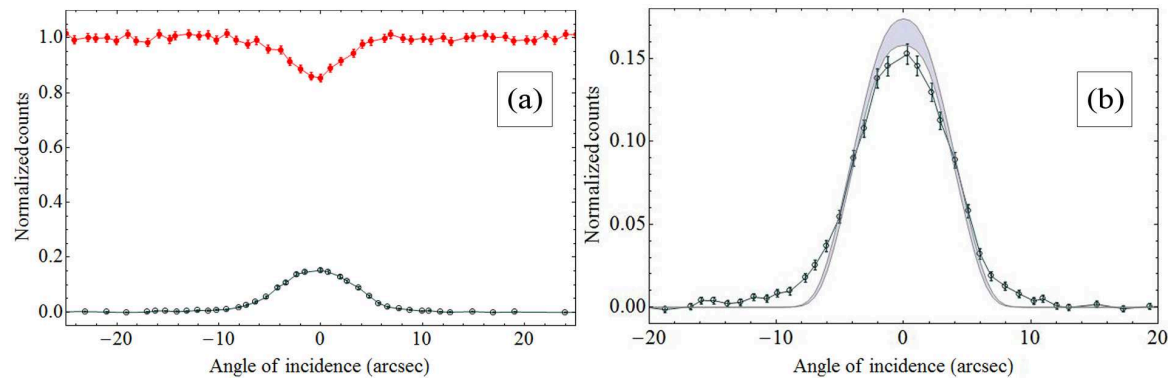
Figure 7.5: Experimental and theoretical RCs of the (311) QM crystal cylindrically bent. a) The blue empty circles plot the intensity of measured diffracted beam with their uncertainty bar, whereas the red filled points plot the transmitted beam. b) Zoom on the diffracted points. The gray area represents the expected result as calculated by taking into account the experimental uncertainties.

planes can be arranged in the external area of a Laue lens, allowing significant increase in its geometric area. Since the moderate diffraction efficiency of (311) planes is compensated for by the large geometric area they can cover, a raise in the effective area of a Laue lens becomes possible.

7.5   Conclusions

Two innovative bent silicon quasi-mosaic crystals were investigated as optical components for a Laue lens, exploiting (422) and (311) QM planes. The samples were manufactured with a self-standing curvature thanks to the grooving method, i.e., there was no need for any external holder to keep the crystal bent. Quasi-mosaicity lead to an increase in diffraction efficiency. Indeed, if there were no QM effect, the integrated reflectivity of the whole lens would be the same as that obtained from flat diffracting planes, which is relatively poor.

The combined use of several kinds of crystals and crystallographic orientations could be a viable route to realize a Laue lens with high sensitivity, which would be the condicio sine qua non for the concrete realization of a X- and γ- ray concentrator. In the next chapter, two prototypes based on the obtained results are simulated and proposed.

CHAPTER 8

Simulation of Laue lenses: the *LaueGen* code

8.1   Simulation of a Laue lens with QM crystals

In this chapter the acquired knowledge on quasi-mosaicity is applied to simulate new prototypes of Laue lenses. For the prototypes, Si and Ge crystals were chosen for two reasons. First, because they can be commercially found with high crystalline perfection, and especially because they exhibit the QM effect. A photon beam with energy between 100 and 300 keV was considered to impinge onto the crystals parallel to the axis of the lens because Si and Ge diffract X-rays at high efficiency in this energy range. Since (111), (422) and (311) planes can diffract photons of the same energy, though at very different Bragg angles, the crystals could be arranged at different positions to build up a Laue lens, featuring significant enhancement of the geometric area undergoing diffraction.

The crystal tiles were considered to be disposed as concentric rings onto the spherical calotte of a Laue lens with a focal distance $f = 20m$. Thus, the primary radius of curvature of the tiles must be twice the focal length of the lens, namely 40 m [57, 66, 63]. The thickness of the tile, T_0, affects both the focusing capability and the reflectivity of the lens. High values of T_0 lead to higher reflectivity and lower spatial resolution on the focal plane, while lower values of T_0 decrease the reflectivity but increase the focusing strength.

For a CDP crystal, the ratio between diffracted beam intensity and incident beam

intensity, that is, the crystal reflectivity η_{QM}, is given by the formula [25]

$$\eta_{QM} = (1 - e^{\frac{-\pi^2 T_0 d_{hkl}}{\Omega_{QM} \Lambda_0^2}}) e^{\frac{-\mu T_0}{\cos\theta_B}}, \tag{8.1}$$

where the first factor is the diffraction efficiency, the latter is the attenuation factor due to absorption throughout the sample, μ is the linear absorption coefficient, d_{hkl} the d-spacing of planes *(hkl)*, θ_B the Bragg angle, and Λ_0 the extinction length as defined by [26] for the Laue symmetric case. Ω_{QM} represents the bending angle of the CDPs, namely of the QM planes. Ω_{QM} can be calculated as a function of the primary curvature through Eqs.7.2 and 7.5.

The energy bandpass of a crystal in a ring is given by the formula [56]

$$\Delta_E \simeq 2\Omega_P E \frac{f}{r_{ring}}. \tag{8.2}$$

Here r_{ring} is the radius of a selected ring, Ω_P is the bending angle induced in the tile by primary curvature and E the mean energy diffracted by the ring. This latter depends on the material, crystallographic plane, and the distance from the axes of the lens, that is, the radius of the ring, as given by the formula

$$E \simeq \frac{fhc}{d_{hkl} r_{ring}}, \tag{8.3}$$

where h and c are the Planck constant and the light speed in vacuum, respectively. The small-angle approximation was considered in the last two formulae.

The effective area of an instrument at a certain energy is defined as its geometric area, as seen by the X-ray beam, times the diffraction efficiency at that energy. This parameter is important for quantifying the number of events that an ideal detector located on the focus of the Laue lens would count under exposure to a certain photon flux. As for any tile in the lens, the effective area at a given energy is defined as the geometric area exposed to the photon flux times the reflectivity of the tile at the energy of interest. Because of the finite angle Ω_{QM} exposed to photon flux, only a part of the tile is capable of diffracting a certain photon energy. Thus, the effective area A_{Eff} for a single tile is given by

$$A_{Eff} = (\frac{d\Omega_P}{d\Omega} * \frac{d\epsilon_{QM}}{d\Omega}) A_{tile}, \tag{8.4}$$

where the first function in the convolution is the normalized distribution of diffracting planes due to the primary curvature, the second function is the distribution of

reflectivity due to the QM curvature as function of the diffracting angle Ω, and A_{tile} is the geometric area of each tile. The effective area of the whole lens is the sum of the effective areas of the tiles composing the lens itself. For the simulation, the effective area was calculated as a discrete function of energy, the step being 0.5 keV. This value was selected because it is a good compromise between accuracy and computational time.

As an estimator of the smoothness of the effective area as a function of the photon energy, the quantity *smoothing* was defined in the following way. Firstly, the moving average of the effective area was calculated for five sequential values of energy starting from the minimum (100 keV). Then, the distance between these five values of A_{Eff} and their average value was calculated and the largest distance was selected. This procedure was repeated by shifting the section under analysis along the energy axis, up to the maximum energy (300 keV). The quantity *smoothing* was defined as the sum of all the collected contributions of maximum distances.

To maximize and smoothen the effective area of the simulated Laue lens, a computational method based on a genetic algorithm, named *LaueGen*, was implemented. As a first step, a Laue lens was generated, composed of Si and Ge QM crystalline tiles. A tile of the lens was chosen arbitrarily and was randomly transformed into a tile of different species by changing the material and/or the crystallographic orientation.

It is possible to define a quantifier $k[i]$ of both the effective area for all the energies and the smoothness of the effective area itself.

$$k[i] = w_1 \frac{\int_{E_{min}}^{E_{max}} A_{Eff}[i+1] \, dE}{\int_{E_{min}}^{E_{max}} A_{Eff}[i] \, dE} - w_2 \frac{smoothing[i+1]}{smoothing[i]}, \tag{8.5}$$

where the index $[i]$ represents the configuration before crystal transformation, while the index $[i+1]$ represents the configuration after crystal transformation. w_1 and w_2 are weights that have to be assigned in Eq. 8.5. By increasing w_1 it is possible to achieve a high value of the total effective area, while an increase of w_2 favors a better smoothness. The minus sign before the second term of the equation indicates that the second quantity has to be minimized, while the first has to be maximized.

If $k[i+1] > k[i]$, the crystal exchange is held, otherwise it is rejected. This procedure was iterated until the system reached thermalization, that is, the maximum of $k[i]$ was attained.

Table 8.1: Lens features

inner radius	0.25 m
outer radius	2.26 m
focal length	20 m
number of rings	100
geometric area	158496 cm^2
crystal radial length	20 mm
crystal tangential length	10 mm
crystal thickness	5 mm

Table 8.2: Crystals features

material	Ge (111)	Si (111)	Ge (422)	Si (422)	Total
samples	2259	4778	34629	36254	77920
mass (kg)	12.0	11.1	184.3	84.5	292.0

8.2 Simulation of a Laue lens with (111) and(422) QM crystals

A Laue lens composed of Ge and Si QM crystals was simulated. The crystals were chosen all with the same tile size 20×10 mm^2, with the longer side parallel to the direction where focalization occurs, that is, the radial direction. This choice of tile size reduces the blank space between tiles, while T_0 was chosen to be 5 mm to guarantee high reflectivity. The crystals were arranged in the lens thanks to *LaueGen*. The algorithm was initialized by starting with an *a priori* initial guess for the tile arrangement in the Laue lens, taking into account the different Bragg angles. Fig. 8.1 shows a possible arrangement of the QM tiles in a Laue lens, and quantitative results are listed in Tab. 8.3. Fig. 8.2 represents the spectral effective area of the lens, in which the contributions of the four species are visible.

To verify that the final arrangement was not affected by the initial guess and to control possible interference of local maxima in the quantifier in Eq. 8.5, *LaueGen* was re-initialized by a fully casual disposition of the tiles. After a much longer computing time, a similar arrangement to the previous simulation was obtained.

Since the lens was composed of QM tiles $20 \times 10 \times 5$ mm^3 of size with the focusing curvature along the wider dimension, all the diffracted photons were enclosed in a circle of 10 mm in diameter. To evaluate the capability of focalization of this Laue lens, a Monte Carlo code was written to simulate an on-axis photon beam hitting the

Table 8.3: Number of tiles per type normalized to the number of samples per ring.

| Ring	Tiles	Ge (111)	Si (111)	Ge (422)	Si (422)	Ring	Tiles	Ge (111)	Si (111)	Ge (422)	Si (422)
1	157	1.000	-	-	-	51	786	-	-	0.673	0.327
2	169	1.000	-	-	-	52	798	-	-	0.733	0.267
3	182	0.984	0.016	-	-	53	811	-	-	0.720	0.280
4	194	0.938	0.062	-	-	54	823	-	-	0.710	0.290
5	207	0.831	0.169	-	-	55	836	-	-	0.630	0.370
6	220	0.723	0.277	-	-	56	848	-	-	0.610	0.390
7	232	0.664	0.336	-	-	57	861	-	-	0.602	0.398
8	245	0.620	0.380	-	-	58	874	-	-	0.580	0.420
9	257	0.560	0.440	-	-	59	886	-	-	0.569	0.431
10	270	0.548	0.452	-	-	60	899	-	-	0.558	0.442
11	282	0.291	0.709	-	-	61	911	-	-	0.542	0.458
12	295	0.268	0.732	-	-	62	924	-	-	0.528	0.472
13	308	0.136	0.864	-	-	63	936	-	-	0.496	0.504
14	320	0.075	0.925	-	-	64	949	-	-	0.474	0.526
15	333	0.045	0.955	-	-	65	962	-	-	0.467	0.533
16	345	0.055	0.945	-	-	66	974	-	-	0.441	0.559
17	358	0.075	0.925	-	-	67	987	-	-	0.432	0.568
18	371	0.111	0.889	-	-	68	999	-	-	0.428	0.572
19	383	0.131	0.869	-	-	69	1012	-	-	0.416	0.584
20	396	0.172	0.828	-	-	70	1024	-	-	0.406	0.594
21	408	0.189	0.811	-	-	71	1037	-	-	0.402	0.598
22	421	0.211	0.789	-	-	72	1050	-	-	0.387	0.613
23	433	0.028	0.661	0.312	-	73	1062	-	-	0.389	0.611
24	446	0.025	0.267	0.709	-	74	1075	-	-	0.390	0.610
25	459	0.004	0.248	0.725	0.022	75	1087	-	-	0.397	0.603
26	471	0.011	0.200	0.771	0.019	76	1100	-	-	0.397	0.603
27	484	-	0.056	0.928	0.017	77	1112	-	-	0.394	0.606
28	496	-	0.028	0.925	0.046	78	1125	-	-	0.405	0.595
29	509	-	-	0.953	0.047	79	1138	-	-	0.416	0.584
30	521	-	-	0.948	0.052	80	1150	-	-	0.418	0.582
31	534	-	-	0.934	0.066	81	1163	-	-	0.433	0.567
32	547	-	-	0.925	0.075	82	1175	-	-	0.447	0.553
33	559	-	-	0.928	0.072	83	1188	-	-	0.461	0.539
34	572	-	-	0.907	0.093	84	1200	-	-	0.468	0.532
35	584	-	-	0.914	0.086	85	1213	-	-	0.496	0.504
36	597	-	-	0.868	0.132	86	1226	-	-	0.458	0.542
37	609	-	-	0.849	0.151	87	1238	-	-	0.481	0.519
38	622	-	-	0.860	0.140	88	1251	-	-	0.488	0.512
39	635	-	-	0.838	0.162	89	1263	-	-	0.298	0.702
40	647	-	-	0.822	0.178	90	1276	-	-	0.260	0.740
41	660	-	-	0.811	0.189	91	1288	-	-	0.254	0.746
42	672	-	-	0.795	0.205	92	1301	-	-	0.258	0.742
43	685	-	-	0.778	0.222	93	1314	-	-	0.202	0.798
44	698	-	-	0.756	0.244	94	1326	-	-	0.179	0.821
45	710	-	-	0.749	0.251	95	1339	-	-	0.163	0.837
46	723	-	-	0.743	0.257	96	1351	-	-	0.194	0.806
47	735	-	-	0.721	0.279	97	1364	-	-	-	1.000
48	748	-	-	0.713	0.287	98	1376	-	-	-	1.000
49	760	-	-	0.707	0.293	99	1389	-	-	-	1.000
50	773	-	-	0.684	0.316	100	1401	-	-	-	1.000
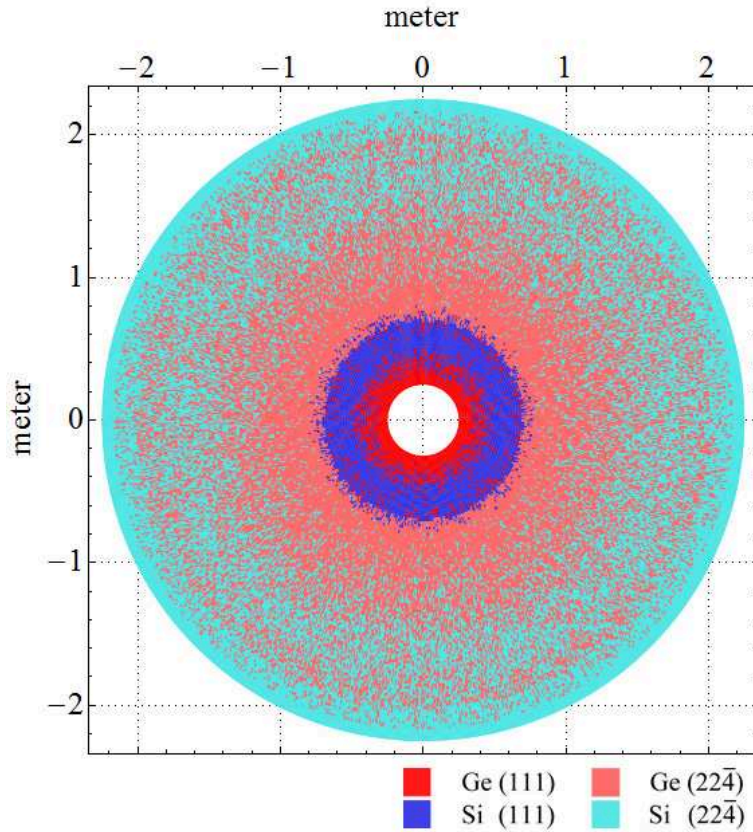
Figure 8.1: Arrangement of crystalline tiles over the calotte of the simulated Laue lens. The legend describes the diffracting plane employed. The crystals are $20\times10\times5$ mm^3 Ge tiles. The disposition of the tiles is optimized thanks to *LaueGen* code

lens within the energy range of 100-300 keV. The concentration of photons is high at the center of the spot and rapidly decreases close to the borders, as is clearly visible in Figs.8.3 and 8.4.

8.3   Discussion

Diffraction from (422) CDP occurs at a Bragg angle much larger than for the (111) planes at the same energy. This means that the crystalline tiles implementing (111) CDP occupy the innermost part of the lens because of the small Bragg angle. In contrast, tiles using (422) CDP occupy the outermost part of the lens because of the large Bragg angle. Although the reflectivity for (422) CDP is lower than for (111) CDP, the external position guarantees a large geometric area, resulting in a large effective area. Moreover, this configuration works with Ge and Si crystals simultaneously owing to their different d-spacing, that is, still more locations for crystalline tiles are
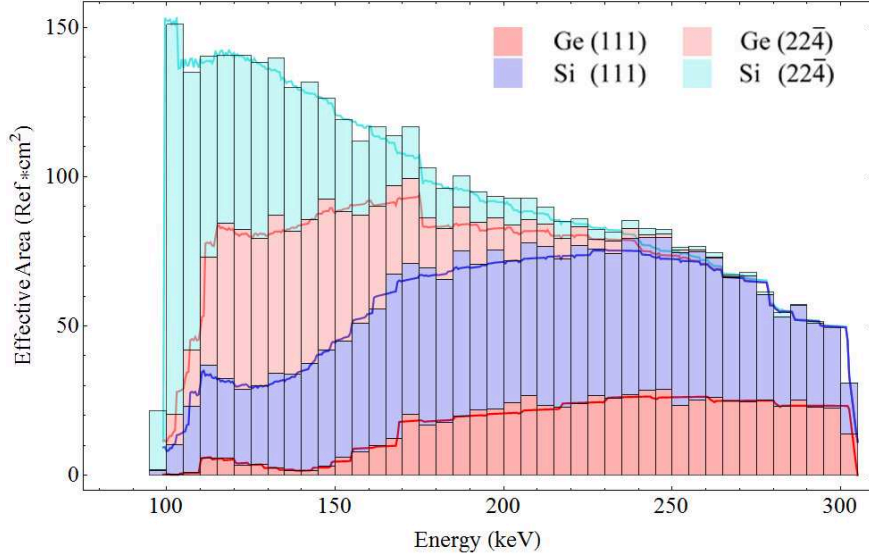
Figure 8.2: Effective area per unit energy of the lens. The contributions of the tiles of different species is visible. Tiles were positioned in the lens to maximize effective area in the energy range 100-300 keV and made the profile as smooth as possible with respect to energy variation. The histogram is calculated analytically, while the continuous lines are calculated with a Monte Carlo simulation.

generated. In summary, the possibility to build up a lens with very large geometric area has been demonstrated. Si crystals provide the largest part of the effective area at low energies, as expected for a light material. Ge tiles, which are composed of a material with higher atomic number, maximize their reflectivity for high energies, providing the largest part of effective area in this zone.

The photon distribution on the focal plane are well-collimated as a result of focusing through QM tiles. This peculiarity is expected to provide high-quality focusing. A quantifier of the focusing capability is the focusing factor G, defined as

$$G = f_{ph} \frac{A_{eff}}{A_d}, \tag{8.6}$$

where A_{eff} is the effective area of the lens and A_d is the area of the focal spot that contains a fraction f_{ph} of photons reflected by the lens. Physically, it represents the number of photons enclosed in a focal spot divided by the area of the focal spot and normalized with respect to the photon flux impinging on the lens. To calculate the focusing factor, the radius of the focal spot R_{spot} was chosen to enclose 90% of the photons, cutting the tails of the distribution, that is, $R_{spot} = 4.66mm$. Fig. 8.5 shows the focusing factor of the lens as a function of the energy of impinging photons.
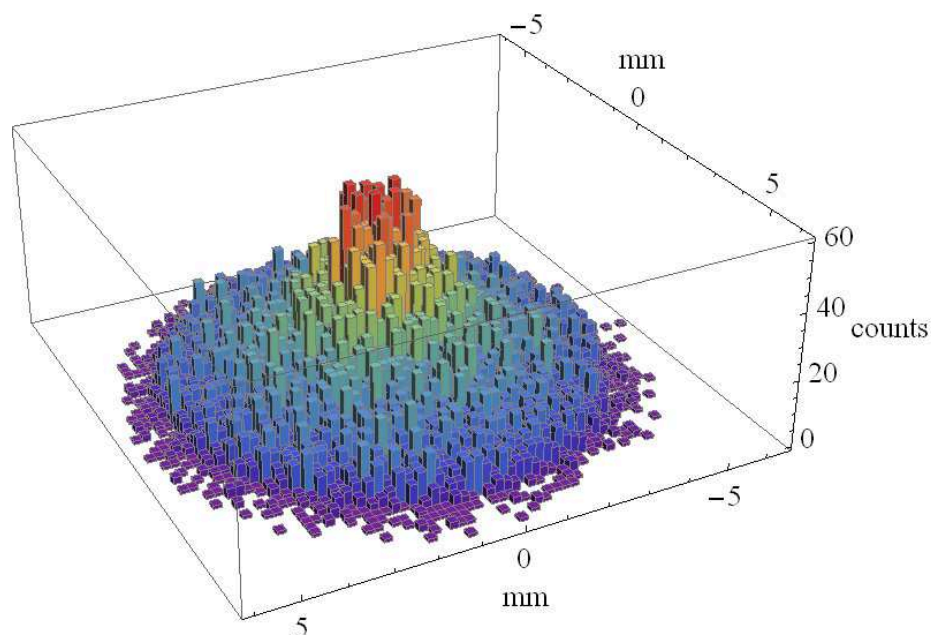
Figure 8.3: Photon distribution onto the focal plane of the lens in arbitrary units. Concentration of photons is high in the focal point and rapidly decreases far from the center. The distribution is obtained with a Monte Carlo code.
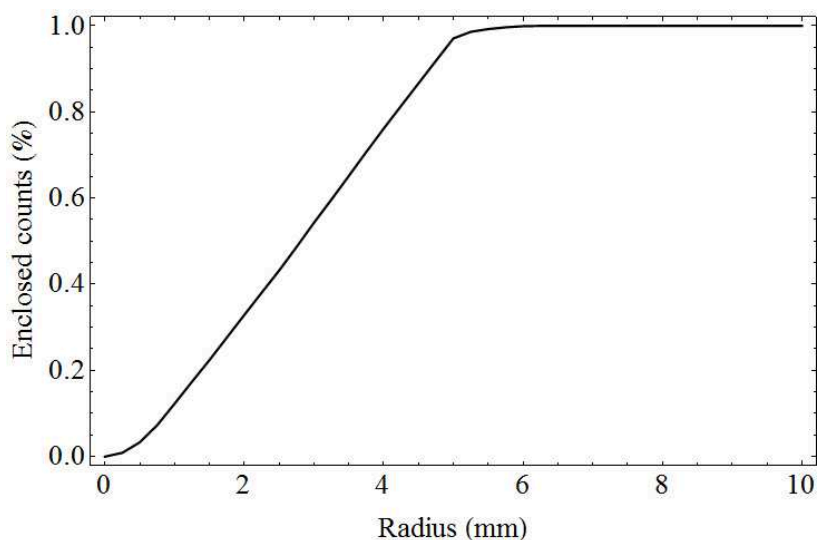

Figure 8.4: Fraction of enclosed photons vs. radius of the focal spot enclosing the photons on the focal plane. The radius R_{spot} corresponding to 90% of the enclosed photons was chosen for the simulation to cut the tails of the focal distribution. $R_{spot} = 4.66mm$
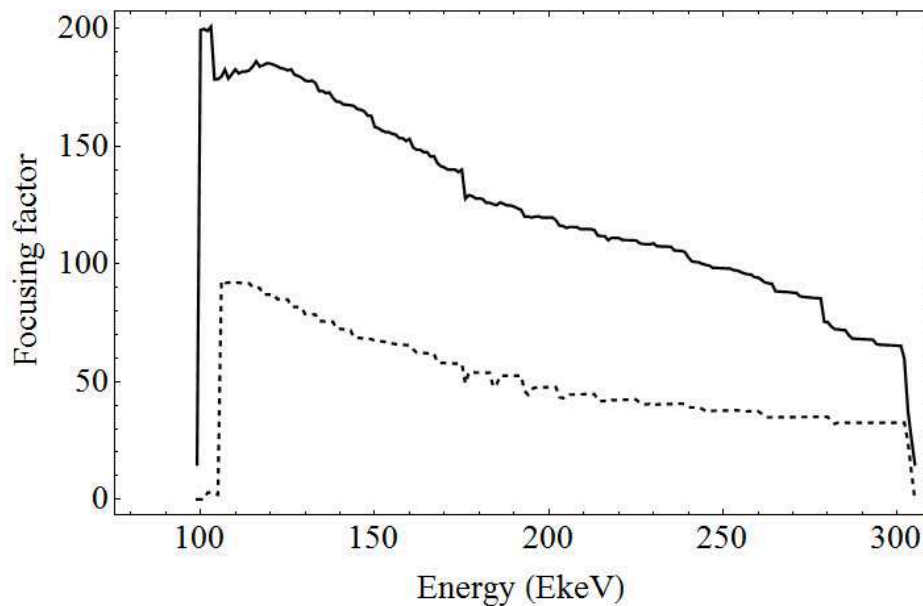
Figure 8.5: Focusing factor of a lens composed of QM (422) and (111) crystalline tiles (continuous line), or composed of QM (111) tiles only (dashed line), in an energy range of the lens of 100-300 keV.

For the sake of comparison, it was simulated the performance of a Laue lens consisting solely of Si and Ge QM (111) tiles and optimized for the purpose. The dimension of QM tiles, the curvature radius and the energy bandpass of the lens are the same as in the previous case. A lens made of (111) QM crystals results in a smaller effective area and then in a smaller focusing factor, as visible in Fig. 8.5.

Finally, the performance of the lens is expressed in terms of the most often acknowledged quantifier recognized by the community of astrophysicists, namely the sensitivity, that is, the lowest flux detectable with 3 sigma significance, for the cases of continuum- and narrow-line emissions. The results are shown in Fig. 8.6, which are in line with the sensitivity of the proposed Laue lens for the Gamma Ray Imager (GRI) [21]. Indeed, the smaller effective area of the QM-based Laue lens, which results from the usage of QM crystals, is abundantly compensated by the strong focusing exerted by the QM effect. In fact, the property of QM crystals to focus on a spot smaller than the dimension of the diffracting crystals themselves raises the sensitivity of the lens. Another advantage of the proposed lens is that its focal length is expected to allow the lens to be accommodated in one spacecraft only despite its relatively large diameter, resulting in a modest weight (292 kg) of the diffracting crystals. If a longer focal length was considered, with two satellites flying in formation as for the GRI, a still better figure of merit would be attained (effective area would increase to 1000
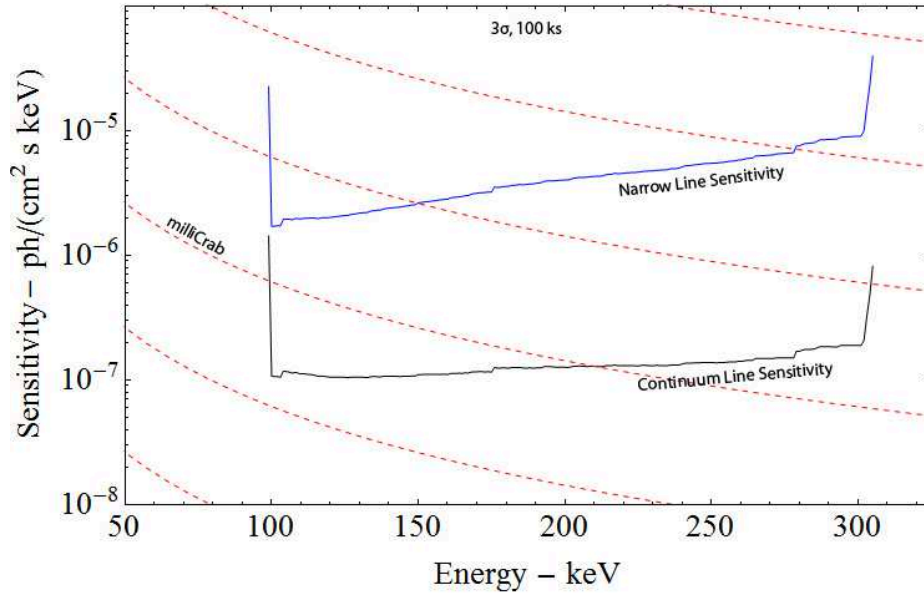
Figure 8.6: Predicted 3σ detection sensitivities for continuum (black) and narrow line (blue) emission, assuming an exposure time of 100 ks and $\Delta E/E = 1/2$ for the continuum and $\Delta E/E = 3\%$ for the line sensitivity.

cm^2 at 100 m focal length).

8.4 Simulation of a Laue lens including (311) QM crystals

A Laue lens consisting of (111), (422) and (311) curved QM planes was generated and simulated. The crystallographic planes used are the most efficient QM planes achievable. For this case, the crystals were chosen $10\times30\ mm^2$ of size, with the longer side parallel to the direction where focalization occurs, namely the radial direction. T_0 was chosen to be 5 mm to guarantee high reflectivity.

To maximize the effective area of the simulated Laue lens and smoothen its energy dependence, the *LaueGen* code was employed. The algorithm was initialized by starting with an *a priori* initial guess for the tile arrangement, taking into account the different Bragg angles. Fig. 8.7 shows a possible arrangement of the QM tiles as result of the simulation and quantitative results are listed in Tab. 8.6. Fig. 8.8 represents the spectral effective area of the lens, in which the contributions of the six species are visible.

Since the lens was composed of QM tiles $10\times30\times5$ mm^3 of size with the focusing
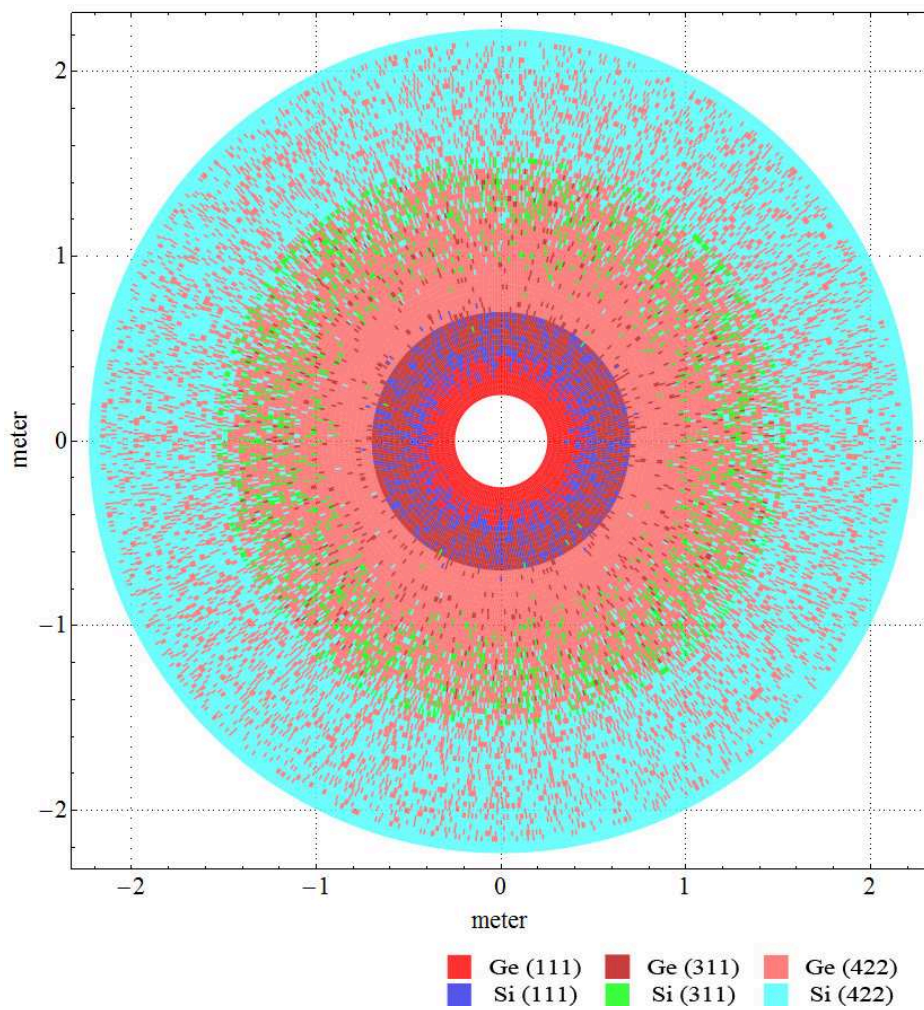
Figure 8.7: Arrangement of crystalline tiles over the calotte of the simulated Laue lens. The legend describes the diffracting plane employed. The crystals are $10 \times 30 \times 5$ mm^3 Si and Ge tiles. The disposition of the tiles is optimized with a specifically written code.

curvature along the wider dimension, all the photons diffracted were enclosed in a circle of 10 mm in diameter. To evaluate the capability of focalization of this Laue lens, a Monte Carlo code was compiled to simulate an on-axis photon beam hitting the lens within the energy range of 100-300 keV. The concentration of photons is high at the center of the spot and rapidly decreases close to the borders, as is clearly visible in Figs. 8.9-8.10.

The focusing factor G was calculated. For this purpose, the radius of the focal spot R_{spot} was chosen to enclose 90% of the photons, cutting the tails of the distribution, that is, $R_{spot} = 4.64mm$. Fig. 8.11 shows the focusing factor of the lens as a function of the energy of impinging photons. Finally, the performance of the lens is expressed

Table 8.4: Lens features

inner radius	0.25 m
outer radius	2.23 m
focal length	20 m
number of rings	66
crystal radial length	30 mm
crystal tangential length	10 mm
crystal thickness	5 mm

Table 8.5: Crystals features

Material	Ge (111)	Si (111)	Ge (311)	Si (311)	Ge (422)	Si (422)	Total
samples	1314	1201	2567	2278	19837	23594	50791
mass (kg)	10.49	4.20	158.4	82.46	20.50	7.96	284.0

in terms of the the sensitivity. The results are shown in Fig. 8.12.

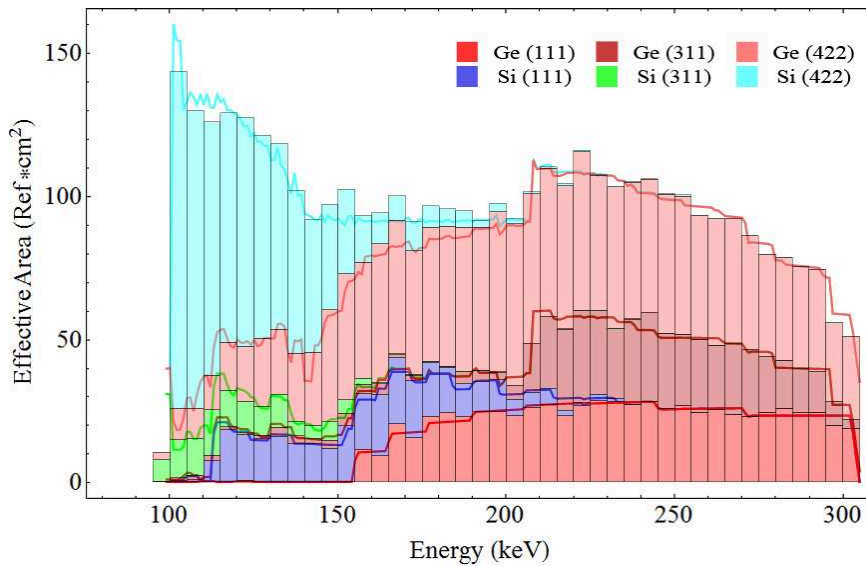Figure 8.8: Effective area per unit energy of the lens. The contributions of the tiles of different species are visible. Tiles were positioned in the lens to maximize effective area in the energy range 100-300 keV and made the profile as smooth as possible with respect to energy variation. The histogram is calculated analytically, while the continuous lines are calculated with a Monte Carlo simulation.

Table 8.6: Number of tiles per type normalized to the number of samples per ring.

| Ring	Tiles	Ge (111)	Si (111)	Ge (311)	Si (311)	Ge (422)	Si (422)
1	157	1.000	0.000	0.000	0.000	0.000	0.000
2	175	1.000	0.000	0.000	0.000	0.000	0.000
3	194	1.000	0.000	0.000	0.000	0.000	0.000
4	213	0.920	0.080	0.000	0.000	0.000	0.000
5	232	0.806	0.194	0.000	0.000	0.000	0.000
6	251	0.657	0.343	0.000	0.000	0.000	0.000
7	270	0.526	0.474	0.000	0.000	0.000	0.000
8	289	0.318	0.536	0.145	0.000	0.000	0.000
9	308	0.000	0.416	0.584	0.000	0.000	0.000
10	326	0.000	0.270	0.730	0.000	0.000	0.000
11	345	0.000	0.258	0.742	0.000	0.000	0.000
12	364	0.000	0.299	0.701	0.000	0.000	0.000
13	383	0.005	0.248	0.742	0.005	0.000	0.000
14	402	0.000	0.281	0.714	0.005	0.000	0.000
15	421	0.010	0.321	0.663	0.007	0.000	0.000
16	440	0.000	0.000	0.139	0.000	0.861	0.000
17	458	0.000	0.028	0.061	0.002	0.906	0.002
18	477	0.000	0.000	0.099	0.002	0.899	0.000
19	496	0.000	0.000	0.002	0.004	0.992	0.002
20	515	0.000	0.000	0.025	0.000	0.973	0.002
21	534	0.000	0.000	0.019	0.009	0.972	0.000
22	553	0.000	0.000	0.063	0.004	0.920	0.013
23	572	0.000	0.000	0.061	0.016	0.911	0.012
24	590	0.000	0.000	0.075	0.032	0.888	0.005
25	609	0.000	0.000	0.061	0.069	0.862	0.008
26	628	0.000	0.000	0.035	0.121	0.828	0.016
27	647	0.000	0.000	0.040	0.060	0.856	0.043
28	666	0.000	0.000	0.056	0.092	0.838	0.015
29	685	0.000	0.000	0.079	0.082	0.780	0.060
30	704	0.000	0.000	0.026	0.153	0.740	0.081
31	722	0.000	0.000	0.050	0.151	0.720	0.079
32	741	0.000	0.000	0.020	0.148	0.692	0.139
33	760	0.000	0.000	0.033	0.179	0.661	0.128
34	779	0.000	0.000	0.041	0.187	0.637	0.135
35	798	0.000	0.000	0.040	0.147	0.608	0.206
36	817	0.000	0.000	0.037	0.191	0.611	0.162
37	836	0.000	0.000	0.011	0.179	0.646	0.164
38	854	0.000	0.000	0.032	0.211	0.550	0.207
39	873	0.000	0.000	0.031	0.142	0.623	0.204
40	892	0.000	0.000	0.021	0.157	0.519	0.303
41	911	0.000	0.000	0.029	0.108	0.515	0.349
42	930	0.000	0.000	0.000	0.109	0.417	0.474
43	949	0.000	0.000	0.000	0.298	0.212	0.490
44	968	0.000	0.000	0.000	0.000	0.412	0.588
45	986	0.000	0.000	0.000	0.000	0.252	0.748
46	1005	0.000	0.000	0.000	0.000	0.368	0.632
47	1024	0.000	0.000	0.000	0.000	0.293	0.707
48	1043	0.000	0.000	0.000	0.000	0.362	0.638
49	1062	0.000	0.000	0.000	0.000	0.305	0.695
50	1081	0.000	0.000	0.000	0.000	0.276	0.724
51	1100	0.000	0.000	0.000	0.000	0.255	0.745
52	1118	0.000	0.000	0.000	0.000	0.263	0.737
53	1137	0.000	0.000	0.000	0.000	0.257	0.743
54	1156	0.000	0.000	0.000	0.000	0.252	0.748
55	1175	0.000	0.000	0.000	0.000	0.236	0.764
56	1194	0.000	0.000	0.000	0.000	0.275	0.725
57	1213	0.000	0.000	0.000	0.000	0.298	0.702
58	1232	0.000	0.000	0.000	0.000	0.282	0.718
59	1250	0.000	0.000	0.000	0.000	0.175	0.825
60	1269	0.000	0.000	0.000	0.000	0.221	0.779
61	1288	0.000	0.000	0.000	0.000	0.191	0.809
62	1307	0.000	0.000	0.000	0.000	0.138	0.862
63	1326	0.000	0.000	0.000	0.000	0.207	0.793
64	1345	0.000	0.000	0.000	0.000	0.191	0.809
65	1364	0.000	0.000	0.000	0.000	0.000	1.000
66	1382	0.000	0.000	0.000	0.000	0.000	1.000
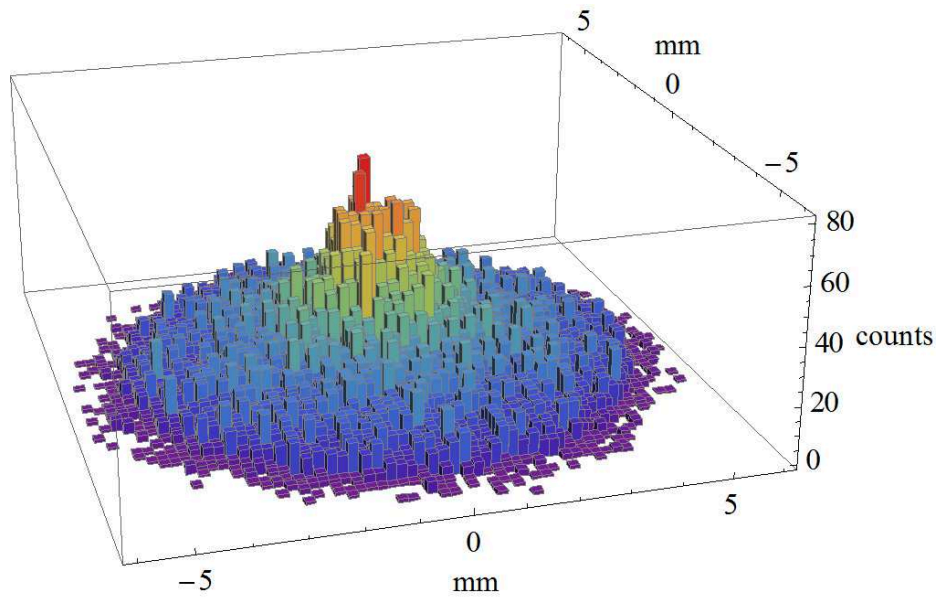
Figure 8.9: Photon distribution onto the focal plane of the lens in arbitrary units. Concentration of photons is high in the focal point and rapidly decreases far from the center. The distribution is obtained with a Monte Carlo code.
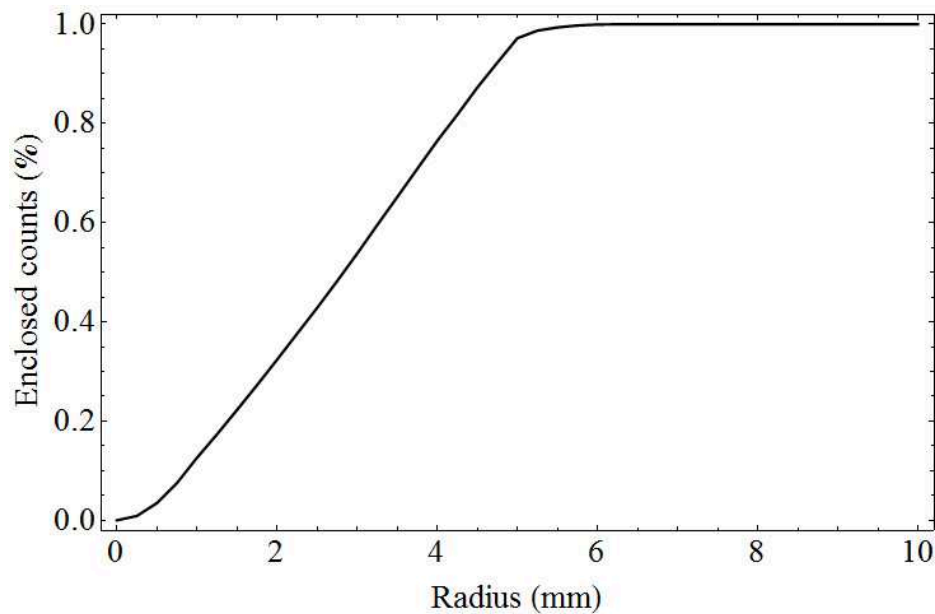

Figure 8.10: Fraction of enclosed photons vs. radius of the focal spot enclosing the photons on the focal plane. The radius R_{spot} corresponding to 90% of the enclosed photons was chosen for the simulation to cut the tails of the focal distribution. $R_{spot} = 4.64mm$
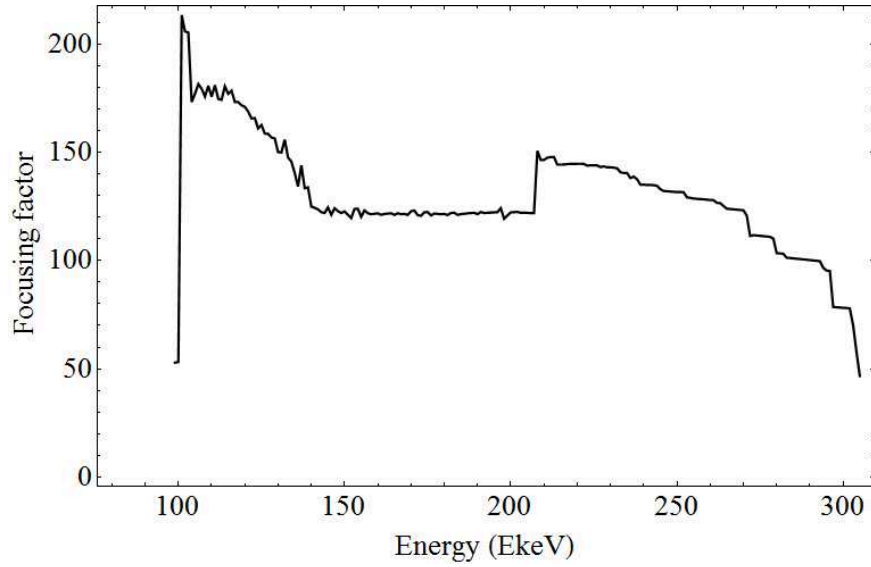
Figure 8.11: Focusing factor of the simulated lens in the energy range of 100-300 keV.
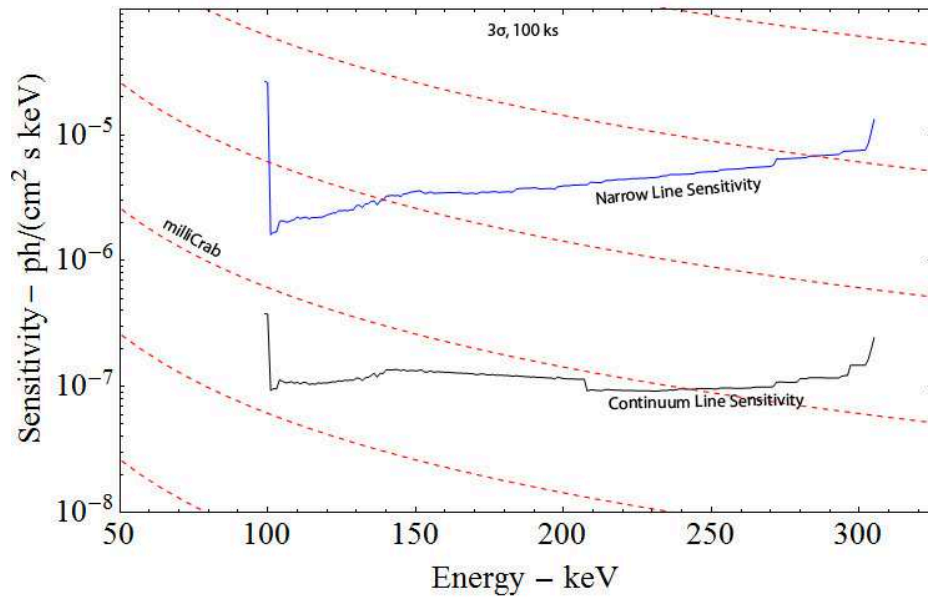

Figure 8.12: Predicted 3σ detection sensitivities for continuum (black) and narrow line (blue) emission, assuming an exposure time of 100 ks and $\Delta E/E = 1/2$ for the continuum and $\Delta E/E = 3\%$ for the line sensitivity.

8.5   Conclusions

The idea of a Laue lens to focalize X- and γ-rays was proposed about thirty years ago with a scheme entirely based on mosaic crystals. Compared to the initial formulation, significant progresses have been done, which bring the concept of a Laue lens within reach. Here, two novel configurations are proposed, based solely on quasi-mosaic crystals, with hybrid Si and Ge samples exploiting traditional (111) planes and (422) and (311) diffracting planes as innovative concepts. with these configurations, it is possible to enhance the capability of the lens by a factor larger than two compared with a Laue lens made of only one species of QM crystals. High sensitivity was obtained as a result of the strong focusing capability due to the quasi-mosaic effect. Thanks to the possibility of employing different diffracting planes with different d-spacing, a lens with very high focusing factor and sensitivity can be obtained.

Conclusions

In this Ph.D. thesis a feasibility study for the development of optical elements capable of concentrating hard X-rays with high resolution for a Laue lens has been pursued.

The usage of bent silicon and germanium crystals allows achieving very high diffraction efficiency. For a practical implementation of a focusing telescope for satellite-borne experiments (e.g. a Laue lens), self-standing bent crystals and a manufacturing method mass-production oriented are required. To this aim, this thesis proposes the grooving method as a technique meeting in full both requirements, other than being economical and simple. Grooved samples were tested at ESRF and at ILL, with monochromatic and polychromatic X- and γ rays, showing diffraction efficiency up to 95%, a level unreachable with mosaic crystals. Furthermore, the concept of quasi-mosaicity was studied and applied to obtain high-resolution optical elements. Thanks to the study of the linear theory of elasticity in anisotropic media, unusual crystallographic orientations bent by the quasi-mosaic effect were investigated and experimentally verified at ILL.

The combined usage of the grooving method and the quasi-mosaic effect was employed for the production of 150 germanium samples as optical elements for the building of a prototype of Laue lens. This prototype was developed within the Laue project, a project financed by the Italian Space Agency (ASI).

Finally, a genetic algorithm named *LaueGen* was implemented to simulate two prototypes of Laue lens. These prototypes are entirely based on quasi-mosaic crystals. It was demonstrated that with quasi-mosaic crystals it is possible to achieve unprecedented focusing capability, since they allows concentrating the diffracted X-rays onto a focal spot smaller than the crystals size.

Based on the knowledge gained during the Ph.D. period, novel techniques will be studied to produce new optical elements in the next future. Moreover, innovative prototypes of Laue lens will be proposed through the use of the *LaueGen* code.

Acknowledgments

Bibliography

[1] Mónica Fernández-Perea, Marie-Anne Descalle, Regina Soufli, Klaus P. Ziock, Jennifer Alameda, Sherry L. Baker, Tom J. McCarville, Veijo Honkimäki, Eric Ziegler, Anders C. Jakobsen, Finn E. Christensen, and Michael J. Pivovaroff. Physics of reflective optics for the soft gamma-ray photon energy range. *Phys. Rev. Lett.*, 111:027404, 2013.

[2] M. Leventhal, C.J. MacCallum, and P.D. Stang. Detection of 511 kev positron annihilation radiation from the galactic center direction. *Astrophys. J.*, 225:L11–L14, 1978.

[3] Donald D. Clayton. Positronium origin of 476 kev galactic feature. *Nature Phys. Sci.*, 244:137–138, 1973.

[4] Donald D. Clayton and Fred Hoyle. Gamma-ray lines from novae. *Astrophys. J.*, 187:L101–L103, 1974.

[5] Nikos Prantzos and Michel Casse. On the production of aluminum-26 by wolf-rayet stars: galactic yield and gamma-ray line emissivity. *Astrophys. J.*, 307:324–331, 1986.

[6] R. Ramaty and R. E. Lingenfelter. Gamma-ray line astronomy. *Nature*, 278:127–132, 1979.

[7] N. Guessoum, P. Jean, and N. Prantzos. Microquasars as sources of positron annihilation radiation. *Astron. Astrophys.*, 457:753–762, 2006.

[8] K. S. Cheng, D. O. Chernyshov, and V. A. Dogiel. Annihilation emission from the galactic black hole. *Astrophys. J.*, 645:1138–1151, 2006.

[9] Tomonori Totani. A riaf interpretation for the past higher activity of the galactic center black hole and the 511 kev annihilation emission. *Astron. Soc. Jpn*, 58:965–977, 2006.

[10] Celine Boehm, Dan Hooper, Joseph Silk, Michel Casse, and Jacques Paul. Mev dark matter: Has it been detected? *Phys. Rev. Lett.*, 92:101301/1–101301/4, 2004.

[11] R. K. Smither, K. A. Saleem, D. E. Roa, M. A. Beno, P. V. Ballmoos, and G. K. Skinner. High diffraction efficiency, broadband, diffraction crystals for use in crystal diffraction lenses. *Exp. Astron.*, 20:201–210, 2005.

[12] D. Roa, R. Smither, X. Zhang, K. Nie, Y. Shieh, N. Ramsinghani, N. Milne, J. Kuo, J. Redpath, M. Al-Ghazi, and P. Caligiuri. Development of a new photon diffraction imaging system for diagnostic nuclear medicine. *Exp. Astron.*, 20:229–239, 2005.

[13] V. Guidi, V. Bellucci, R. Camattari, and I. Neri. Proposal for a laue lens with quasi-mosaic crystalline tiles. *J. Appl. Cryst.*, 44:1255–1258, 2011.

[14] R. Camattari, V. Guidi, V. Bellucci, I. Neri, and M. Jentschel. Self-standing quasi-mosaic crystals for focusing hard x-rays. *Rev. Sci. Instrum.*, 84:053110 – 053110–4, 2013.

[15] P. Von Ballmoos. Gamma-ray optics for high-energy astrophysics. *Nucl. Instr. Meth. B*, 309:244–248, 2013.

[16] P. Ubertini, F. Lebrun, G. Di Cocco, A. Bazzano, A. J. Bird, K. Broenstad, A. Goldwurm, G. La Rosa, C. Labanti, P. Laurent, I. F. Mirabel, E. M. Quadrini, B. Ramsey, V. Reglero, L. Sabau, B. Sacco, R. Staubert, L. Vigroux, M. C. Weisskopf, and A. A. Zdziarski. Ibis: The imager on-board integral. *Astron and Astrophys*, 411:L131–L139, 2003.

[17] P. Von Ballmoos, M. Güdel, S. M. Kahn, and R. Sunjaev. *High energy spectroscopic astrophysics.* Springer, 2005.

[18] R. K. Smither. New method for focusing x rays and gamma rays. *Rev. Sci. Instrum.*, 53:131, 1982.

[19] N. Lund. A study of focusing telescopes for soft gamma rays. *Exp Astron*, 2:259–273, 1992.

[20] P. von Ballmoos, H. Halloin, J. Evrad, G. Skinner, N. Abrosimov, J. Alvarez, P. Bastie, B. Hamelin, M. hernanz, P. Jean, J. Knödlseder, and R. K. Smither. Claire: First light for a gamma-ray lens. *Exp. Astron.*, 20:253–267, 2005.

[21] J. Knödlseder, P. von Ballmoos, F. Frontera, A. Bazzano, F. Christensen, M. Hernanz, and C. Wunderer. Gri: focusing on the evolving violent universe. *Exp. Astron.*, 23:121–138, 2009.

[22] D. Pellicciotta, F. Frontera, G. Loffredo, A. Pisa, K. Andersen, P. Courtois, B. Hamelin, V. Carassiti, M. Melchiorri, and S. Squerzanti. Laue lens development for hard x-rays (> 60 kev). *IEEE Transactions on Nuclear Science*, 53:253–258, 2006.

[23] A. Pisa, F. Frontera, G. Loffredo, D. Pellicciotta, and N. Auricchio. Optical properties of laue lenses for hard x-rays (> 60 kev). *Exp. Astron.*, 20:219–228, 2005.

[24] William H. Zachariasen. *Theory of X-ray diffraction in crystals.* J. Wiley and sons, inc., 1945.

[25] Cécile Malgrange. X-ray propagation in distorted crystals: From dynamical to kinematical theory. *Cryst. Res. and Tech.*, 37:654–662, 2002.

[26] A. Authier. *Dynamical theory of X-ray diffraction.* Oxford University Press, 2001.

[27] Hubert Halloin and Pierre Bastie. Laue diffraction lenses for astrophysics: Theoretical concepts. *Exp. Astron.*, 20:151–170, 2005.

[28] S. Keitel, C. Malgrange, T. Niemöller, and J. R. Schneider. Diffraction of 100 to 200 kev x-rays from an $Si_{1-x}Ge_x$ gradient crystal: comparison with results from dynamical theory. *Acta Crystallogr. A*, A55:855–863, 1999.

[29] Nicolas Barrière, Vincenzo Guidi, Valerio Bellucci, Riccardo Camattari, Thomas Buslaps, Julien Rousselle, Gilles Roudil, Franois-Xavier Arnaud, Pierre Bastie, and Lorenzo Natalucci. High diffraction efficiency at hard X-ray energy in a silicon crystal bent by indentation. *J. Appl. Cryst.*, 43:1519–1521, Dec 2010.

[30] O.I. Sumbaev. *Soviet Phys. JETP*, 5:1042–1044, 1957.

[31] S.G. Lekhnitskii, S.W. Tsai, and T. Cheron. *Anisotropic Plates.* Gordon and Breach Science Publishers, 1956.

[32] H. Kawata, M. Sato, and Y. Higashi. Improvements on water-cooled and doubly bent crystal monochromator for compton scattering experiments. *Nucl. Instrum. Meth. A*, 467468, Part 1:404–408, 2001.

[33] C. Schulze, U. Lienert, M. Hanfland, M. Lorenzen, and F. Zontone. *J. Synchrotron Rad.*, 5:77–81, 1998.

[34] P. Suortti, U. Lienert, and C. Schulze. *AIP Conf. Proc.*, 389:175–192, 1997.

[35] M. Rekveldt. *Nucl. Instrum. Methods*, 215:521–527, 1983.

[36] M. Th. Rekveldt and P. Westerhuuijs. *Nucl. Instrum. Methods Phys. Res. Sect. B*, 28:583–591, 1987.

[37] P. Mikula, E. Krüger, R. Scherm, and V. Wagner. *J. Appl. Cryst.*, 23:105–110, 1990.

[38] M. Popovici, A. D. Stoica, W. B. Yelon, and R. Berliner. *Proc. SPIE*, 3767:320–327, 1999.

[39] N. V. Abrosimov. Mosaic and gradient sige single crystals for gamma ray laue lense. *Exp. Astron.*, 20:185, 2005.

[40] A. Erko, F. Schaefers, W. Gudat, N. V. Abrosimov, S. N. Rossolenko, V. Alex, S. Groth, and W. Schroeder. On the feasibility of employing gradient crystals for high resolution synchrotron optics. *Nucl. Intrum. Meth. A*, 374(3):408–412, 1996.

[41] C. Ferrari, E. Buffagni, E. Bonnini, and D. Korytar. High diffraction efficiency in crystals curved by surface damage. *J. Appl. Cryst.*, 46:1576–1581, 2013.

[42] V.M. Biryukov, Yu. A. Chesnokov, and V. I. Kotov. *Crystal Channeling and Its Application at High-Energy Accelerators.* Springer, Berlin, 1997.

[43] Walter Scandale, Alberto Carnera, Gianantonio Della Mea, Davide De Salvador, Riccardo Milan, Alberto Vomiero, Stefano Baricordi, Pietro Dalpiaz, Massimiliano Fiorini, Vincenzo Guidi, Giuliano Martinelli, Andrea Mazzolari, Emiliano Milan, Giovanni Ambrosi, Philipp Azzarello, Roberto Battiston, Bruna Bertucci, William J. Burger, Maria Ionica, Paolo Zuccon, Gianluca Cavoto, Roberta Santacesaria, Paolo Valente, Erik Vallazza, Alexander G. Afonin, Vladimir T. Baranov, Yury A. Chesnokov, Vladilen I. Kotov, Vladimir A. Maisheev, Igor A. Yazynin, Sergey V. Afanasiev, Alexander D. Kovalenko, Alexander M. Taratin, Alexander S. Denisov, Yury A. Gavrikov, Yuri M. Ivanov, Vladimir G. Ivochkin, Sergey V. Kosyanenko, Anatoli A. Petrunin, Vyacheslav V. Skorobogatov, Vsevolod M. Suvorov, Davide Bolognini, Luca Foggetta, Said Hasan, and Michela Prest. Deflection of 400 *gev/c* proton beam with bent silicon crystals at the cern super proton synchrotron. *Phys. Rev. ST Accel. Beams*, 11:063501, 2008.

[44] Walter Scandale, Dean A. Still, Alberto Carnera, Gianantonio Della Mea, Davide De Salvador, Riccardo Milan, Alberto Vomiero, Stefano Baricordi, Pietro Dalpiaz, Massimiliano Fiorini, Vincenzo Guidi, Giuliano Martinelli, Andrea Mazzolari, Emiliano Milan, Giovanni Ambrosi, Philipp Azzarello, Roberto Battiston, Bruna Bertucci, William J. Burger, Maria Ionica, Paolo Zuccon, Gianluca Cavoto, Roberta Santacesaria, Paolo Valente, Erik Vallazza, Alexander G. Afonin, Vladimir T. Baranov, Yury A. Chesnokov, Vladilen I. Kotov, Vladimir A. Maisheev, Igor A. Yaznin, Sergey V. Afansiev, Alexander D. Kovalenko, Alexander M. Taratin, Alexander S. Denisov, Yury A. Gavrikov, Yuri M. Ivanov, Vladimir G. Ivochkin, Sergey V. Kosyanenko, Anatoli A. Petrunin, Vyacheslav V. Skorobogatov, Vsevolod M. Suvorov, Davide Bolognini, Luca Foggetta, Said Hasan, and Michela Prest. High-efficiency volume reflection of an ultrarelativistic proton beam with a bent silicon crystal. *Phys. Rev. Lett.*, 98:154801, 2007.

[45] S. Bellucci, S. Bini, V. M. Biryukov, Yu. A. Chesnokov, S. Dadagov, G. Giannini, V. Guidi, Yu. M. Ivanov, V. I. Kotov, V. A. Maisheev, C. Malagù, G. Martinelli, A. A. Petrunin, V. V. Skorobogatov, M. Stefancich, and D. Vincenzi. Experimental study for the feasibility of a crystalline undulator. *Phys. Rev. Lett.*, 90:034801, 2003.

[46] Y. Gogotsi, C. Baek, and F. Kirscht. Raman microspectroscopy study of processing-induced phase transformations and residual stress in silicon. *Semicond. Sci. Technol.*, 14:936, 1999.

[47] V. Bellucci, R. Camattari, V. Guidi, and A. Mazzolari. Bending of silicon plate crystals through superficial grooving: modeling and experimentation. *Thin Solid Films*, 520:1069–1073, 2011.

[48] S.G. Lekhnitskii. *Theory of elasticity of an anisotropic body.* Mir Publishers, Moscow, 1981.

[49] B. Erdem Alaca, M.T.A. Saif, and H. Sehitoglu. On the interface debond at the edge of a thin film on a thick substrate. *Acta Mater*, 50(5):1197–1209, 2002.

[50] G. G. Stoney. The Tension of Metallic Films Deposited by Electrolysis. *Proc Royal Soc A*, 82:172–175, 1909.

[51] V. Guidi, L. Lanzoni, and A. Mazzolari. Patterning and modeling of mechanically bent silicon plates through coactive stresses. *Thin Solid Films*, 520:1074–1079, 2011.

[52] Nicolas Barrière, Julien Rousselle, Peter von Ballmoos, Nikolai V. Abrosimov, Pierre Courtois, Pierre Bastie, Thierry Camus, Michael Jentschel, Vladimir N. Kurlov, Lorenzo Natalucci, Gilles Roudil, Nicolai Frisch Brejnholt, and Denis Serre. Experimental and theoretical study of the diffraction properties of various crystals for the realization of a soft gamma-ray Laue lens. *J. of App. Cryst.*, 42(5):834–845, 2009.

[53] I. Neri, R. Camattari, V. Bellucci, V. Guidi, and P. Bastie. Ordered stacking of crystals with adjustable curvatures for hard x- and gamma-ray broadband focusing. *J. Appl. Cryst.*, 46:953–959, 2013.

[54] V. Guidi, V. Bellucci, R. Camattari, and I. Neri. Curved crystals for high-resolution focusing of x and gamma rays through a laue lens. *Nucl. Instrum. Meth. B*, 309:249–253, 2013.

[55] Yu. Ivanov, A. Petrunin, and V. Skorobogatov. Observation of the elastic quasi-mosaicity effect in bent silicon single crystals. *JETP Letters*, 81:99–101, 2005.

[56] Nicolas Barrière, Peter von Ballmoos, Pierre Bastie, Pierre Courtois, Nikolai V. Abrosimov, K. Andersen, T. Buslaps, T. Camus, H. Halloin, M. Jentschel, J. Knodlseder, G. Roudil, D. Serre, and G. Skinner. R&d progress on second-generation crystals for laue lens applications. *Optics for EUV, X-Ray, and Gamma-Ray Astronomy III.*, 6688:66880O, 2007.

[57] F. Frontera, A. Pisa, V. Carassiti, F. Evangelisti, G. Loffredo, D. Pellicciotta, K.H. Andersen, P. Courtois, L. Amati, E. Caroli, T. Franceschini, G. Landini, S. Silvestri, and J.B. Stephen. A gamma ray laue lens focusing telescope aboard a balloon experiment. *Proc. SPIE*, 6266:626–627, 2006.

[58] V. Bellucci, R. Camattari, I. Neri, and V. Guidi. Calculation of diffraction efficiency for curved crystals with arbitrary curvature radius. *J. Appl. Cryst.*, 46:415–420, 2013.

[59] A. Guinier and J. Tennevin. Sur deux variantes de la mthode de laue et leurs applications. *Acta Crystallogr.*, 2:133–138, 1949.

[60] B. Hamelin and P. Bastie. High-energy focusing laue method: Recent developments. *J. Phys. IV.*, 8:3–8, 1998.

[61] M. Stockmeier and A. Magerl. A focusing laue diffractometer for the investigation of bulk crystals. *J. Appl. Cryst.*, 41:754–760, 2008.

[62] E. Virgilli, F. Frontera, V. Valsan, V. Liccardo, E. Caroli, J. B. Stephen, F. Cassese, L. Recanatesi, M. Pecora, S. Mottini, P. Attinà, and B. Negri. The laue project for broadband gamma-ray focusing lenses. *Optics for EUV, X-Ray, and Gamma-Ray Astronomy V*, 8147:81471C–81471C–7, 2011.

[63] F. Frontera, E. Virgilli, V. Liccardo, V. Valsan, V. Carassiti, S. Chiozzi, F. Evangelisti, S. Squerzanti, M. Statera, V. Guidi, C. Ferrari, R. A. Zappettini, E. Caroli, N. Auricchio, S. Silvestri, R. Camattari, F. Cassese, L. Recanatesi, M. Pecora, S. Mottini, and B. Negri. Development status of the laue project. *Space Telescopes and Instrumentation 2012: Ultraviolet to Gamma Ray*, 8443:84430B–84430B–9, 2012.

[64] I. M. Huygens, W.P. Gomes, and K. Strubber. Etching of germanium in hydrogenperoxide solutions. *ECS Trans.*, 6:375, 2007.

[65] A. Authier and C. Malgrange. Diffraction physics. *Acta Cryst.*, A54:806–819, 1998.

[66] R. Camattari, V. Guidi, and I. Neri. Quasi-mosaicity as a tool for focusing hard x-rays. *Space Telescopes and Instrumentation 2012: Ultraviolet to Gamma Ray*, 8443:844335–844335–8, 2012.